Miniaturized Fabry-Perot Polymer Film Ultrasound Sensor for Photoacoustic Endoscope System

by

Tong Li

A dissertation submitted in partial fulfillment
of the requirements for the degree of
Doctor of Philosophy
(Mechanical Engineering)
in the University of Michigan
2023

Doctoral Committee:

Professor Thomas D Wang, Chair
Professor L Jay Guo
Professor Kenn Richard Oldham
Assistant Professor Guan Xu

Tong Li

dqlitong@umich.edu

ORCID iD: 0009-0001-9049-4301

Dedication

To my parents and all the people who have helped me along the way.

Acknowledgements

I would like to thank my advisor, Prof. Thomas D. Wang, for giving me this opportunity to conduct high-level scientific research and helping me grow in every aspect. With his patience, guidance, and generous supports, I gained a deeper understanding of interdisciplinary thinking, problem solving, self-motivation and commitment. They will be priceless treasures in my future endeavors.

I would also like to express my gratitude to the rest of my committee members. I would like to thank Prof. Kenn R. Oldham for his help on clean room fabrication, sensor dynamics modeling and signal processing in my research. I would like to thank Prof. L Jay Guo for his help on optical design and sensor characterization. I would like to thank Prof. Guan Xu for his help on tissue imaging. This dissertation would not have been possible without the generous guidance and valuable feedbacks from all the committee members.

I'm also grateful to the current and former members in our lab for generous help and friendly environment. Dr. Xiyu Duan and Dr. Quan Zhou, as senior PhD students, introduced me into the research world and helped me through the transition when I first started my PhD career. I'm grateful to our former postdoctoral members, Dr. Haijun Li for his broad knowledge and help on MEMS fabrication and mechanical design, and Dr. Gaoming Li for his insights in optical design. I would like to thank Tse-Shao Chang for his help on photoacoustic imaging and mechanical design, Ahmad Shirazi for his help on probe fabrication, and Dr. Xiaoli Wu on animal experiments. I would like to thank Miki Lee, Ruoliu Zhang, Dr. Shuo Feng, Dr. Sangeeta Jaiswal, Dr. Fa Wang, Dr. Xiaoqing Meng and all other current and former lab members for their help.

This dissertation would not have been possible without the help from collaboration. I would like to express my thanks to Prof. Kenn R. Oldham's students, Dr. Mayur Birla and Joonyoung Yu for their help on clean room fabrication, and Prof. L Jay Guo's student, Wei-Kuan Lin for his help on sensor characterization.

I would also like to thank staff of the Lurie Nanofabrication Facility at the University of Michigan for training and supports on fabrication of my sensors.

Finally, I would like to thank my parents for their love, encouragement and supports during my years of studying abroad.

Table of Contents

List of Tables

List of Figures

Abstract

Colorectal cancer (CRC) is estimated to be the fourth most common cancer and the second most deadly cancer in 2023. The development of such cancer usually involves a growing polyp into deeper tissue. Thus, depth-resolving imaging modalities will help detect and stage CRC for early prevention and better treatment. Photoacoustic endoscopy (PAE) is an emerging imaging technology that combines the advantages of optics and ultrasound. Various designs of PAE have been proposed, however, there is still a need for highly sensitive, transparent, and miniaturized sensors. A Fabry-Perot (FP) polymer film ultrasound sensor is an excellent candidate to satisfy these demands. The current FP sensors are either bulky substrate-based sensor array, single fiber-based sensor, or fiber bundle-based sensor array. None of them can achieve transparency, miniaturization, design flexibility and array configuration at the same time. Thus, in this dissertation, we propose using thin wafer-based FP sensor to fabricate miniaturized and cost-effective sensor array for PAE applications.

A transfer matrix-based model is developed to study the physics of multilayer structure of the miniaturized sensor. An approximate model is then built to simplify the problem, and it reveals that the finite thickness substrate acts as a filter in the frequency domain. Thus, the frequency response of the miniaturized sensor can be back filtered to remove the effect of the substrate, demonstrating the feasibility of miniaturization in theory.

The sensor is fabricated by depositing gold and Parylene C films onto a glass wafer. It turns out that the sensitivity is not uniform on the wafer surface. However, by dicing the thin wafer carefully, a relatively uniform region can be selected and treated as a sensor array. In this way a

fixed wavelength laser can be used to interrogate this sensor instead of an expensive tunable laser required in other FP sensors.

A 2 mm by 9 mm rectangular sensor array is fabricated in this way and a tabletop system is built to conduct tomography imaging. The system clearly shows the structure of a phantom made from a knotted wire and the polyps from a CPC-APC mouse colon tissue ex vivo with IV injection of gold nanoshell. The system has a best NEP of 0.76kPa, a -3dB bandwidth of 16.6 MHz, a lateral resolution of 208 μm and an axial resolution of 32 μm.

A 2 mm by 2 mm single element sensor is fabricated to verify the feasibility of being integrated into a PAE probe. A miniaturized PAE probe based on the 2 mm sensor is designed. The sub-probe for 532 nm excitation laser delivery in the PAE design is fabricated to demonstrate the feasibility of miniaturized PAE probe. The imaging performance is demonstrated by phantom imaging and in vivo imaging of the ear of a nude mouse. Another sub-probe using 800 nm is built for deep tissue imaging with gold nanoshell. The system can image phantoms and prolapsed CPC-APC mouse in vivo with IV injection of gold nanoshell.

These results show that the proposed miniaturized FP sensor is promising to enable novel PAE designs for better CRC detection and staging.

Chapter 1 Introduction

1.1 Colorectal cancer

According to American Cancer Society, colorectal cancer (CRC) is estimated to be the fourth most common cancer with both sexes combined in 2023, with a number of new cases of 153,020. It also causes the second most deaths among all type of cancers, with an estimated deaths of 52,550 in 2023 [1]. The incidence of colorectal cancer in 2012-2016 and mortality in 2013-2017 are 38.7 and 13.9 per 100,000 population, respectively [2]. Most CRC develops from a polyp, which is a noncancerous growth in the mucosa of the colorectum [2]. As the polyp grows and finally develops into cancer, it can invade into the blood or lymph node vessels in the colorectal wall and spread to other regions of the body, causing a spread of cancer referred to as metastasis [2]. The term stage is used to describe the extent of the spread of cancer by the time it is diagnosed. According to the Surveillance, Epidemiology, and End Results (SEER) summary staging system, CRC is categorized into four stages: in situ, local, regional and distant with an ascending severity [2]. Colorectal cancer five-year survival rate drops dramatically from 90% of local stage to only 14% of distant stage, while 21% of CRC is staged as distant when diagnosed [2]. Thus, using screening tool with staging ability, i.e., depth-resolving ability, as early as possible will bring early diagnosis, better treatment plan and prevention of late-stage cancer.

1.2 Common depth-resolved imaging modalities in endoscopic application

Colonoscopy is the most common tool for CRC screening [2]. Thus, some common deep tissue imaging modalities such as X-ray computed tomography (CT) and magnetic resonance

imaging (MRI), given their bulky dimensions, will not be discussed in this dissertation. The remaining common depth resolved imaging modalities that can be implemented in an endoscopic form factor are ultrasound, optical imaging, and photoacoustic imaging.

1.2.1 Ultrasound

Ultrasound (US) is a commonly used modality to image internal organs. It is a sound, or more accurately, pressure wave, that has a frequency beyond the threshold of human hearing (20 kHz). During ultrasound imaging, a short pulse of ultrasound wave is generated by an ultrasound transducer and propagates in tissue. This ultrasound wave is reflected if there is a change in acoustic impedance such as the boundary of an organ. The reflected wave appears as an echo to the original wave and is received by the same ultrasound transducer. The time delay of the echo is used to calculate the depth of the target. The axial resolution depends on the frequency of the ultrasound wave, but higher frequencies suffer from increasing attenuation in soft tissue [3]. Overall, frequencies of several to tens of megahertz are used in ultrasound imaging. The lateral features of the target are resolved by using a transducer array to steer the pulse and reconstruct the received signal by changing the phases on different elements of the array. An imaging depth of centimeters is easily achieved nowadays. However, this imaging modality replies on the reflection property change inside of the tissue. If the physical properties of the polyp or cancer tissue is not too different from that of the normal tissue, ultrasound will lose imaging contrast. This limits the potential of ultrasound in cancer detection and staging.

1.2.2 Optical imaging

Optical imaging refers to a wide range of imaging modalities that use light to form an image. Thanks to the short wavelength of light wave, sub-cellular resolution is already achieved

in many optical imaging modalities. Two common categories of optical imaging are confocal microscopy and optical coherence tomography (OCT).

In confocal microscopy, the light from a source, which is usually a laser, passes through a pinhole and gets focused by an objective lens onto the target. The focused light can either be used to excite fluorescence signal or simply form reflectance image. The signal light is collected by the same objective lens, passes through another pinhole, which is at the confocal position of the first pinhole, and is collected by a photodetector. Any light that comes out of the focus of the objective lens will not pass through the second pinhole, thus reducing noises and improve resolution. Such imaging modality can provide excellent sub-cellular resolution by using high numerical aperture (NA) objective lenses. Fluorescence based on excitation wavelength can also provide molecular information of the tissue. However, biological tissue is a highly scattering medium and optical resolution will degrade significantly beyond an imaging depth of about 1 mm [4]. Imaging with confocal microscopy in a depth of several millimeters will compromise sub-cellular resolution, thus losing its original advantages.

OCT is another optical modality that provides even better imaging depth. It is essentially an interferometer using a low coherence light source. The light is divided into two beams, and one is focused onto the tissue while the other one is used as a reference arm. The reflected light from the tissue is combined with the reference arm to form an interference pattern and is detected by a photodetector. The reference arm is axially scanned to form the best interference signal, and the low coherence of the laser makes sure that the interference is only good when the two beams align almost perfectly. This provides the depth-resolving ability of OCT. However, since the interference is formed from reflected light from the tissue, there is a lack of molecular information and thus decreasing the imaging contrast between cancer and normal tissue.

1.3 Principle of photoacoustic imaging

Photoacoustic imaging (PAI) is based on photoacoustic (PA) effect, which was discovered by Alexander G. Bell back in the 1880s [5]. When a very short light pulse, usually from a nanosecond pulsed laser, is incident onto the target, the target will absorb the laser energy and undergo rapid thermal expansion. This expansion will then cause a rapid pressure rise in the surroundings due to thermoelastic effect, and this initial pressure distribution will propagate outwards as an ultrasound wave. This wave is a wide-band short pulse and can go up to tens or more than a hundred megahertz, depending on the scale of the absorber [6]. A photoacoustic image is the reconstructed absorption distribution in the target region using the detected ultrasound signal. This process is illustrated in Figure *1.1*. Since the absorption depends on the molecular property of the tissue, photoacoustic imaging combines the good image contrast of optics and good penetration of ultrasound, making it a promising candidate in detecting and staging colorectal cancer.

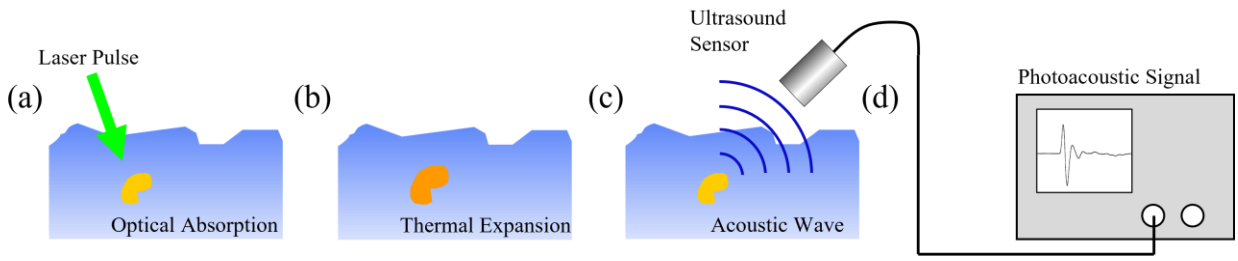

Figure 1.1 Principle of photoacoustic imaging

Due to the hybrid nature of optical imaging and ultrasound, photoacoustic imaging has a variety of configurations. Photoacoustic tomography (PAT) uses an ultrasound sensor array to detect the PA signal excited by an unfocused pulsed laser that illuminates the whole field of view. The lateral features are resolved using reconstruction algorithms, such as delay and sum in conventional ultrasound imaging, or algorithms developed specifically for PAT such as universal

back-projection [7] and frequency-domain reconstruction [8], etc. Scanners are usually unnecessary, because a 2-D array is sufficient to form 3-D images, while a 1-D array can be used to generate 2-D cross sectional images. The lateral resolution of PAT depends on the aperture of the sensor array, while the axial resolution depends on the bandwidth of the ultrasound array [9]. Since the excitation laser is not focused, the imaging penetration depth is fundamentally limited by the dissipation limit of about 10 cm [10], thus providing a much better imaging depth than optical imaging modalities. A photoacoustic microscopy (PAM) uses a single element ultrasound sensor, and scanning mechanism is required to acquire PA signals pixel by pixel to resolve the lateral features [11]. Similar to ultrasound imaging, the depth information is resolved from the time-domain signal. Since both the excitation light and the ultrasound sensor can be focused, PAM can be further categorized into optical-resolution photoacoustic microscopy (ORPAM) and acoustic-resolution photoacoustic microscopy (ARPAM), depending on which wave has a tighter focused spot. An ORPAM can achieve optical sub-cellular resolution [12], [13], but the imaging depth is limited by the diffusion limit as in pure optical imaging, while an ARPAM can achieve similar resolution and depth as in ultrasound [14], [15].

1.4 Photoacoustic endoscope

Because of its advantages in imaging contrast and depth, photoacoustic imaging provides an excellent candidate to be implemented into an endoscopic probe, known as photoacoustic endoscope (PAE). PAE is an emerging imaging modality and has it has been extensively researched in recent years, thanks to the advances in miniaturization of optical and ultrasound technologies [16]–[49]. Most PAE probes are consist of the following components: excitation light delivery components, ultrasound sensor to detect PA signals, and scanning mechanism to form images. ORPAM, ARPAM and PAT configurations have all been implemented in PAE probes.

Depending on the application, PAE probes can be mainly divided into the following two categories: gastrointestinal (GI) tract endoscopes [18]–[23], [25], [28], [29], [31]–[34], [38], [40], [41], [43], [44], [47]–[49], and intravascular photoacoustic (IVPA) imaging probes [16], [17], [24], [26], [27], [35]–[37], [42], [45], [46]. PAE also finds applications in colposcopy [39] and cystoscopy [30], though they share a lot in common with GI tract endoscopes. Various imaging targets in biology tissues have been studied by using proper excitation wavelengths. Because the optical and ultrasonic components in PAE are also common in optical and ultrasound imaging modalities, it is convenient to build a multimodal endoscopic probe by reasonable additional efforts. Multimodal imaging probes incorporating one or more of ultrasound [16], [17], [19], [20], [22], [24], [26], [29], [30], [32], [36], [40], OCT [27], [42] and other modalities [18], [28], [35], [37], [45] have been proposed. A detailed discussion of current PAE systems from different aspects is provided below.

1.4.1 Ultrasound sensors

Ultrasound sensors play a dominant role in PAE systems. The most common ultrasound sensors used in PAE are piezoelectric material-based ultrasound transducers. These devices are based on the direct piezoelectric effect, where electric charges are induced on the surface of a piezoelectric material under mechanical stress, and inverse piezoelectric effect, where mechanical deformation of the piezoelectric material is induced by an external electric field. These effects are reversible, making them ideal for receiving and generating ultrasound waves. There has been extensive research on piezoelectric materials for fabricating ultrasound transducers, and the most common materials that are recently reported in PAE include lead zirconate titanate (PZT) [16], [17], polyvinylidene fluoride (PVDF) [18]–[21], lead magnesium niobate-lead titanate (PMN-PT) [22], and lithium niobate (LiNbO3) [23]. Each of the materials has its own pros and cons, and

tradeoff is usually necessary in design of PAE systems. Meanwhile, miniaturized ultrasound transducers have been commercially available, greatly advancing the progresses in design and fabrication of endoscopic PA imaging probes [24]–[30].

In terms of the relative positions of the ultrasound sensor and the excitation laser beam, there are basically two configurations: coaxial and noncoaxial configurations. In coaxial configuration, the optical axis of the laser beam is aligned with the acoustic axis of the transducer. Due to the opaque nature of most ultrasound transducers, the coaxial configuration is usually achieved by fabricating the transducer into a ring shape, allowing the laser beam to go through the center of the transducer [17]–[20], [31]–[34]. A typical coaxial design [31] is shown in Figure *1.2* (a). An alternative approach to achieve coaxial alignment is to use a transparent acoustic reflector that reflects the incident PA signal while allowing the excitation laser beam to go through [38]. The ultrasound transducer can thus be placed at 90 degrees with respect to the optical path, as shown in Figure *1.2* (b). This design requires more space in the imaging tube, thus introducing more difficulties in probe design. In noncoaxial configuration, the transducer is simply placed by the side of the laser beam, and the optical axis is at an angle with respect to the acoustic axis, creating an oblique illumination of the tissue [16], [22]–[28], [35]–[37]. A representative noncoaxial PAE design [22] is shown in Figure *1.2* (c). In addition to coaxial and noncoaxial configurations, some other designs have also been proposed. Zhao et al. [21] demonstrated a transparent, ITO-coated, PVDF thin film ultrasound sensor that can directly allow the laser beam to through. In 2022, Yang's group demonstrated two PAE probes with similar designs of using dual miniaturized ultrasound transducers on the two sides of the laser beam, forming a quasi-coaxial configuration [29], [30].

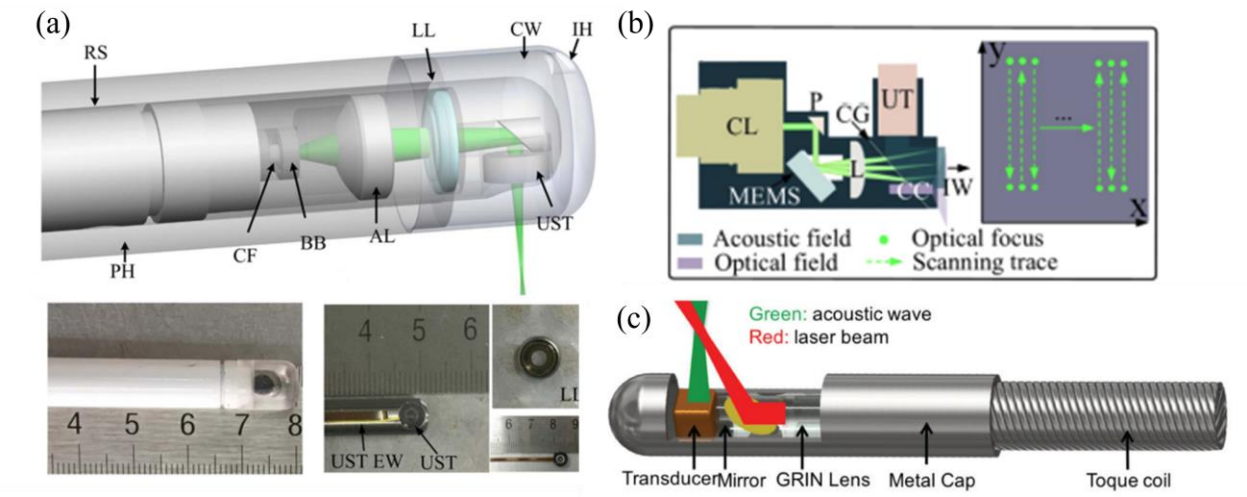

Figure 1.2 Representative coaxial and noncoaxial designs in PAE

The aforementioned PAE systems operate in the PAM configuration. Endoscopic PAT systems based on miniaturized ultrasound array have also been reported [39], [40]. Although transducer array makes the size of the probe larger, the system is free from scanning mechanism because of the electronically scanning capability of a phased array.

While piezoelectric detectors have played an important role in PAE systems, they suffer from decrease of sensitivity when being miniaturized [50], resulting in a need for alternative ultrasound sensing strategies. In addition to piezoelectric material-based ultrasound transducers, optical ultrasound sensors make up another large portion of PAE designs [41]–[49]. Among them the most common optical sensors are fiber based Fabry-Perot interferometer ultrasound sensors [41]–[46]. The detailed working principle of such sensors will be discussed in Section 1.5. Other types of optical ultrasound sensors, including microring resonator [47], remote sensing [48] and linear-cavity fiber laser-based ultrasound sensor [49]. These sensors can achieve extremely small element sizes without sacrificing sensitivities, are immune to electromagnetic noises when operating in a long distance and have the potential of being made transparent to the PA excitation laser, making them highly suitable for being implemented into miniaturized imaging probes [50].

They provide promising candidates for novel PAE systems and more research is needed to advance the field.

1.4.2 Delivery of excitation light and scanning mechanism

The ultrasound sensors are essential in the detection end, while the generation of PA signals is the other half of the story. Optical fibers are used as flexible wave guides to deliver laser light to the tissue. Since high energy pulses are required to generate PA signals, multi-mode fibers (MMF) are more often used to avoid damage to the optics [16], [17], [21]–[27], [32], [35]–[37], [40], [44]–[47]. Single-mode fibers (SMF) are also used to deliver the laser pulses [18]–[20], [28]–[31], [33], [34], [38], [42], [48], [49] when optical resolution is pursued. Fiber bundles have also been reported for pulse delivery [41], [43]. The laser coming out of the fiber is usually focused by a miniaturized gradient-Index (GRIN) lens [16], [18], [22], [25]–[27], [29], [30], [33], [35], [43], [47]–[49] or other types of miniaturized lenses [19], [20], [28], [31], [34], [37], [38] to achieve optical resolution. In these cases, the lateral resolution of the system is determined by the size of the focus spot of the excitation laser, so the ultrasound sensors are unfocused. They actually can be regarded as miniaturized version of ORPAM. Meanwhile, in other proposed designs, the laser directly comes out of the fiber and is incident onto the tissue without being focused [17], [23], [24], [32], [36], [39]–[42]. The lateral resolution is determined by the ultrasound transducer, and they fall into the category of either ARPAM or PAT.

Scanning mechanism in PAE system depends on which imaging configuration the system is. For the probes using PAM configuration, a pixel-by-pixel scanning mechanism is needed to resolve lateral features. Most designs apply a side-viewing configuration, which is an intuitive idea when imaging hollow organs or inside of the vasculature. Thus, a rotary scanning mechanism is used to drive the probe and form a circumferential field of view, which is realized by either directly

driving the probe with a rotary motor [20], [23], [24], [26]–[31], [37], [47], [49] or transmitting the torque through a torque coil from a long distance [16], [17], [22], [35], [36], [42]. A linear stage or motor is often used for pullback to form 3-D images. Micromotor has also been implemented at the distal end of the probe to rotate the reflector which directs the laser into the tissue in a side-viewing configuration [18]. In this way the whole probe except for the reflector can stay stationary during imaging, but the micromotor introduces more complexity to the system and makes the distal end too long to go into a working channel of a clinical endoscope. Micro-electromechanical systems (MEMS) scanners have also been proposed to scan the excitation laser beam [34], [38]. However, their field of view is limited compared to the rotation-based scanning mechanism. For front-viewing configurations, a 2-D motorized stage is used to scan the pixels and the system operates like a tabletop microscope [19], [33], [48]. In addition, some research use wavefront shaping techniques to achieve optical focusing and scanning [21], [45], [46] and they operate as ORPAM. If a transducer array is used [39]–[41], [44], it can directly form a cross-sectional image without scanning the probe, thus reducing motion artifacts during imaging.

1.4.3 Application, contrast agents, and multimodality in PAE imaging

Based on the clinical applications, most endoscopic PA imaging systems can be categorized into two following groups: gastrointestinal (GI) tract endoscopes and intravascular photoacoustic (IVPA) imaging probes. A GI tract endoscope examines the important organs in the digestive system such as esophagus and colorectum. The PAE developed for imaging GI tract should be able to go through an instrument channel of a video endoscope so that it can be used in clinics, which puts a limit to the size of the probe. A variety of PAE systems designed for GI tract imaging have been demonstrated to examine various animal models and human tissue, including in vivo rabbit colorectum [18], [20], [23], [31], [40], in vivo rat colorectum [22], [28], [29], [49]

and intestine [38], in vivo swine esophagus [29], and ex vivo human colorectal tissue [32]. In vivo rabbit urinary tract [30], ex vivo human ectocervix and in vivo anterior surface of the ectocervix [34] have also been imaged using relatively similar endoscopic designs.

Another category, intravascular photoacoustic (IVPA) imaging probes, are inserted into the artery to image abnormal tissues such as atherosclerotic plaques. Thus, the size requirement is even stricter than GI tract endoscopes. In recent years the proposed probes are all smaller than 1.6 mm [16], [17], [24], [26], [27], [35]–[37], [42], [45]. Their imaging targets are all different types of arteries, such as in vivo rabbit aorta [16], [24], [26], [37], ex vivo rabbit aorta [35], ex vivo porcine coronary artery [17], [27], ex vivo human coronary artery [24] and ex vivo mouse thoracic aorta [36].

PAE probes have also imaged biological tissues to test their performance when not inserted into an organ or the body of an animal. They include in vivo human palm and mouse ear tumor [19], in vivo zebrafish larvae [28], [48], in vivo mouse ear [25], [33], [49], eye, back, leg [33] and skin [41], ex vivo duck embryo [41], ex vivo human placenta [44] and ex vivo red blood cells [45], [46].

The molecular imaging target determines the wavelength of the excitation laser and the application of the PAE system. Since the generation of PA signal relies on the absorption of the incident laser, endogenous tissue chromophores with high absorption at available wavelength are preferred in PAI. The abundance of hemoglobin in biological tissue makes it an excellent imaging contrast agent for imaging vasculature structure or measuring blood oxygen saturation. At 532 nm, the optical absorption of oxyhemoglobin and deoxyhemoglobin (HbO2 and HbR) are identical, so the PA signal is proportional to the concentration of total hemoglobin [51]. Thus, most of the recent PAE systems use 532 nm or a nearby wavelength to reveal the vasculature structures [18]–[22],

[28]–[31], [33], [34], [38], [41]–[43], [45], [46], [49]. Another endogenous imaging agent is lipid, which can be found to be rich in plaque and has a strong absorption at around 1720 nm [52]. Most IVPA probes use a wavelength around 1720 nm to image the aorta [24], [26], [27], [35]–[37]. A wavelength around 1300 nm has also been used to image collagen [23], [27], [40]. Applying exogenous imaging contrast agents can further enhance the PA signal or provide additional contrast. Nanoparticles with an absorption peak at 1064 nm [16], [17] and indocyanine green (ICG) at 780 nm [26] have been reported for PAE imaging.

Due to the hybrid nature of photoacoustic imaging, it is intuitive to add multimodal imaging capability to PAE systems. When an ultrasound transducer is used in PAE to collect signals, it can also be controlled to perform pulse-echo operation and work as a pure ultrasound imaging probe without significant modifications to the current system. Various endoscopic PA/US systems have been proposed [16], [17], [19], [20], [22], [24], [26], [29], [30], [32], [36], [40]. The ultrasound images can show the structure of the tissue, while PAI shows the molecular information of the tissue. The images are often overlaid in the same image to extract more information from the tissue. Other multimodal imaging probes involve optical imaging and system modifications on the optics are needed. Fluorescence imaging [28], [37], [45], optical coherence tomography [42] and hyperspectral imaging [18] have all been implemented in PAE probes. Tri-modality imaging systems of PA/US/OCT [27] and US/PA/elasticity imaging [35] have also been proposed. These designs show the flexibility of PAI to work with other imaging modalities in a single imaging instrument, which can be beneficial to inspire novel technologies to cope with complex imaging environments.

1.5 Working principle of Fabry-Perot polymer film ultrasound sensor

Fabry-Perot (FP) polymer film ultrasound sensor has been widely used in PAE imaging systems, and its working principle has been well studied [53]. A Fabry-Perot polymer film ultrasound sensor is based on Fabry-Perot interferometer. It consists of a thin polymer film in between the backing material and the surrounding medium, which forms a resonant cavity. An incident optical wave will undergo multi-reflection inside of the film, and the output wave is the interference of all the waves after multi-reflection, as shown in Figure *1.3* (a). The output intensity depends on the one-way phase difference between each wave, which is defined as:

$$\phi = \frac{2\pi}{\lambda} nl \cos\theta'$$

where λ is the wavelength of the interrogation laser, n is the index of refraction of the film, l is the thickness of the film, and θ' is the angle of the direction of the traveling wave inside of the film. The curve of output intensity with respect to change of the phase is referred to as the interferometer transfer function (ITF). The detailed mathematical derivation of ITF will be given in Section 3.5.

If the thickness of the polymer film is modulated by an incident ultrasound wave, the phase will also be modulated, thus creating a modulation in the output laser intensity, as shown in Figure *1.3* (b). This modulation can be detected by a photodetector, and this time-domain signal can be used to calculate the waveform of the incident ultrasound wave. Softer polymer will result in a larger change in thickness under the modulation of the ultrasound wave, thus having a larger signal output. However, their frequency responses tend to have smaller bandwidths due to the low mechanical stiffness. Thus, the selection of polymer material is a tradeoff between sensitivity and bandwidth. Given the same amount of phase change, the maximum output intensity change will occur at the phase where the slope of the ITF is steepest. To make sure the FP sensor is working

at this optimal center phase, a tunable laser is used to shift the ITF curve so that the steepest slope occurs at the desired center phase. The ITF curve gets sharper when the reflectivity on the interfaces of the materials are higher, so highly reflective mirrors can be coated on the two sides of the polymer film to increase the sensitivity of the sensor. What's more, well designed optical coatings made from dielectric materials can be highly reflective to the interrogation laser while transparent to the excitation laser in PAI, thus providing a promising approach to make transparent sensors in PAE. The FP sensor also only outputs signal when the thickness changes, thus working in a thickness mode. Thus, the lateral size does not affect the sensing principle and miniaturization is made possible.

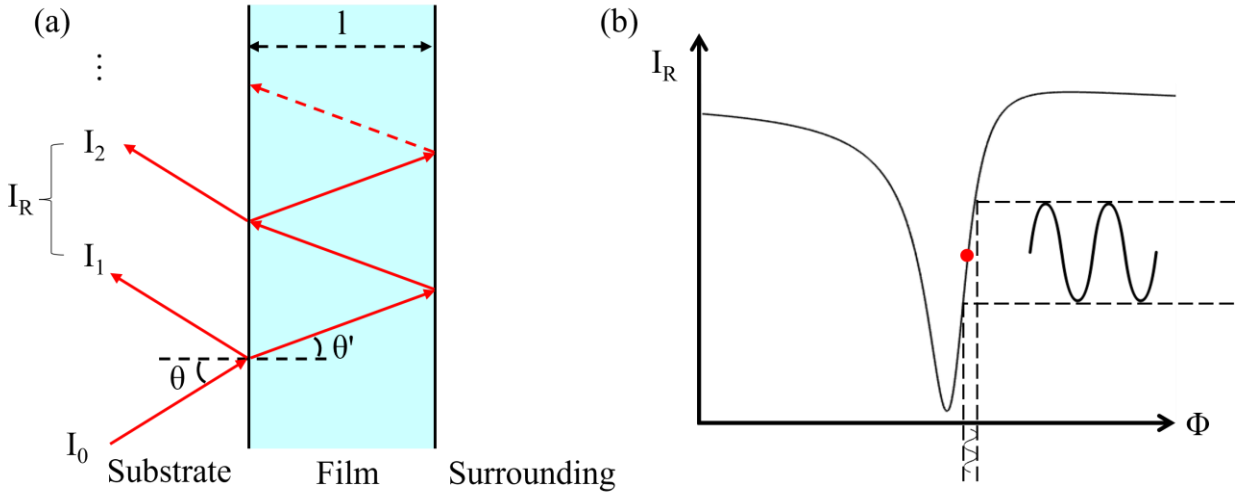

Figure 1.3 Working principle of FP interferometer ultrasound sensor

1.6 Miniaturized Fabry-Perot polymer film ultrasound sensors

Multiple configurations of Fabry-Perot polymer film ultrasound sensors have been developed for photoacoustic imaging systems. They generally fall into three categories: bulky substrate-based scanning head, single optical fiber-based FP sensor, and fiber bundle-based sensor array.

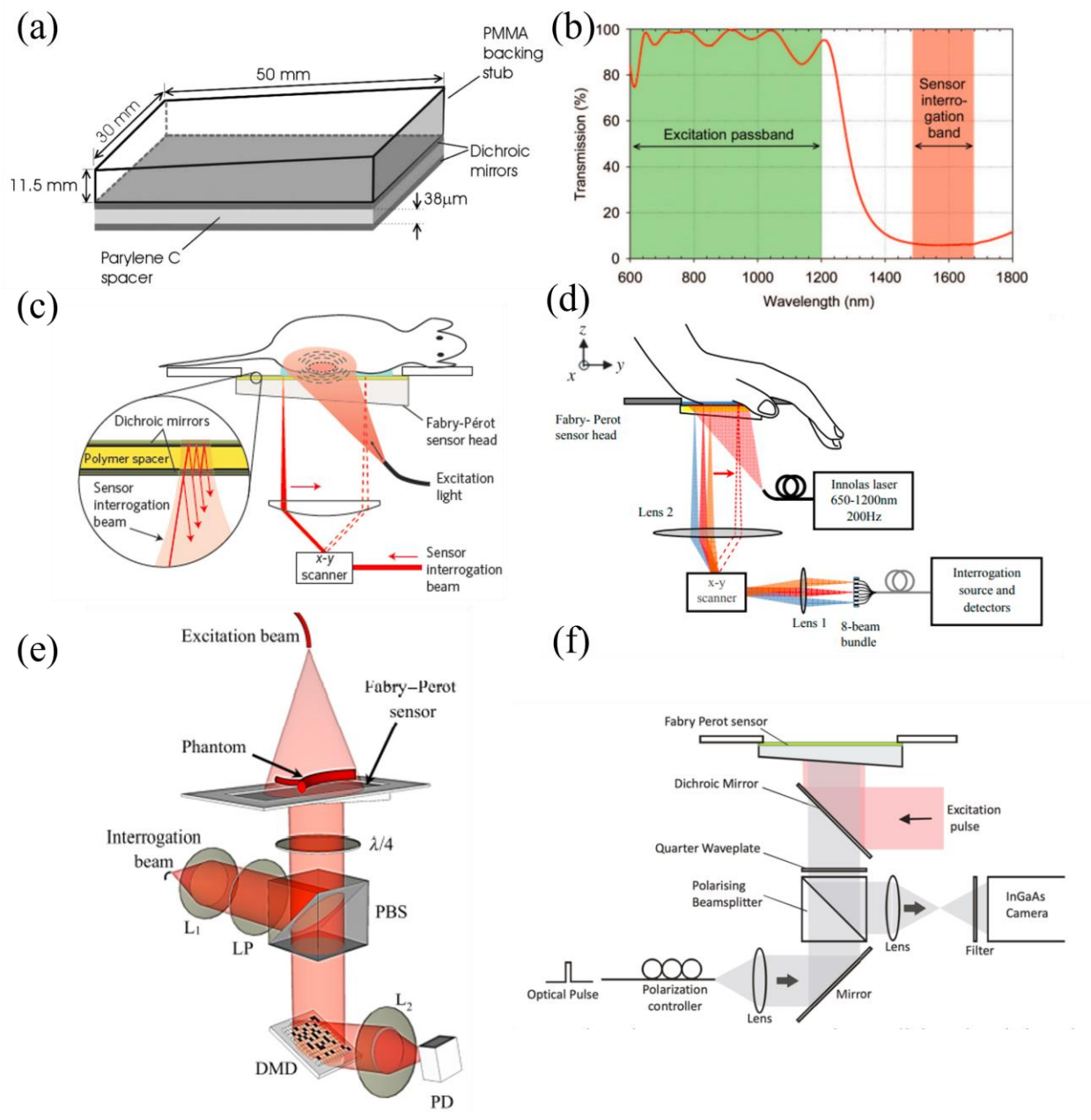

Figure 1.4 Different bulky substrate-based FP sensors

Figure *1.4* (a) shows a representative bulky substrate-based FP ultrasound sensor [54]. The sensor was built for a tabletop imaging system and served as a 2-D ultrasound array for tomography imaging. Dichroic mirrors are formed by alternately depositing two materials with different indices of refraction. This is to achieve highly reflective mirrors for the interrogation wavelength, while allow maximum transmission for the excitation wavelength, thus forming a transparent ultrasound

sensor. A representative dichroic mirror transmission characteristic is shown in Figure *1.4* (b) [54]. Under the effect of an incident ultrasound wave, every point on the sensor head has an individual response to the wave, and they can be treated as the sensing elements of a sensor array. In early demonstrations, the interrogation beam is focused by a lens and scanned by a 2-D scanner across the surface of the sensor head to record all the responses from the virtual sensing elements, as shown in Figure *1.4* (c) [55]. The size of the virtual element is defined by the diameter of the focus spot. Each time only the response from one virtual element is recorded when ultrasound waves are generated by an excitation pulse. So, the system actually works under the assumption that the generated ultrasound waves are the same from pulse to pulse, and the acquisition time is fundamentally limited by the repetition rate of the pulsed laser. Several strategies have been proposed later to overcome this limitation. Huynh et al [56] demonstrated an 8-beam scanner which splits the interrogation laser equally into 8 beams and scans them simultaneously to decrease the total acquisition time, as shown in Figure *1.4* (d). Later, they proposed a single-pixel camera PAT system where the sensor head is illuminated uniformly by a collimated interrogation beam and a digital micromirror device (DMD) is used to spatially sample the reflected beam from the sensor and its output is focused onto a photodetector to record the signals, as shown in Figure *1.4* (e) [57]. The virtual element size is limited by the mirror size of the DMD, and it is still a one pulse-one pixel scanning strategy. Allen et al further developed this concept and directed the collimated reflected beam onto a camera to record all the responses of the surface of the sensor head, as shown in Figure *1.4* (f) [58]. However, the required sampling rate to record the time-domain ultrasound signals is well above the frame rate of the camera, so the system just recorded one single frame of the responses at a certain delay from one excitation pulse and looped through different delays with sequential pulses to acquire the 3-D data sets. Thus, this one pulse-one frame

scanning strategy is fundamentally not so different from the previous strategies. In the future, a one pulse-one 3-D image system can be realized with the development of megahertz sampling rate high speed camera or photodetector array with large number of elements. However, the transparency and the small virtual array elements with high sensitivity already make such FP sensors a good candidate in PAI systems.

A miniaturized version of the FP sensor is appreciated in the development of a PAE system. Since optical fibers are common for light delivery, it is an intuitive idea to build FP sensor on fiber tips. An early demonstration of fiber-based FP sensor is shown in Figure *1.5* (a) [59]. A Parylene C film and two gold mirrors were deposited on the tip of an optical fiber. Zhang and Beard also proposed a FP sensor built on a rounded tip fiber to improve frequency response and directional characteristics by smoothing the sharp diffractive boundaries of the flat tip, as shown in Figure *1.5* (b) [60]. However, since the beam coming out of the fiber is divergent, the multi-reflected beams inside of the polymer film cannot align with each other spatially well and go back to the fiber core, thus decreasing the sensitivity of the sensor. To solve this problem. Guggenheim et al proposed a planoconcave micro resonator formed on the tip of a fiber by dip-coating techniques, as shown in Figure *1.5* (c) [61]. The concave mirror is designed to be perpendicular at any angle with respect to the diverging beam, thus well-aligned interference is created inside of the curved spacer and most of the output is collected by the same fiber core. In addition to improved sensitivity, the curved sensing surface also enables omnidirectional detection. Both front-viewing [43], [45], [46] and side-viewing [42] PAE systems have been proposed using such fiber-based FP sensors. However, they can only work as single element sensors and mostly work in ORPAM, thus the imaging depth is limited compared to PAT.

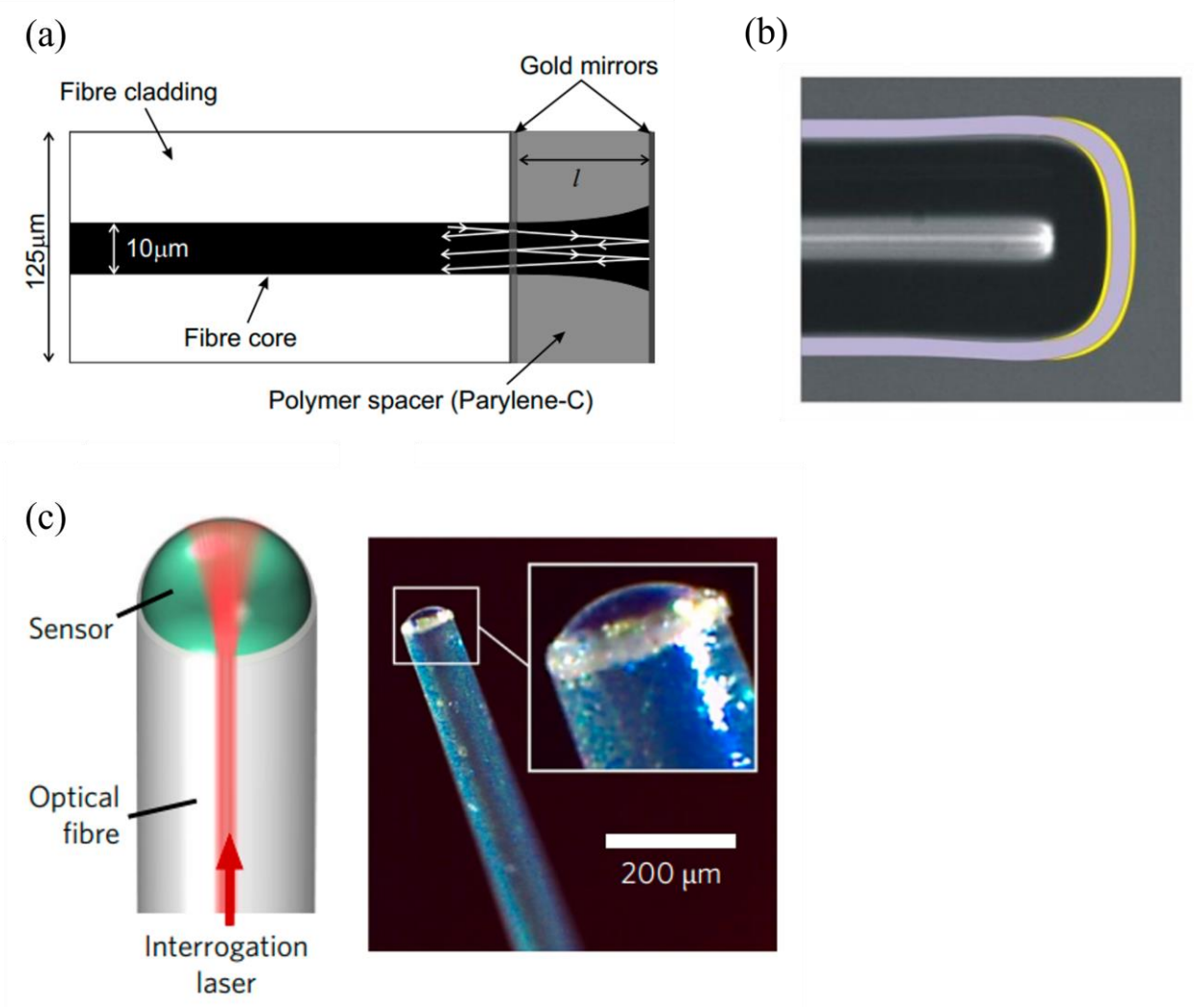

Figure 1.5 Different designs of optical fiber-based FP sensors

Fiber bundle-based FP sensors have also been proposed as an attempt to achieve tomography using fiber-based sensor arrays. Ansari et al demonstrated a front-viewing fiber bundle-based PAE probe for 3-D imaging, as shown in Figure *1.6* (a) [41]. Dichroic mirrors and Parylen-C polymer are deposited on the flat tip of the fiber bundle. Each fiber in the bundle forms a single element sensor. The interrogation beam is focused and scanned on the other end of the fiber bundle to collect the signals from each single fiber. Thus. this is also a one-pulse, one pixel configuration. The same fiber bundle is also used to deliver excitation light thanks to the transparency of the mirrors at the excitation wavelength. Later, they proposed a flexible front-

viewing PAE system, as shown in Figure *1.6* (b) [44]. This time the fiber bundle only serves as a wave guide and a bulky-substrate sensor head is mounted on the distal end of the probe. The interrogation light coming out of the bundle is focused by a pair of lenses onto the sensor head and it is scanned on the other end of the fiber bundle. In summary, these fiber bundle-based FP sensors combine the advantages of single fiber-based sensors and bulky substrate-based sensors. However, they can only achieve front-viewing configuration, where side-viewing is usually preferred in endoscopic applications.

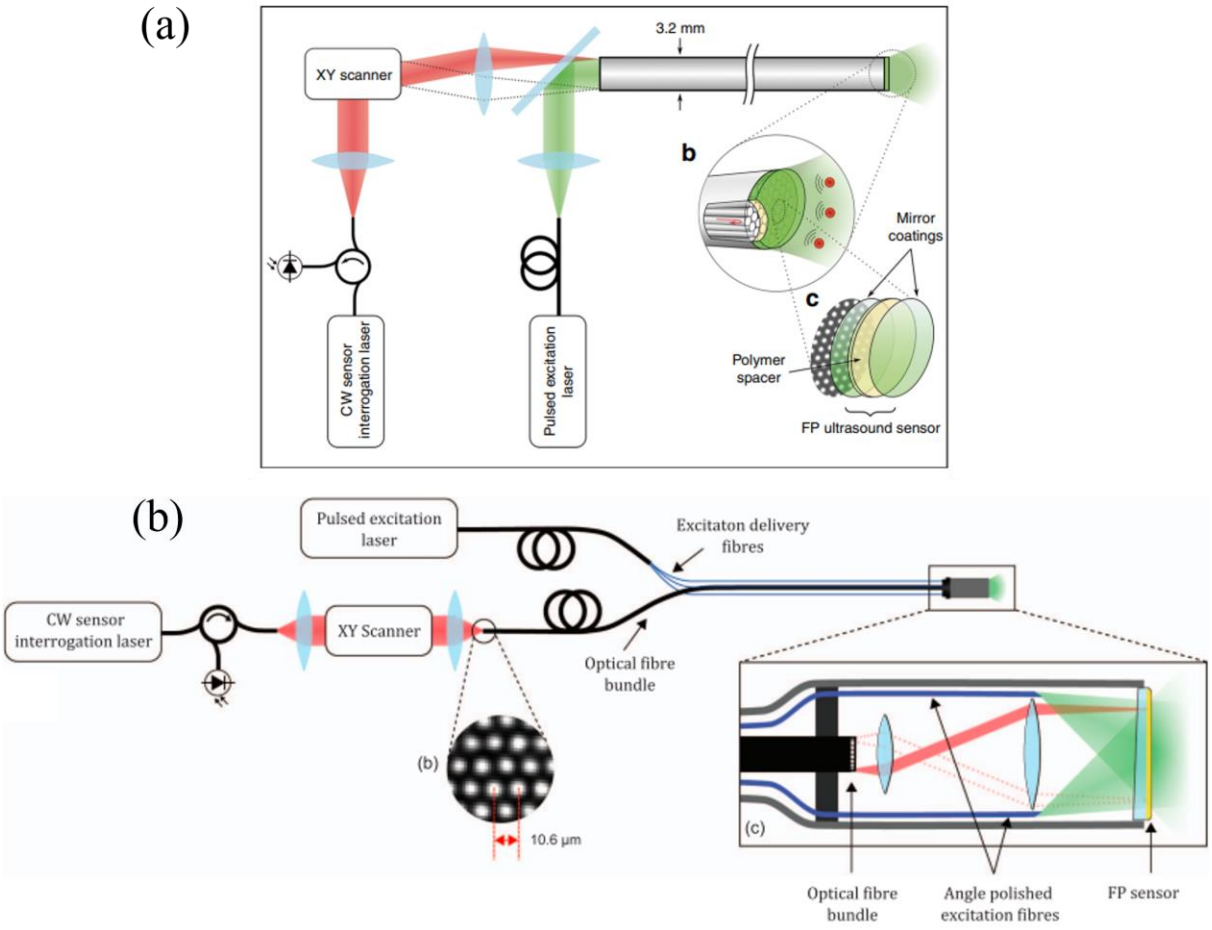

Figure 1.6 Fiber bundle-based FP sensor array

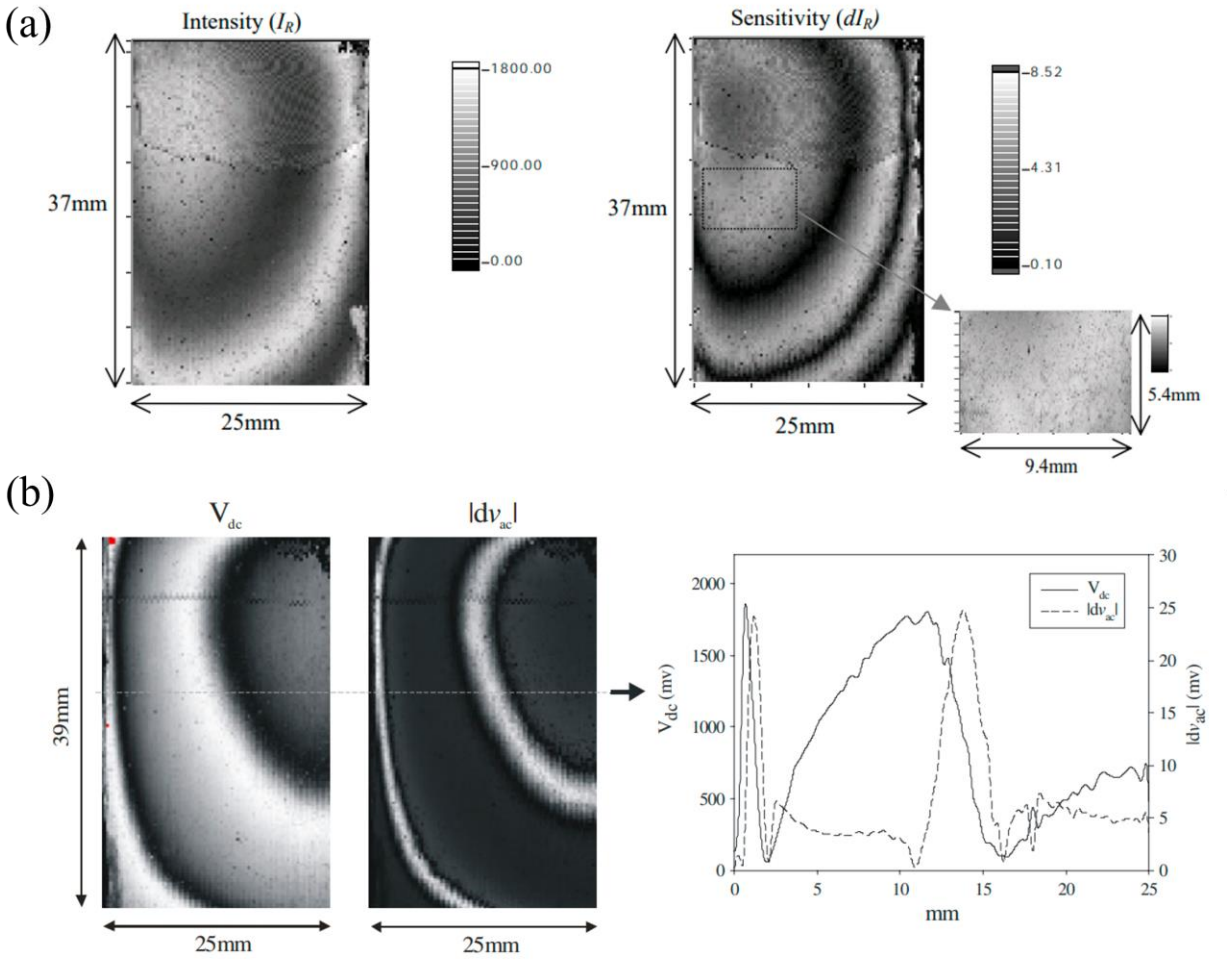

Figure 1.7 Non-uniformity of sensitivity reported in early literatures

Moreover, there is a fundamental constraint of all polymer film-based FP sensors. Since the phase of the cavity is highly sensitive to the film thickness, a thickness variation over the sensor surface will lead to a shift of the ITF curve and thus a non-uniformity in the sensitivity. This phenomenon has already been reported in the early demonstrations of bulky substrate-based sensors, as shown in Figure *1.7* [62], [63]. Concentric fringes are shown when interrogated with a fixed wavelength laser, indicating that there is a systematic thickness variation of the polymer film during fabrication. This is the reason why the later sensors all use a tunable wavelength laser to tune to the optimal wavelength at each location on the sensor head, or to the optimal wavelength

of a fiber-based sensor. This not only increases system cost because a tunable laser is much more expensive than a fixed wavelength laser, but also increases data acquisition time especially when using the sensor array, because the wavelength tuning is required at any location before acquiring any data and all locations have different optimal wavelengths. Thus, a FP sensor with a fixed wavelength interrogation laser is needed to advance the field.

Chapter 2 Specific Aims and Dissertation Overview

2.1 Specific aims

The overall goal of this research is to design and fabricate a miniaturized Fabry-Perot polymer film ultrasound sensor to enable novel photoacoustic endoscopy technologies for early cancer detection and staging. The miniaturized sensor should be able to be implemented into a probe less than 4.2 mm in diameter to perform in vivo mouse colon imaging. The imaging depth should exceed 3 mm into the tissue. The sensor should operate using a single wavelength laser. Imaging performance will be demonstrated using both endogenous contrast agents such as hemoglobin and exogenous contrast agents such as gold nanoparticle.

Specific aim 1: Study the physics of miniaturized FP sensors to see the effect of scale-downed size on detection performance and to verify feasibility of such sensor.

Specific aim 2: Design and fabricate a miniaturized FP sensor that can work with single wavelength interrogation laser while having sufficient sensitivity.

Specific aim 3: Characterize the sensor and demonstrate the imaging performance using a tabletop system.

Specific aim 4: Design a miniaturized PAE probe incorporating the FP sensor and validate its feasibility.

2.2 Dissertation overview

This dissertation is organized in the following order:

Chapter 1 provides a detailed introduction on the big picture of the research field and the state-of-the-art technologies in imaging. The principle of photoacoustic imaging is described, followed by a detailed review of the current PAE systems. The working principle of Fabry-Perot sensor and current miniaturization progress are presented.

Chapter 2 presents the specific aims of this research and provides an overview of the structure of this dissertation.

Chapter 3 describes the design and fabrication of miniaturized FP sensor. An in-depth modeling of the physics of the miniaturized FP sensor is described. Design and fabrication processes are presented. The sensors are characterized after fabrication, and secondary dicing are made possible based on the findings.

Chapter 4 shows the results of characterization of the FP sensors. ITF, detection sensitivity and frequency response are measured.

Chapter 5 presents a photoacoustic tomography imaging system based on a miniaturized Fabry-Perot sensor array. The setup of the system, the scanning strategy and the image reconstruction algorithm are described in detail. The spatial resolutions of the PAT system are measured. The imaging performance is demonstrated by 3-D imaging of absorbing phantoms. With the help of gold nanoshell, ex vivo 3-D imaging of mouse colon tissue is conducted.

Chapter 6 describes the design of a photoacoustic endoscope based on a miniaturized Fabry-Perot single element sensor. The fabrication processes of the sensor are introduced. An excitation light delivering sub-probe of the whole PAE system is fabricated to demonstrate the feasibility of miniaturized FP sensor to work with miniature optics. A tabletop PAI system is built to test the imaging capability of the FP sensor. Phantoms and the ear of a nude mouse are imaged.

Then a new sub-probe using a different excitation laser is constructed to image the prolapsed mouse.

Chapter 7 discusses the achievements, the knowledge gained, and limitations in this research.

Chapter 8 shows some directions for future work on this project.

Chapter 3 Design and Fabrication of Miniaturized Fabry-Perot Sensor

3.1 Selection of polymer material

Before the study and design of the miniaturized Fabry-Perot sensor, it is important to choose the right material for the polymer film. There have been many studies using different materials for the polymer film, including Parylene C (chlorinated poly(para-xylylene)) [54], [64], PET (polyethylene terephthalate) [64], [65], PDMS (polydimethylsiloxane) [66], SU-8 [67], [68] and polyimide [69]. The properties of these materials and the performance of the sensors made from these materials are summarized in Table *1*.

Table 1 Properties of polymers used in FP sensors

Material	**Parylene C**	**PET**	**PDMS**	**SU-8**	**Polyimide**
Density [kg/m3]	1289 [70]	1409.1 [65]	969 [71]	1187 [72]	1420 [72]
Speed of Sound [m/s]	2200 [54]	2200 [65]	1119 [71]	2500 [72]	2620 [72]
Young's Modulus [Pa]	2.8×10^9 [70]	4.4×10^9 [65]	$3.6–8.7\times10^5$ [73]	2.0×10^9 [74]	2.4×10^9 [75]
Thickness [μm]	40 [64] 38 [54] 22 [54]	75 [64] 50 [65]	3 [66]	10 [67] 10 [68]	11 [69]
-3dB Bandwidth [MHz]	17.5 [64] 22 [54] 39 [54]	12.5 [64] 25 [65]	57 (-6dB) [66]	47 (-6dB) [68]	62 (-6dB) [69]
Noise Equivalent Pressure (NEP) [kPa]	8 [64] 0.21 [54] 0.31 [54]	6.5 [64] 10 [65]	20 [66]	2.1 [67] 8.9 [68]	3.3 [69]

The fabrication processes, depending on the materials, can be categorized into three groups. In the first group, commercially available thin PET films are coated with highly reflective mirrors on both sides and glued to a substrate using adhesion materials [64], [65]. The thickness of the purchased film may not be uniform on the scale of optical wavelengths, and the adhesion layer

contributes to even more variation of the total film thickness. This method appeared in early studies and is rarely used in recent research. In the second group, a thin film of polymer is formed by spin coating, and it applies to PDMS [66], SU-8 [67], [68] and polyimide [69]. This method is inexpensive and flexible, but only very thin (<15 μm) films can be formed, causing low sensitivity. A thicker film can only be achieved by slowing down the spinning speed, but the uniformity will be decreased. In the third group, a Parylene C film is formed on the substrate from gas-phase molecules. The film is conformal and has high uniformity, while a thick film can also be formed in this way. The sensitivities are much better than the sensors made from other materials. Given the fact that the densities and speeds of sound in these materials are close to each other, the sensitivity and uniformity become the most important criteria, and Parylene C is chosen as the polymer spacer material for the FP sensor in this dissertation.

3.2 Study of backing thickness by transfer matrix method

To study the effect of the thickness of backing material, we use transfer matrix method to model the system since it is computational efficient for multi-layer structures. It has never been done in the literature because they never considered multi-layer structures for Fabry-Perot sensors. Here we assume the incident wave is a plane wave, and since we are only studying the thickness effect, we assume the lateral size is infinite.

The schematic of the modelling setup is shown in Figure *3.1*. P_0 is the magnitude of the input pressure wave that travels in the positive x direction in tissue and is incident onto the Parylene C-tissue interface at x = 0. P_R is the magnitude of the reflected pressure wave by this interface. P_1 and P_2 represent the magnitudes of the pressure waves travelling in the positive and negative x directions inside of the Parylene C film, which has a thickness of l. Similarly, P_3 and P_4 represent the magnitudes of the pressure waves travelling in the positive and negative x directions inside of

the glass substrate, which has a thickness of H. Finally, P_T is the magnitude of the transmitted pressure wave out of the glass substrate into the air, with no pressure wave travelling in the negative x direction in air. z_1 through z_4 are the acoustic impedances in tissue, Parylene C, glass, and air, respectively. The properties of Parylene C in Table *1* are used in this simulation.

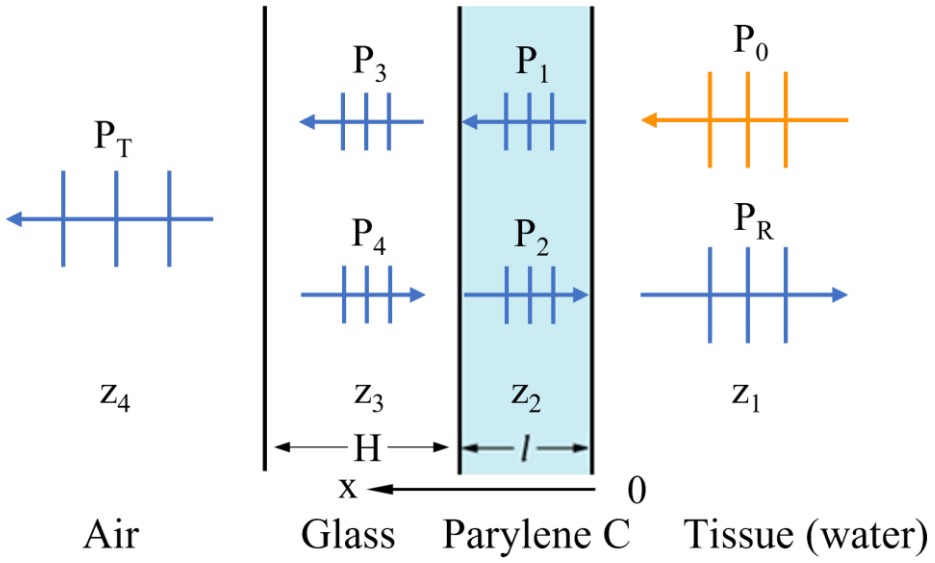

Figure 3.1 Schematic of problem setup for transfer matrix method

The pressures on the two sides of an interface are connected through the boundary conditions:

$$\begin{bmatrix} P(x=0) \\ v(x=0) \end{bmatrix} = \begin{bmatrix} e^{-ik_2 0} & e^{ik_2 0} \\ \frac{1}{z_2} e^{-ik_2 0} & -\frac{1}{z_2} e^{ik_2 0} \end{bmatrix} \begin{bmatrix} P_1 \\ P_2 \end{bmatrix} = \begin{bmatrix} e^{-ik_1 0} & e^{ik_1 0} \\ \frac{1}{z_1} e^{-ik_1 0} & -\frac{1}{z_1} e^{ik_1 0} \end{bmatrix} \begin{bmatrix} P_0 \\ P_R \end{bmatrix}$$

$$\begin{bmatrix} P(x=l) \\ v(x=l) \end{bmatrix} = \begin{bmatrix} e^{-ik_3 l} & e^{ik_3 l} \\ \frac{1}{z_3} e^{-ik_3 l} & -\frac{1}{z_3} e^{ik_3 l} \end{bmatrix} \begin{bmatrix} P_3 \\ P_4 \end{bmatrix} = \begin{bmatrix} e^{-ik_2 l} & e^{ik_2 l} \\ \frac{1}{z_2} e^{-ik_2 l} & -\frac{1}{z_2} e^{ik_2 l} \end{bmatrix} \begin{bmatrix} P_1 \\ P_2 \end{bmatrix}$$

$$\begin{bmatrix} P(x=l+H) \\ v(x=l+H) \end{bmatrix} = \begin{bmatrix} e^{-ik_4(l+H)} & e^{ik_4(l+H)} \\ \frac{1}{z_4} e^{-ik_4(l+H)} & -\frac{1}{z_4} e^{ik_4(l+H)} \end{bmatrix} \begin{bmatrix} P_T \\ 0 \end{bmatrix} = \begin{bmatrix} e^{-ik_3(l+H)} & e^{ik_3(l+H)} \\ \frac{1}{z_3} e^{-ik_3(l+H)} & -\frac{1}{z_3} e^{ik_3(l+H)} \end{bmatrix} \begin{bmatrix} P_3 \\ P_4 \end{bmatrix}$$

where P(x) is the total pressure at position x, while v(x) is the velocity of the particle at position x.

From these equations we have:

$$\begin{bmatrix} P_1 \\ P_2 \end{bmatrix} = \begin{bmatrix} e^{-ik_2 0} & e^{ik_2 0} \\ \frac{1}{z_2} e^{-ik_2 0} & -\frac{1}{z_2} e^{ik_2 0} \end{bmatrix}^{-1} \begin{bmatrix} e^{-ik_1 0} & e^{ik_1 0} \\ \frac{1}{z_1} e^{-ik_1 0} & -\frac{1}{z_1} e^{ik_1 0} \end{bmatrix} \begin{bmatrix} P_0 \\ P_R \end{bmatrix} = \begin{bmatrix} 1 & 1 \\ \frac{1}{z_2} & -\frac{1}{z_2} \end{bmatrix}^{-1} \begin{bmatrix} 1 & 1 \\ \frac{1}{z_1} & -\frac{1}{z_1} \end{bmatrix} \begin{bmatrix} P_0 \\ P_R \end{bmatrix}$$

$$\begin{bmatrix} P_3 \\ P_4 \end{bmatrix} = \begin{bmatrix} e^{-ik_3 l} & e^{ik_3 l} \\ \frac{1}{z_3} e^{-ik_3 l} & -\frac{1}{z_3} e^{ik_3 l} \end{bmatrix}^{-1} \begin{bmatrix} e^{-ik_2 l} & e^{ik_2 l} \\ \frac{1}{z_2} e^{-ik_2 l} & -\frac{1}{z_2} e^{ik_2 l} \end{bmatrix} \begin{bmatrix} P_1 \\ P_2 \end{bmatrix}$$

$$\begin{bmatrix} P_T \\ 0 \end{bmatrix} = \begin{bmatrix} e^{-ik_4 (l+H)} & e^{ik_4 (l+H)} \\ \frac{1}{z_4} e^{-ik_4 (l+H)} & -\frac{1}{z_4} e^{ik_4 (l+H)} \end{bmatrix}^{-1} \begin{bmatrix} e^{-ik_3 (l+H)} & e^{ik_3 (l+H)} \\ \frac{1}{z_3} e^{-ik_3 (l+H)} & -\frac{1}{z_3} e^{ik_3 (l+H)} \end{bmatrix} \begin{bmatrix} P_3 \\ P_4 \end{bmatrix}$$

Thus,

$$\begin{bmatrix} P_T \\ 0 \end{bmatrix} = \begin{bmatrix} e^{-ik_4 (l+H)} & e^{ik_4 (l+H)} \\ \frac{1}{z_4} e^{-ik_4 (l+H)} & -\frac{1}{z_4} e^{ik_4 (l+H)} \end{bmatrix}^{-1} \times \begin{bmatrix} e^{-ik_3 (l+H)} & e^{ik_3 (l+H)} \\ \frac{1}{z_3} e^{-ik_3 (l+H)} & -\frac{1}{z_3} e^{ik_3 (l+H)} \end{bmatrix}$$

$$\times \begin{bmatrix} e^{-ik_3 l} & e^{ik_3 l} \\ \frac{1}{z_3} e^{-ik_3 l} & -\frac{1}{z_3} e^{ik_3 l} \end{bmatrix}^{-1} \times \begin{bmatrix} e^{-ik_2 l} & e^{ik_2 l} \\ \frac{1}{z_2} e^{-ik_2 l} & -\frac{1}{z_2} e^{ik_2 l} \end{bmatrix} \times \begin{bmatrix} 1 & 1 \\ \frac{1}{z_2} & -\frac{1}{z_2} \end{bmatrix}^{-1} \times \begin{bmatrix} 1 & 1 \\ \frac{1}{z_1} & -\frac{1}{z_1} \end{bmatrix} \times \begin{bmatrix} P_0 \\ P_R \end{bmatrix}$$

$$= \begin{bmatrix} T_{11} & T_{12} \\ T_{21} & T_{22} \end{bmatrix} \begin{bmatrix} P_0 \\ P_R \end{bmatrix} = T \begin{bmatrix} P_0 \\ P_R \end{bmatrix}$$

where $T = \begin{bmatrix} T_{11} & T_{12} \\ T_{21} & T_{22} \end{bmatrix}$ is defined as the transfer matrix of the system.

We then have $0 = T_{21} P_0 + T_{22} P_R$, which gives $P_R = -\frac{T_{21}}{T_{22}} P_0$

Then P_1 and P_2 can be calculated as:

$$\begin{bmatrix} P_1 \\ P_2 \end{bmatrix} = \begin{bmatrix} 1 & 1 \\ \frac{1}{z_2} & -\frac{1}{z_2} \end{bmatrix}^{-1} \begin{bmatrix} 1 & 1 \\ \frac{1}{z_1} & -\frac{1}{z_1} \end{bmatrix} \begin{bmatrix} P_0 \\ P_R \end{bmatrix}$$

$$P_1 = \frac{1}{2}\left[\left(1+\frac{z_2}{z_1}\right)P_0 + \left(1-\frac{z_2}{z_1}\right)P_R\right] = \frac{1}{2}\left[\left(1+\frac{z_2}{z_1}\right) - \frac{T_{21}}{T_{22}}\left(1-\frac{z_2}{z_1}\right)\right]P_0$$

$$P_2 = \frac{1}{2}\left[\left(1-\frac{z_2}{z_1}\right)P_0 + \left(1+\frac{z_2}{z_1}\right)P_R\right] = \frac{1}{2}\left[\left(1-\frac{z_2}{z_1}\right) - \frac{T_{21}}{T_{22}}\left(1+\frac{z_2}{z_1}\right)\right]P_0$$

Finally, the thickness change of the Parylene C film can be calculated as:

$$\Delta l(\omega) = \frac{\left(P_1 e^{-ik_2 l} - P_2 e^{ik_2 l}\right) - (P_1 - P_2)}{\omega z_2} = \frac{e^{-ik_2 l} - 1}{\omega z_2}\left(P_1 + P_2 e^{ik_2 l}\right)$$

$$= \frac{e^{-ik_2 l} - 1}{2\omega z_2}\left\{\left[\left(1+\frac{z_2}{z_1}\right) - \frac{T_{21}}{T_{22}}\left(1-\frac{z_2}{z_1}\right)\right] + e^{ik_2 l}\left[\left(1-\frac{z_2}{z_1}\right) - \frac{T_{21}}{T_{22}}\left(1+\frac{z_2}{z_1}\right)\right]\right\}P_0 = F(\omega)P_0(\omega)$$

where F(ω) is defined as the frequency response of the multi-layer sensor. As can been seen, the induced thickness change in frequency domain is simply the frequency response of the sensor multiplied by the spectrum of the input ultrasound signal. The thickness change in time domain can be calculated by taking the inverse Fourier transform of the thickness change in frequency domain.

A MATLAB (The MathWorks, Inc.) program is developed to calculate this thickness change thanks to its effective matrix calculations. The transfer matrix T is looping through different layers, so the program can be applied to structures with any number of layers, including the simplest case when there are only tissue, Parylene C and infinite thick glass layers.

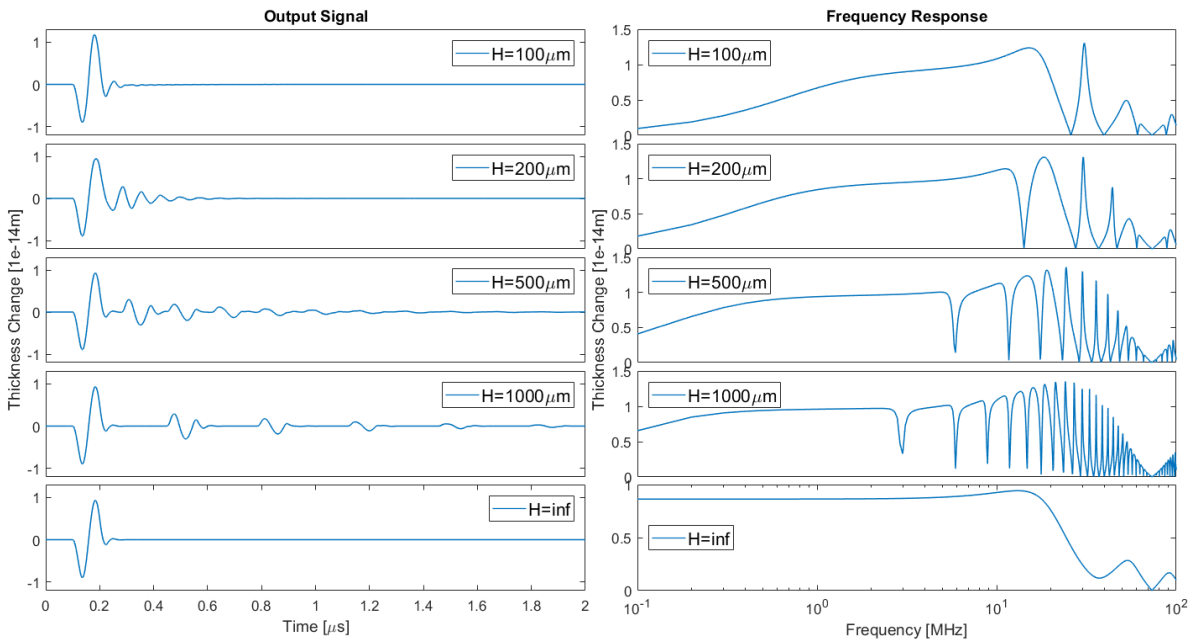

Figure 3.2 Time and frequency domain responses of FP sensors with finite thickness substrates

Now we need to validate the model. We use a one cycle of 10 MHz sine wave as the input ultrasound signal from the tissue. Figure *3.2* shows the output thickness changes and corresponding sensor frequency responses when changing the thickness of the glass substrate. The infinite-thick sensor agrees with the result calculated using the method proposed by Beard et al [53]. However, the frequency responses of the sensors with finite thicknesses exhibit quite different patterns compared to the one with infinite thickness. It is easier to explain in the time domain. The finite thickness of the substrate appears to introduce multi-reflection of the pressure wave inside of the substrate, which appears in the form of "echoes". By measuring the time interval between the echoes, we can find that it is equal to the time of flight of pressure wave that travels a round trip inside of the substrate, i.e., $\Delta t = 2H/c_3$. This roughly proves that the introduction of the finite thickness of the substrate merely results in echoes of the input signal. As the substrate gets thinner, the echoes first come closer and closer to the main signal which represents the thickness change induced by the incident pressure wave itself. After a certain point, the echoes merge into the main

signal and appear to become the ring-down response of the vibration of the main signal. As the substrate keeps getting thinner, the glass layer will become acoustically thin enough for the pressure wave to transmit, and the echoes will disappear.

3.3 Approximate model of sensor frequency response based on multi-reflection

As mentioned in Section 0, the time-of-flight method to prove the multi-reflection physics.is not accurate. A theoretical model predicting this behavior will deepen the understanding of the working principle of such miniaturized sensors.

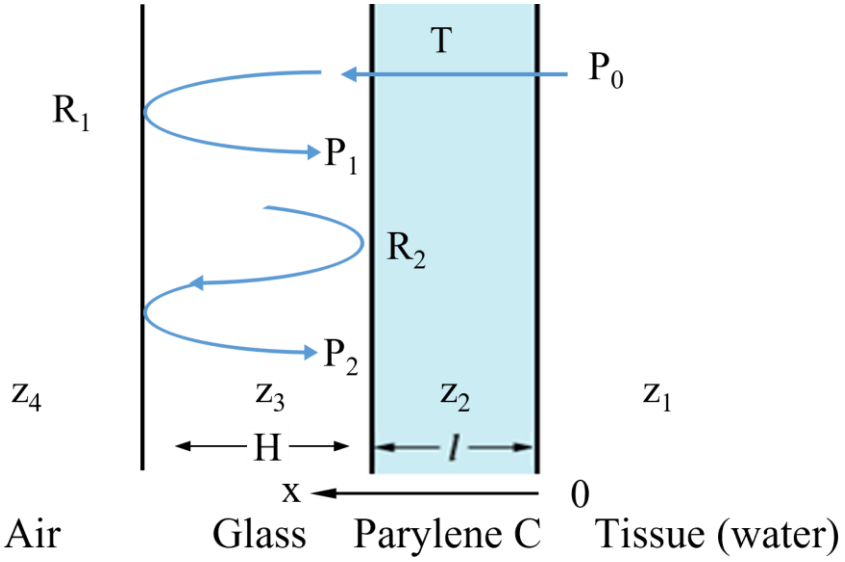

Figure 3.3 Problem setup for approximate modeling of finite thickness substrate

Since the model of the frequency response of a Fabry-Perot sensor with infinitely thick substrate is well studied, it will be convenient to develop the model for finite-thick substrate based on that. Figure *3.3* shows the schematic of the problem setup. After the main ultrasound wave P_0 induces a thickness change of the Parylene C film, it transmits into the glass substrate, gets reflected by the glass-air interface, and travels back to the glass-Parylene C interface as P_1. A secondary thickness change is induced by this reflected pressure wave, while this wave is reflected

again by the glass-Paryelen C interface. This pressure wave keeps being reflected inside of the glass substrate and forms an echo signal.

In Figure *3.3*, T represents the acoustic transmission coefficient between the Parylene C-glass interface, R_1 represents the reflection coefficient between the air-glass interface, and R_2 represents the reflection coefficient between the glass-Parylene C interface. The expression of the transmission coefficient T can be derived explicitly using the transfer matrix method in Section 0 when the glass is infinitely thick. The expression is:

$$T = \frac{2z_3}{z_1} e^{ik_3 l} \frac{1}{\left(1+\frac{z_3}{z_1}\right)\cos(k_2 l) + i\left(\frac{z_2}{z_1}+\frac{z_3}{z_2}\right)\sin(k_2 l)}$$

Similarly, the explicit expressions of R_1 and R_2 are:

$$R_1 \approx -e^{-2ik_3(H+l)}$$

$$R_2 = -e^{2ik_3 l} \frac{\left(1-\frac{z_1}{z_3}\right)\cos(k_2 l) + i\left(-\frac{z_2}{z_3}+\frac{z_1}{z_2}\right)\sin(k_2 l)}{\left(1+\frac{z_1}{z_3}\right)\cos(k_2 l) + i\left(\frac{z_2}{z_3}+\frac{z_1}{z_2}\right)\sin(k_2 l)}$$

Note the expression of R_1 is approximated by assuming the acoustic impedance of the air is much smaller than that of the glass. There is one more thing that needs to be considered. Since the reflected pressure wave hits the glass-Parylene C interface from the glass side, so the induced thickness change of the Parylene C film even by the same unit pressure wave will be different from that coming from the tissue side. The thickness change of the Parylene C induced by a unit pressure wave from the tissue side is:

$$\Delta l_0 = -\frac{4i\sin\left(\frac{1}{2}k_2 l\right)}{\omega z_2} \frac{\frac{z_3}{z_1}\cos\left(\frac{1}{2}k_2 l\right) + i\frac{z_2}{z_1}\sin\left(\frac{1}{2}k_2 l\right)}{\left(1+\frac{z_3}{z_1}\right)\cos(k_2 l) + i\left(\frac{z_2}{z_1}+\frac{z_3}{z_2}\right)\sin(k_2 l)}$$

Note this expression is actually the frequency response F(ω) of the Fabry-Perot sensor with infinitely thick substrate. Similarly, the thickness change induced by a unit pressure wave from the glass side is:

$$\Delta l_1 = -\frac{4i\sin\left(\frac{1}{2}k_2 l\right)}{\omega z_2} e^{ik_3 l} \frac{\frac{z_1}{z_3}\cos\left(\frac{1}{2}k_2 l\right) + i\frac{z_2}{z_3}\sin\left(\frac{1}{2}k_2 l\right)}{\left(1+\frac{z_1}{z_3}\right)\cos(k_2 l) + i\left(\frac{z_2}{z_3}+\frac{z_1}{z_2}\right)\sin(k_2 l)}$$

Now define η to be the ratio between the thickness changes caused by incident waves from glass and tissue side. Thus,

$$\eta = \frac{\Delta l_1}{\Delta l_0}$$

$$= e^{ik_3 l} \frac{\frac{z_1}{z_3}\cos\left(\frac{1}{2}k_2 l\right) + i\frac{z_2}{z_3}\sin\left(\frac{1}{2}k_2 l\right)}{\left(1+\frac{z_1}{z_3}\right)\cos(k_2 l) + i\left(\frac{z_2}{z_3}+\frac{z_1}{z_2}\right)\sin(k_2 l)} \frac{\left(1+\frac{z_3}{z_1}\right)\cos(k_2 l) + i\left(\frac{z_2}{z_1}+\frac{z_3}{z_2}\right)\sin(k_2 l)}{\frac{z_3}{z_1}\cos\left(\frac{1}{2}k_2 l\right) + i\frac{z_2}{z_1}\sin\left(\frac{1}{2}k_2 l\right)}$$

The total pressure P_G inside of the glass is the sum of all the reflected pressure waves, and can be calculated as:

$$P_G = P_1 + P_2 + P_3 \ldots = P_1 + P_1 R_1 R_2 + P_1 (R_1 R_2)^2 + \cdots = P_1 \sum_{n=0}^{\infty} (R_1 R_2)^n = P_1 \frac{1}{1 - R_1 R_2}$$

$$= P_0 T R_1 \frac{1}{1 - R_1 R_2}$$

Now the total thickness change of a sensor with a glass substrate, Δl, can be written as the sum of the thickness changes Δl_0 induced by P_0 and Δl_G induced by P_G:

$$\Delta l = \Delta l_0 + \Delta l_G$$

Since Δl_0 is proportional to P_0 and Δl_G is proportional to P_G, using η we have defined:

$$\Delta l = \Delta l_0 + \Delta l_0 T R_1 \eta \frac{1}{1 - R_1 R_2} = \Delta l_0 \left(1 + \frac{T R_1 \eta}{1 - R_1 R_2}\right)$$

Thus Δl can be written as $\Delta l(\omega) = F_H(\omega)\Delta l_0(\omega)$, where $F_H(\omega) = 1 + \frac{TR_1\eta}{1-R_1R_2}$ is defined as a frequency domain filter that converts the original sensor frequency response $\Delta l_0(\omega)$ to that of the new finite thickness sensor $\Delta l(\omega)$. After plugging in the expressions of the coefficients and simplify the result, the explicit expression of $F_H(\omega)$ is:

$$F_H(\omega) = \frac{1 - e^{-2ik_3H}\dfrac{z_3 \cos\left(\frac{1}{2}k_2 l\right) - iz_2 \sin\left(\frac{1}{2}k_2 l\right)}{z_3 \cos\left(\frac{1}{2}k_2 l\right) + iz_2 \sin\left(\frac{1}{2}k_2 l\right)}}{1 - e^{-2ik_3H}\dfrac{\left(1 - \frac{z_1}{z_3}\right)\cos(k_2 l) + i\left(-\frac{z_2}{z_3} + \frac{z_1}{z_2}\right)\sin(k_2 l)}{\left(1 + \frac{z_1}{z_3}\right)\cos(k_2 l) + i\left(\frac{z_2}{z_3} + \frac{z_1}{z_2}\right)\sin(k_2 l)}}$$

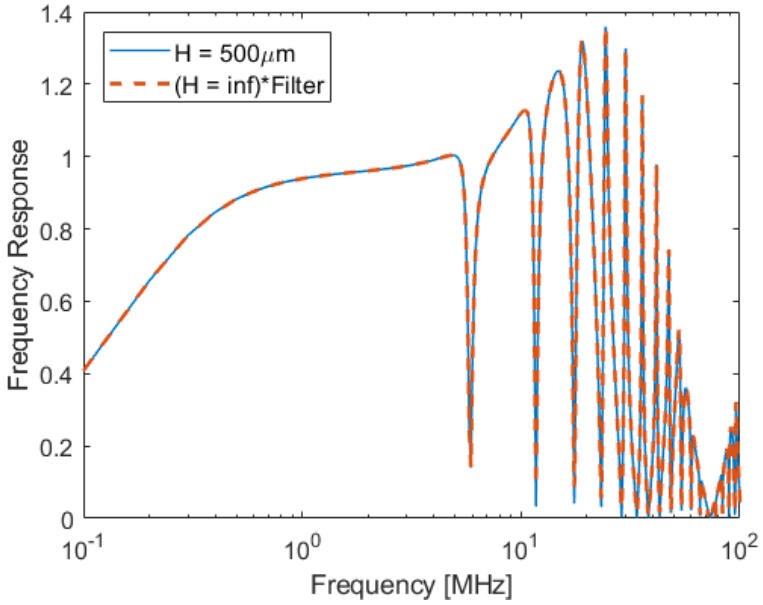

Figure 3.4 Comparison of frequency responses of a 500 μm substrate FP sensor and the product of the frequency response of an infinitely thick sensor and the 500 μm filter

We can see that the frequency response of the finite thickness sensor is simply that of the infinitely thick sensor multiplied by the filter $F_H(\omega)$. This reveals the intrinsic connection of the

new response to the original response. Thus, the time domain signal from the finite thickness sensor can be converted back to the signal from the infinitely thick sensor by simply dividing $F_H(\omega)$ from the spectrum of the signal. This provides a promising approach to remove the echo signals.

To verify the derivation of the filter, we multiply the frequency response of the infinite thick sensor by the filter in the MATLAB program and plot it along the calculated frequency response of a finite thickness sensor in the same figure, Figure *3.4*. The two frequency responses overlap perfectly, showing that the frequency response of the finite thickness sensor is indeed the product of the derived filter and the response of the original infinitely thick sensor.

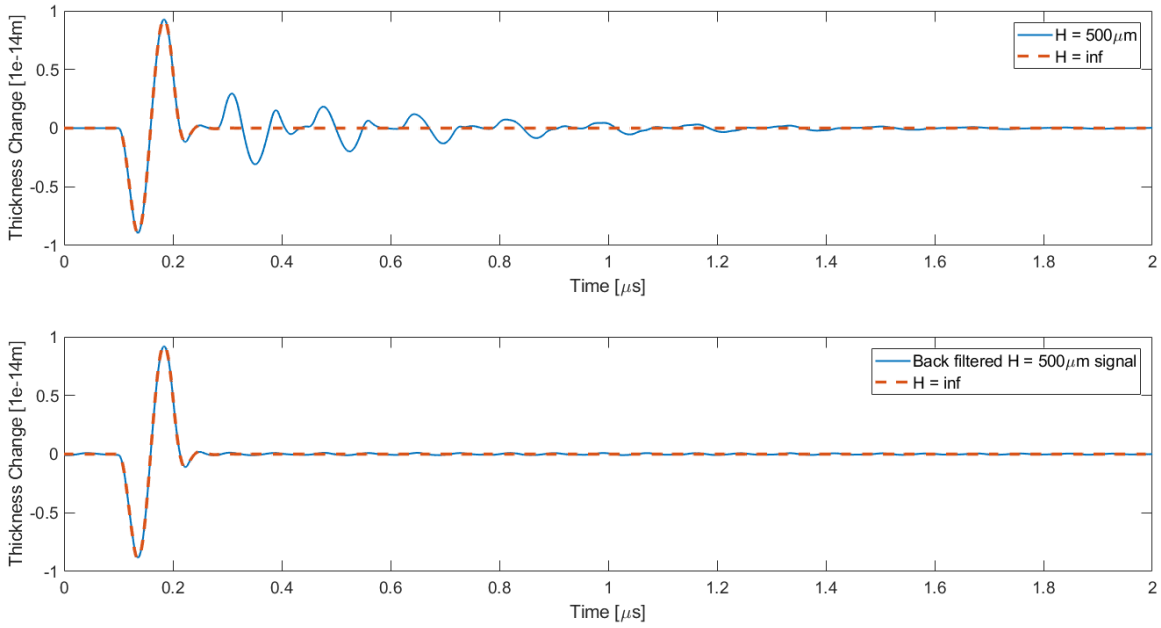

Figure 3.5 Back-filtered signal from a 500 μm FP sensor and the signal of an infinitely thick sensor

Also, we try to remove the echo signals by dividing the filter from the spectrum of the signal. Figure *3.5* shows the signals of the 500um thick sensor before and after filtering and the signal from the infinitely thick sensor. We can see that the filtered signal gets rid of the echoes and matches the original signal very well. This shows that theoretically the echoes introduced by the

thickness of the substrate can be removed by back filtering, thus simplifying the considerations in substrate designs.

3.4 Analysis of the influence of lateral sizes

As shown in Section 3.2, the thickness of the substrate has a fundamental impact on the frequency response of the miniaturized FP sensor. It was assumed that the lateral size of the FP sensor did not affect the vibration of the Parylene C film, and plane waves were used to model the pressure waves inside of the layers. However, in reality, the miniaturized sensor also has a finite lateral size, and its effect may not be ignored. Since the geometry is much more complicated than the 1-D thickness mode vibration modeled before, a finite element analysis (FEA) is conducted using COMSOL Multiphysics (COMSOL Inc.). Figure *3.6* shows the 2-D simulation setup. The Parylene C film and the glass substrate are mounted between air and water. The water domain has a depth of 2 mm while the air domain has a depth of 0.1 mm. The lengths and thicknesses of the Parylene C film and the glass substrate are changed according to the specific simulation. The lateral sizes of the water and air domains are 1 mm wider than the Parylene C and the glass. Three physics are used in this simulation. The “Solid Mechanics” physics is applied to the Parylene C film and the glass substrate. Specifically, they are modeled as “Linear Elastic Material” and have “Initial Values” of 0. “Fixed Constraint” is applied to the sides of them to model rigid mounting. “Pressure Acoustics, Transient” physics is applied to the water and air domains. Specifically, they are modeled as “Transient Pressure Acoustics Model” and have “Initial Values” of 0. The regions besides the Parylene C film and the glass substrate are modeled as “Sound Hard Boundary (Wall)” to indicate the rigid mounting. The bottom of the air domain is modeled as “Plane Wave Radiation”, and an incident pressure wave is modeled at the top of the water domain by “Pressure” and is a one-cycle 10 MHz sine wave as before. Finally, “Acoustic-Structure Boundary”

multiphysics is applied to the Parylene C-water and glass-air interfaces. A “Time Dependent” study is conducted to find the thickness change of the Parylene C film at the center point. Figure *3.6* (a) shows a representative simulation when the Parylene C and glass have a lateral size of 1 mm, while the water and air domain have a lateral size of 2 mm.

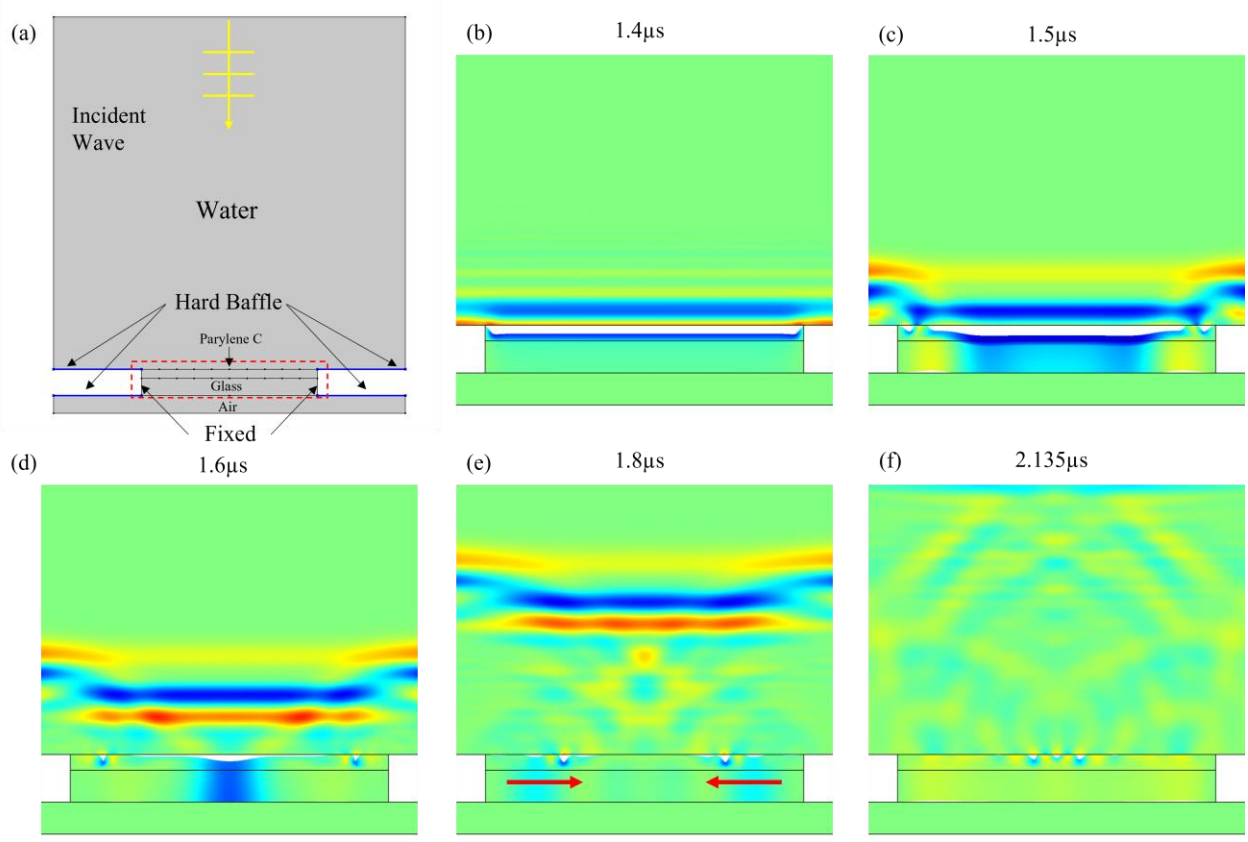

Figure 3.6 Modeling setup and simulation results at different times

Figure *3.6* (b) to (e) show the deformation of the Parylene C film at different times. About 1.4 μs after the firing of the incident pressure wave, it arrives at the Parylene C-water interface and creates the initial thickness change. This is the main signal of the FP sensor. Then as shown in Figure *3.6* (c), in addition to the multi-reflection of the pressure wave inside of the glass substrate, since the edge of the Parylene C film is fixed, there is also an induced deformation in the lateral direction. This initial deformation then propagates towards the center of the FP sensor as side waves, as shown in (d) and (e). The red arrows in (e) indicate the directions of the

propagation. Figure *3.6* (f) shows the time at 2.135 μs when these side waves meet at the center of the FP sensor. This is when the thickness change at the center caused by the side waves reaches the maximum amplitude. The side waves then keep propagating and gradually die down.

The thickness change is modeled by the difference between the displacements of the center points at the Parylene C-water interface and Parylene C-glass interface. Now the model is ready and different parameters are analyzed on the effect of the side wave. The first parameter is the thickness of the glass substrate. Figure *3.7* shows the thickness changes of the center points of 1 mm long, 50 μm Parylene C sensors with 0.5 mm, 0.2 mm and 0.1 mm substrates. It can be seen that the magnitude of the side wave is comparable to the main signal, creating an undesirable artifact signal. The thickness of the glass, however, does not affect the side wave. This shows that this side wave depends on the parameters of the Parylene C film, while the substrate thickness affects the multi-reflection echo signals.

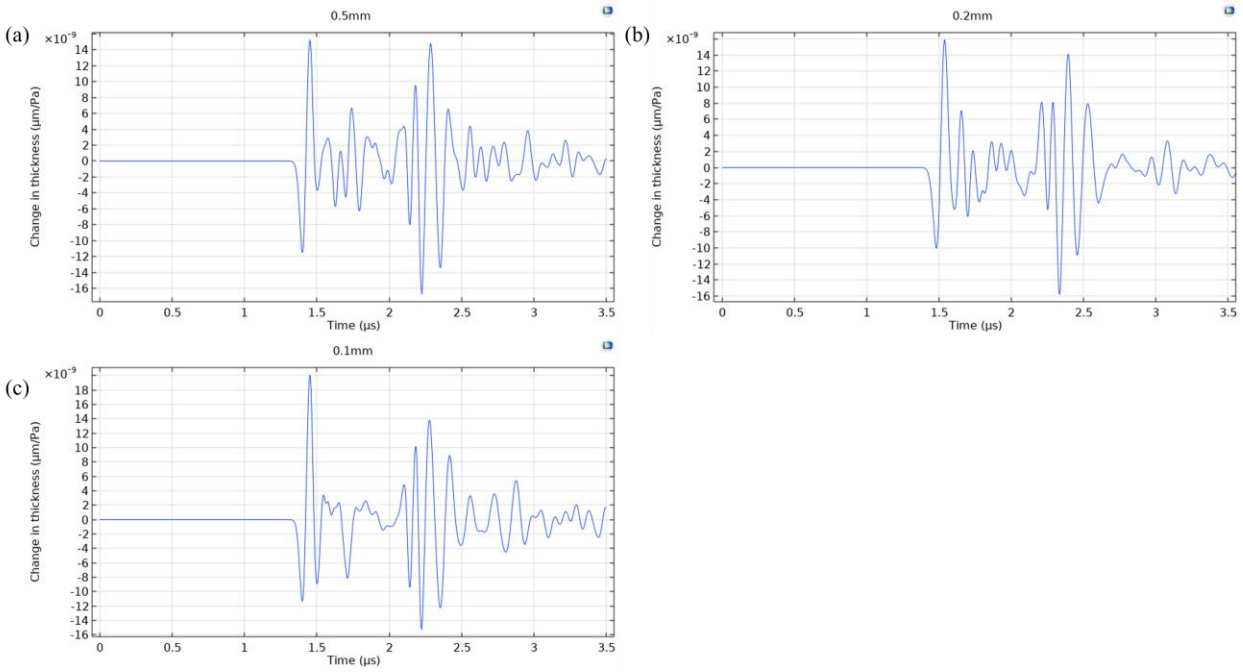

Figure 3.7 Parylene C thickness changes of sensors with different glass substrate thicknesses

The second parameter studied is the lateral size of the sensor. Figure *3.8* shows the thickness changes of 0.2 mm thick, 50 µm Parylene C sensors with 1 mm, 2 mm, 3 mm and 4 mm lateral sizes. The glass is chosen to be 0.2 mm thick to make the echo signals merge with the main signal, thus distinguishing them from the side waves in the time domain data. The side wave appears in later time when the lateral size of the sensor is larger, since it takes more time for the waves to travel to the center of the sensor. The magnitude of the side wave is also smaller for longer sensors because of the smaller stiffness. Thus, a sensor with a larger lateral size is preferred to reduce the side waves, which creates constraints on miniaturization of the sensor.

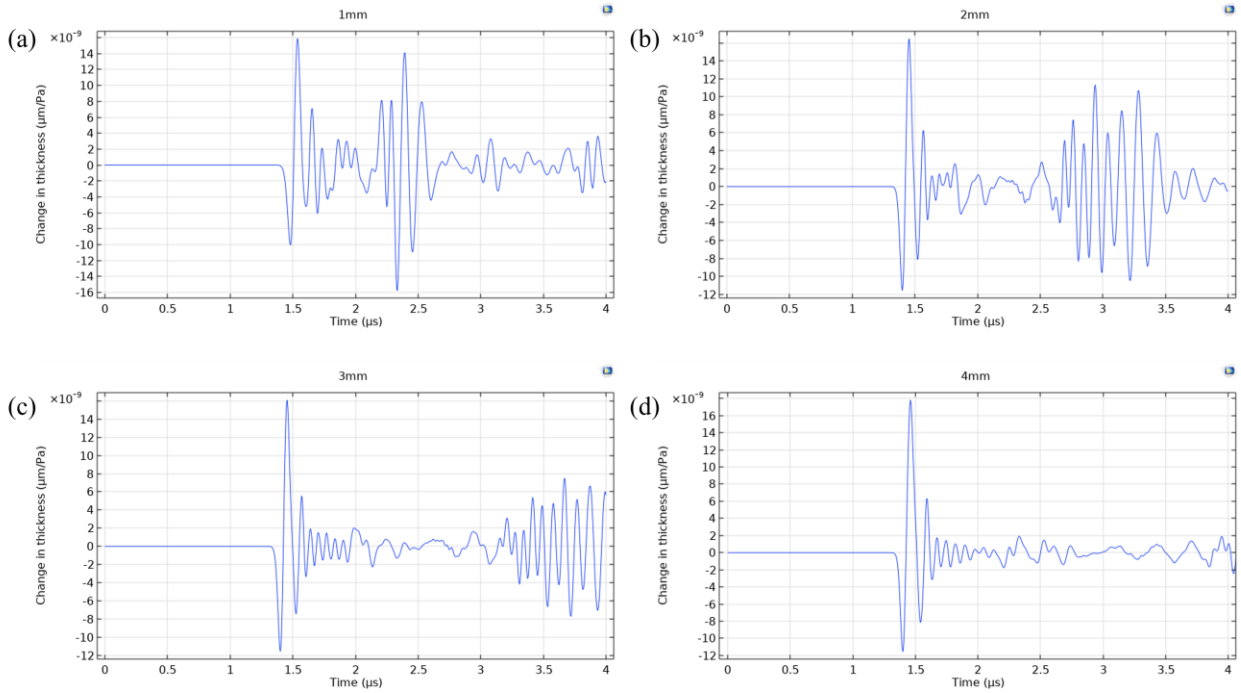

Figure 3.8 Parylene C thickness changes of sensors with different lateral sizes

The third parameter studied is the thickness of the Parylene C film. Figure *3.9* shows the thickness changes of 2 mm long, 0.2 mm thick sensors with Parylene C thicknesses of 50 µm, 40 µm, 30 µm, 20 µm and 10 µm. It can be seen that as the thickness of the Parylene C film gets thinner, the magnitude of the side wave decreases and finally becomes reasonably insignificant compared to the main signal. However, the absolute magnitude of the main signal also decreases

due to the decrease in Parylene C film. Thus, eliminating the side wave will come with a sacrifice of sensor sensitivity in this way.

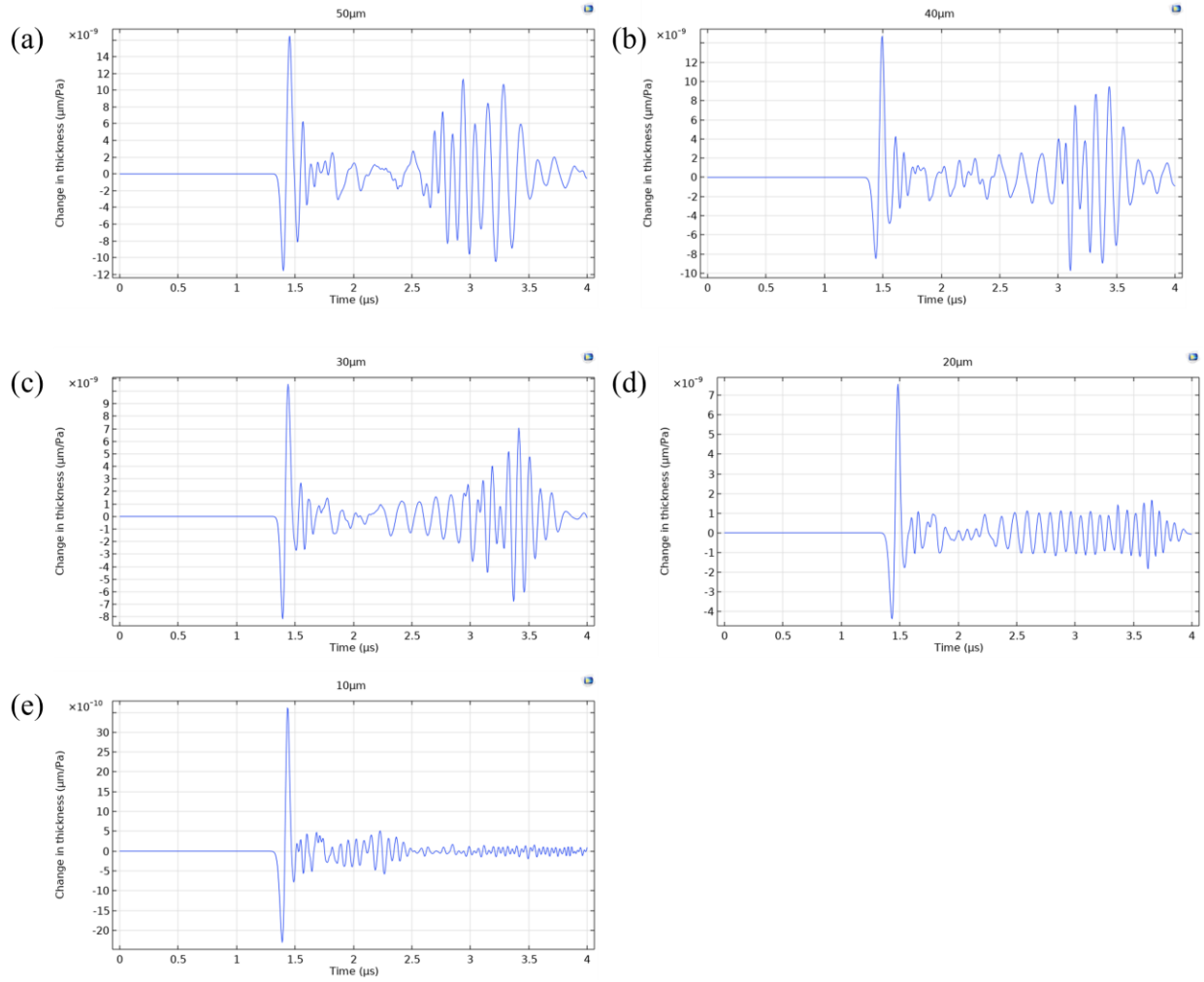

Figure 3.9 Parylene C thickness changes of sensors with different Parylene C thicknesses

The last parameter studied is the averaging length on the Parylene C film, because the interrogation laser beam has a finite size and the acquired signal is the average of the thickness changes in this area. Figure *3.10* shows the thickness changes of 2 mm long, 0.2 mm thick, 50 µm Parylene C sensors with line averaging lengths of 50 µm, 100 µm, 200 µm and 500 µm. It can be seen that the side wave is significantly reduced when using a 100 µm or 200 µm averaging length, while it can be almost eliminated when using an averaging length of 500 µm. Thus, the side wave

can be effectively eliminated using a focused beam with relatively large diameter, or directly using a collimated beam of the interrogation laser. Compared to the others, this method can eliminate the side wave without changing the dimensions of the sensor, thus making miniaturization of the sensor possible.

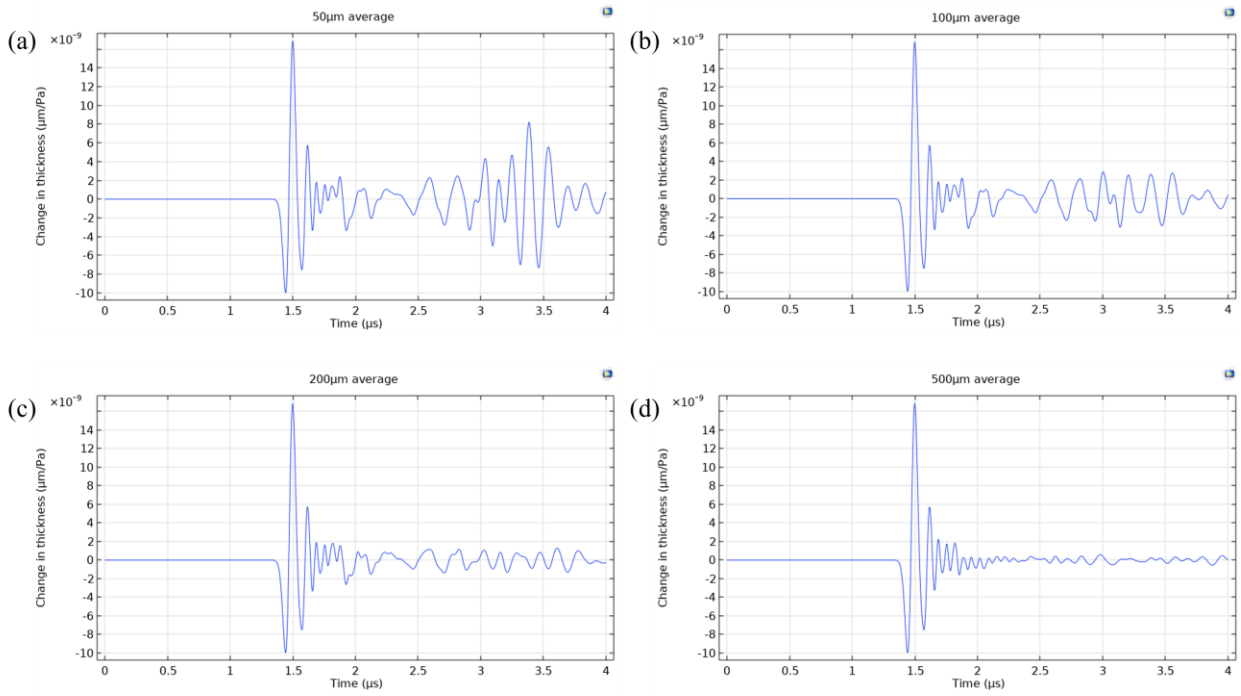

Figure 3.10 Parylene C thickness changes of sensors with different averaging lengths

3.5 Gold reflective mirror modeling, verification, and design

Fabry-Perot interferometer-based ultrasound sensor operates with highly reflective mirrors to get high sensitivity. For the purpose of proof of concept, we start the first version of our senor with gold coatings as reflective mirrors, and helium-neon (He-Ne) laser for detection due to its great coherence length. Gold mirrors exhibit high reflectivity in red and near infrared wavelengths, but still have absorptions due to the complex refractive index. Since the mirrors in Fabry-Perot interferometer need to be partial reflective, which is achieved by changing the thickness of the gold coating, a model that calculates the reflectivity from the film thickness is needed to select the best film thickness.

The refractive index of an absorbing medium is complex, which can be written as **n** = n – ik [76], where n is the common refractive index and k is the extinction or absorption coefficient. Both these values vary with the thickness of the medium when it's in the form of a thin film and they are different from those of a bulky material. To develop a model that can accurately calculate the complex refractive index given the film thickness, the data from the study on gold film by Krautkramer [77] is used to calculate the refractive index at 632.8 nm of He-Ne laser. The values of n and k of gold films with different thicknesses are measured at 600 nm and 700 nm, so the refractive index at 632.8 nm is interpolated from the two values at 600 and 700 nm. Since this study only measured the films thinner than about 275 Å, the refractive indices of thicker films are calculated from the data by McPeak et al [78].

After finding the complex refractive index of the gold film, it can be used to calculate the reflection and transmission coefficients of the film. As shown in Figure *3.11* (a), for a film with thickness d and refractive index $\mathbf{n_1}$, the reflection and transmission coefficients from medium n_0 to medium n_2 are:

$$r = \frac{(n_0 - \boldsymbol{n_1})(\boldsymbol{n_1} + n_2)e^{i\delta} + (n_0 + \boldsymbol{n_1})(\boldsymbol{n_1} - n_2)e^{-i\delta}}{(n_0 + \boldsymbol{n_1})(\boldsymbol{n_1} + n_2)e^{i\delta} + (n_0 - \boldsymbol{n_1})(\boldsymbol{n_1} - n_2)e^{-i\delta}}$$

$$t = \frac{4n_0\boldsymbol{n_1}}{(n_0 + \boldsymbol{n_1})(\boldsymbol{n_1} + n_2)e^{i\delta} + (n_0 - \boldsymbol{n_1})(\boldsymbol{n_1} - n_2)e^{-i\delta}}$$

where $\boldsymbol{n_1} = n_1 - ik_1$ is the complex refractive index of the film, and $\delta = \frac{2\pi}{\lambda}\boldsymbol{n_1} d\cos\theta$ is the one-way phase change inside of the film.

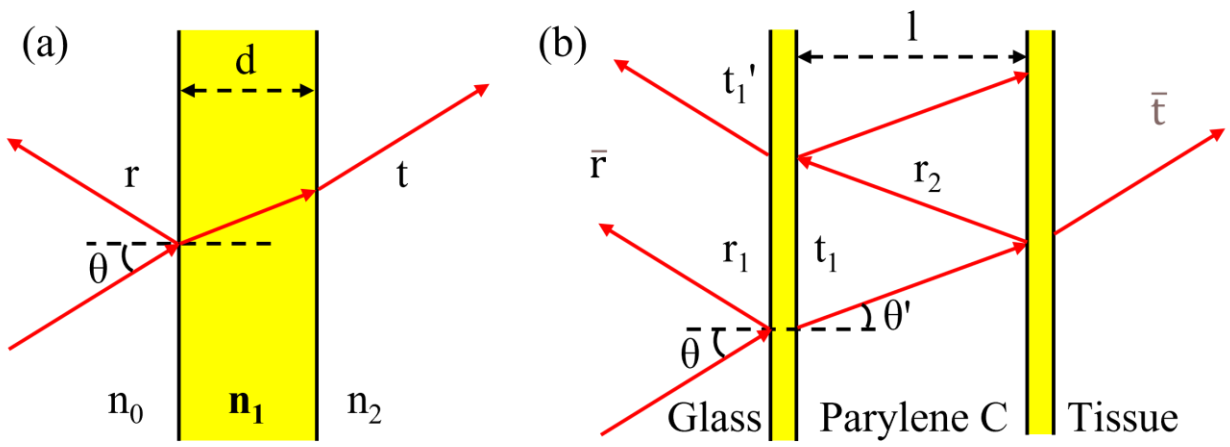

Figure 3.11 Working principle of gold film as reflective mirror

The complete optical model of the interferometer is built upon the complex reflection and transmission coefficients of the gold film, as shown in in Figure *3.11* (b). r_1 is the reflection coefficient of the first gold film between glass and Parylene C, t_1 is the transmission coefficient through the film from glass to Parylene C, t_1' is the transmission coefficient through the film from Parylene C to glass, and r_2 is the reflection coefficient of the second gold film between Parylene C and tissue. The optical properties of tissue are approximated by those of water. The overall reflection coefficient at the glass-gold interface is:

$$\bar{r} = r_1 + \frac{t_1 t_1' r_2 e^{-2i\phi}}{1 + r_1 r_2 e^{-2i\phi}}$$

where $\phi = \frac{2\pi}{\lambda} n_p l \cos\theta'$ is the one-way phase change inside of the Parylene C film and n_p is the refractive index of Parylene C.

The total reflectance R can then be calculated by: $R = |\bar{r}|^2$. The plot of R with respect to the wavelength of the incident laser is called the interferometer transfer function (ITF) of the sensor.

3.6 Fabrication of the miniaturized FP sensor

To achieve miniaturization of FP sensor array, first a thin substrate needs to be selected instead of a bulky substrate already reported in literature. Here a borosilicate wafer with 100 mm diameter and 500 µm thickness is used as the sensor's substrate. A 10 Å layer of titanium is first deposited onto the glass substrate as an adhesion layer using a magnetron sputtering tool (Lab 18-2, Kurt J Lesker Company). It is followed by sputtering a 32.8 nm gold and another layer of 10 Å titanium adhesion layer. Then a 32 µm thick layer of Parylene C is vacuum deposited onto the first gold layer (PDS 2035, Specialty Coating Systems Inc.). This thickness is chosen to have a target bandwidth of 20 MHz based on simulation using the method described in Section 0. Another 10 Å titanium and 100 nm thick gold are sputtered on top of the Parylene C as the second reflective mirror. The wafer is then spin coated (CEE 200X, Brewer Science) with a layer of photoresist (SPR 220 (3.0), Dow Inc.) at a speed of 2000 rpm, resulting in a 3.2 µm protective layer for later dicing operations. The wafer is finally partially diced into 10 mm square pieces with 200 µm thick substrate remaining for further measurements (ADT 7100 Dicing Saw, Advanced Dicing Technologies Ltd.). The fabrication process is illustrated in Figure *3.12*.

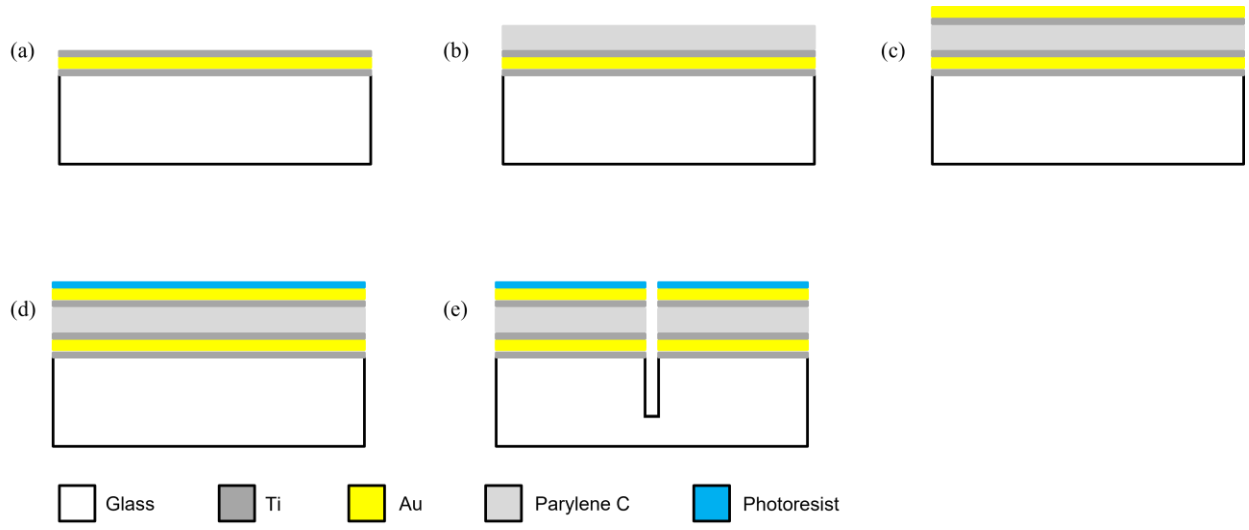

Figure 3.12 Fabrication process of the miniaturized FP sensor

3.7 Characterization of sensor surface sensitivities

Although Parylene C can form highly conformal coatings, the coating thickness still slightly varies on the surface of a flat backing substrate, especially on the scale of optical wavelengths. This leads to a shift of FP interferometer transfer function (ITF), resulting in a variation of the optimal interrogation wavelength across the surface of the sensor, or a variation of sensitivity when using a fixed wavelength laser. This phenomenon has already been reported in literature [62], [63]. This is the reason why a tunable wavelength laser is usually used to optimize the interrogation wavelength on different locations on FP sensors, leading to an increase in data acquisition time and a reduction in frame rate. Whether these variations still exist in a miniaturized Fabry-Perot sensor remains unclear and needs to be investigated.

After the wafer is coated as described in Section 3.6, the whole wafer is diced into 10mm by 10mm squares for more convenient measurements. Figure *3.13* shows a schematic of the setup for characterizing surface sensitivities of the sensors. The 10 mm piece is taped onto a hollow 3D-printed holder that is mounted onto the side wall of a water tank. The glass substrate side is in contact with air while the coating side is in contact with water inside of the tank. The water tank is placed on a linear stage with three DC servo actuators (CONEX-TRA12CC, Newport) controlled by a desktop computer.

A 5 mW 633 nm continuous wave He-Ne laser (30990, REO) is used as the interrogation source due to its good coherence. Its output is modulated by a neutral-density filter (NDC-50C-2M, Thorlabs). The laser beam is directed to a beam expander comprising lenses L1 and L2 by a pair of mirrors M1 and M2. The expanded beam is directed to a galvanometer mirror (6200H Optical Scanners, Cambridge Technology) by mirror M3. A 75 mm achromatic lens L3 (AC508-075-A, Thorlabs) is placed after the galvanometer mirror such that the galvanometer mirror is at

the left focal point of the lens. In this way the chief rays of the focused beams coming out of the lens are always perpendicular to the lens as the galvanometer mirror scans the incident collimated beam. The focused laser beam is incident onto the glass backing side of the FP sensor. The sensor is placed at a small angle to the norm of the incident beam such that the reflected beam is slightly above the incident beam. The reflected beam is picked up by the same lens L3 and gets directed by the galvanometer mirror and mirror M3. Mirror M4 is placed right above the incident beam and picks up the reflected beam after M3. The reflected beam is then further directed by mirror M5 and focused onto an AC-coupled low noise photoreceiver (1801, New Focus) by a lens L4.

A 10 MHz unfocused ultrasound transducer (V312-SU, Olympus) is used as the ultrasound source to test the Fabry-Perot sensor, and it is controlled by a pulser-receiver (PR5073, Olympus). The sensor is raster scanned together with the tank while the transducer and the interrogation laser are kept stationary. The ac-coupled output of the photodetector is acquired by an NI FPGA module (PXIe-7962R, National Instruments) with an 80 MS/s digitizer adapter module (NI 5732, National Instruments). The data is temporally stored on the memory of the FPGA module and then transferred to a host computer for further processing. On the same chassis (NI PXIe-1073, National Instruments) a NI PXI analog output module (NI PXI-6711, National Instruments) is used to generate the analog control signal of the galvanometer mirror and the trigger signal for the pulser-receiver for synchronization. A LabVIEW (National Instruments) program is developed to control the actuators, the galvanometer mirror, the data acquisition system, and the trigger signals.

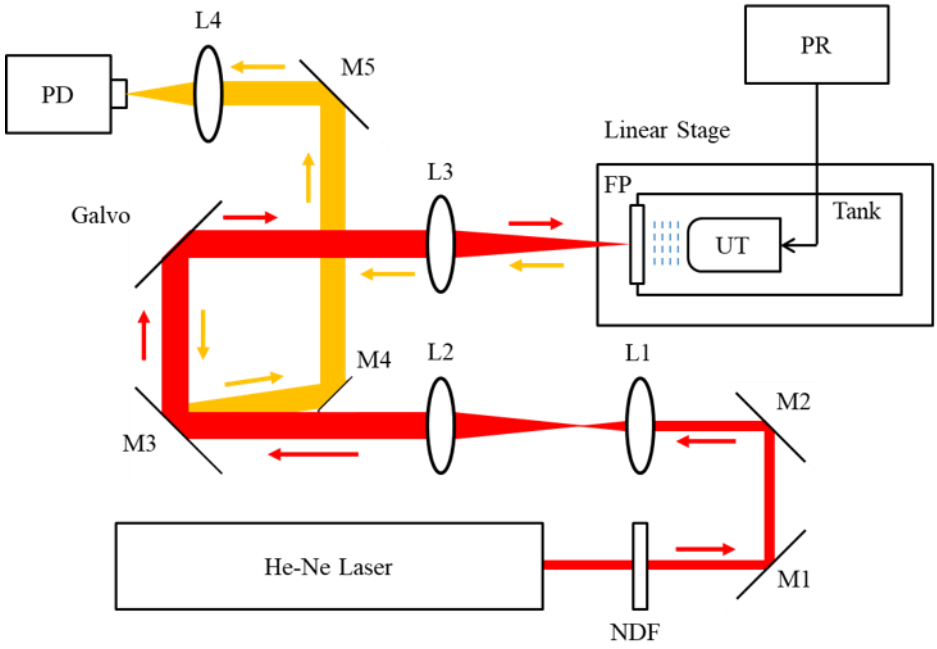

Figure 3.13 Schematic of system setup for FP sensor testing

The time-domain signal acquired by the photodetector represents the response of the sensor under the modulation of the incident ultrasound wave. The peak-to-peak voltage of the output of the photodetector is used as the sensitivity at each location during scanning. The sensitivity maps of each of the 10 mm sensors are measured one after one, and they are shown in Figure *3.14* (b), which are placed in the same order as they were before being removed from the wafer.

It can be seen that the sensitivities of the sensors are not uniform. When measured by a single wavelength laser, the fringes indicate that the thickness of the Parylene C film, which is half of the optical path length, varies with an amount of half of interrogation wavelength between each two fringes. This thickness variation is smooth across the wafer with an obvious concentric pattern. A reasonable explanation of the cause of the concentric thickness variation is that the wafer spins slowly inside of the chamber during Parylene C deposition. Since the Parylene C coating is formed by the monomer gas inside of the chamber, there will be a relative speed between the wafer surface and the gas due to the rotation of the wafter. This speed is proportional to the distance from the

rotating axis, so the gas molecules face uniformly changing speeds across the surface of the substrate. Relative speed will affect the deposition of the gas molecules, resulting in a change of coating thickness. Another observation is that the patterns on adjacent sensors are continuous, meaning that dicing won't change the thickness distribution of the polymer film. This also suggests that dicing the 10 mm sensors into even smaller pieces is possible, meaning that miniaturized sensors may be fabricated from selected 10 mm square pieces.

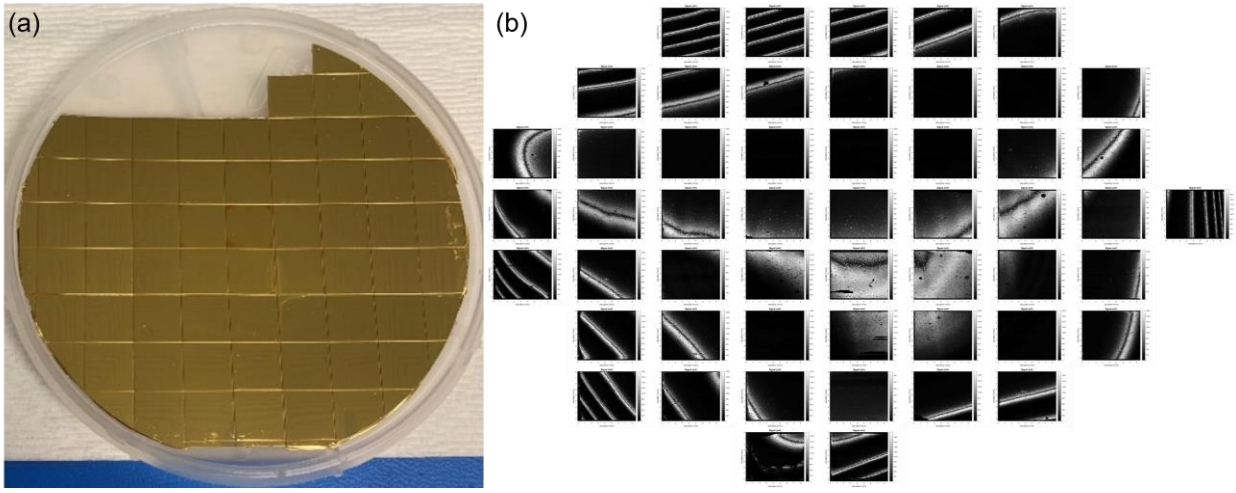

Figure 3.14 Photo of fabricated FP sensors and surface sensitivity maps

The patterns agree with the observations reported in literatures, showing that this is a common phenomenon in flat substrate based Fabry-Perot sensors, regardless of the thickness of the substrate. This is the reason why a tunable laser is needed to interrogate the wavelength at different locations on the sensor. While it seems to cause a problem in bulky 2-D FP sensor array, it actually indicates promising aspects in fabricating miniaturized sensors. By selecting and scanning along a relatively straight region of the most sensitive parts on the sensor when measured with a fixed wavelength laser, a 1-D array is formed without changing the wavelength. Without the thickness gradient, the thickness may end up in the relatively flat region of ITF when using a fixed wavelength laser, resulting in low detection sensitivity. Thus, the thickness variation is essential to generating a usable area. Since the focus point of the interrogation laser is negligible

compared to the dimension of the sensor, the lateral size of such 1-D array can be on the sale of millimeter or even smaller. Such 1-D array is sufficient to form 2-D images and is a promising candidate to fit into an endoscopic form factor. Note that this miniaturization is made possible by using a thin substrate and dicing it, which is impossible when using bulky substrates. In essence, finding the regions with the highest sensitivity is equivalent to tuning to the wavelength with maximum slope on the ITF. Thus, a tunable laser can be replaced by a fixed wavelength laser, reducing data acquisition time and system complexity.

3.8 Secondary dicing and surface sensitivity measurements

As shown in the previous section, a relatively straight region of usable area can be formed due to the thickness gradient of the Parylene C film. By choosing the proper 10 mm square piece and further dicing it according to the fringe pattern on it, a rectangular sensor can be fabricated with relatively uniform surface sensitivity. Figure *3.15* (a) shows the detailed surface sensitivity map of a selected square sensor with relatively straight sensitive region. The dashed lines in the figure show the upper bound, lower bound and centerline of the target dicing area. This sensor is then diced into 9 mm by 2 mm rectangle pieces according to the location of the target region. Figure *3.15* (b) shows a photo of the sensor after dicing. The red arrow indicates the targeted area in (a). Figure *3.15* (c) shows the surface sensitivity map of the indicated miniaturized sensor in (b) measured with raster scanning. It can be seen that the straight region is safely kept after dicing. Figure *3.15* (d) shows the values of peak-to-peak voltage of photodetector output along selected horizontal lines in (c). Multiple lines having relative uniform sensitivity and length greater than 6 mm can be found in the figure, showing that this sensor provides a promising 1-D sensor array with relatively uniform sensitivity. Finally, the selected rectangular miniaturized sensor is soaked

with isotone and IPA successively to remove the previously coated photoresist and a 4 μm Parylene C is deposited on it the as a protection layer.

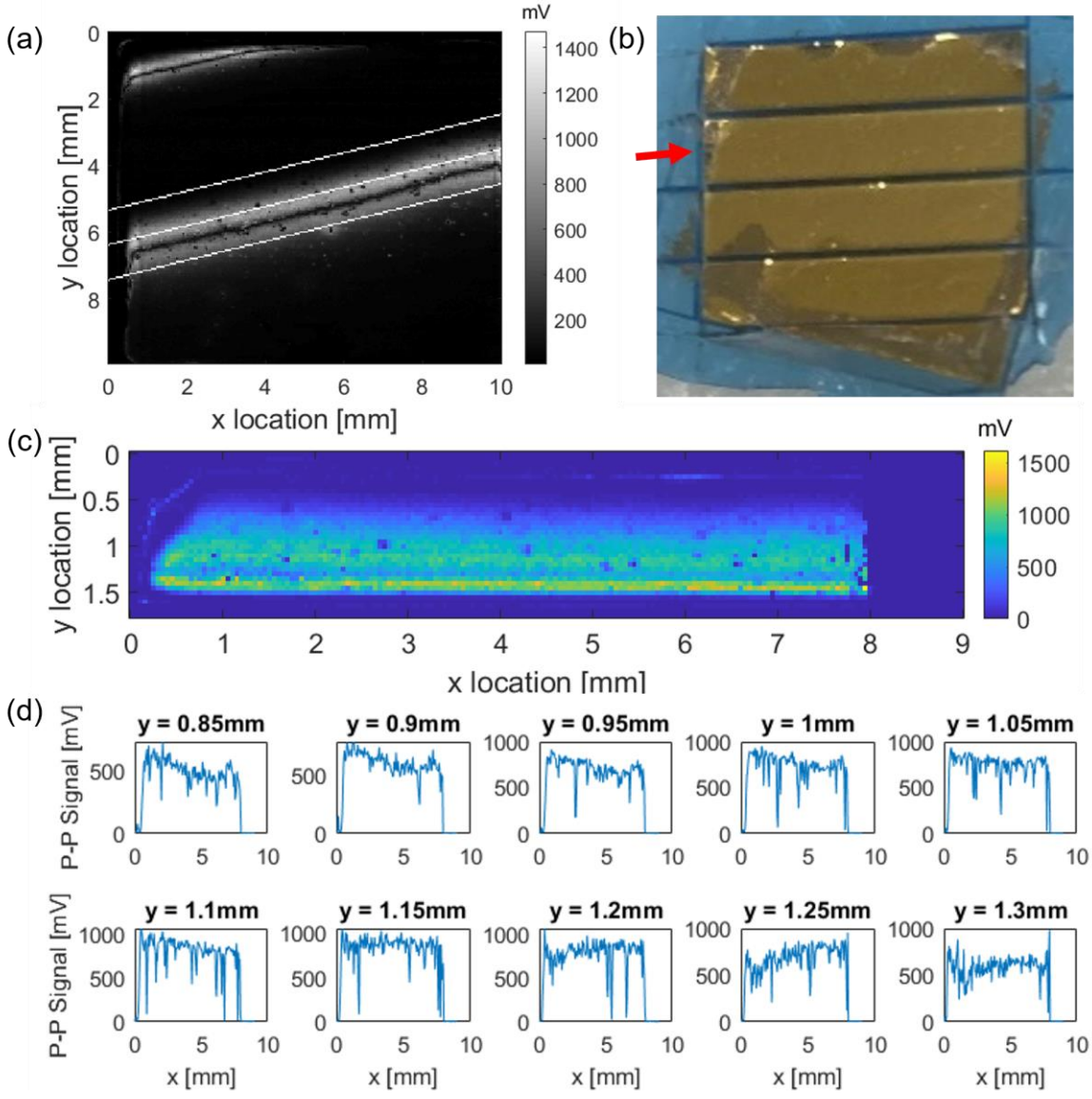

Figure 3.15 Results of secondary dicing

Chapter 4 Characterization of Miniaturized FP Sensors

4.1 Sensor ITF measurement

To verify the design of gold coatings as highly reflective mirrors in the Fabry-Perot interferometer, the ITF of the sensor should be measured with a tunable laser in a range around the targeting wavelength of 633 nm, which is the wavelength of the He-Ne laser in the experimental setup. Unfortunately, due to a lack of appropriate tunable laser near 633 nm, an external cavity diode laser (TLB-6700 Velocity, New Focus) with a wavelength range of 765-781 nm is used instead to measure the ITF as an approximation of the sensor performance in the vicinity of 633 nm. The collimated beam coming out of the laser is directly incident onto the glass side of the sensor and the reflected beam is detected by a power meter. Figure *4.1* (a) shows the measured data and simulation results according to the coating design targeted at 633 nm. It can be seen that the match is very good. Figure *4.1* (b) shows a detailed measurement of the ITF in the range of 777-781nm. The measured data is also fitted with an asymmetric Lorentzian model, and the full width at half-maximum (FWHM) of the ITF is about 0.3 nm. The sharp curve shows that high finesse is successfully achieved by highly reflective gold coatings. The asymmetric shape of the ITF can be explained by the accumulation of Gouy phase shift from the uncollimated light beam that comes out directly from the tunable laser, and it has been reported in literature [41].

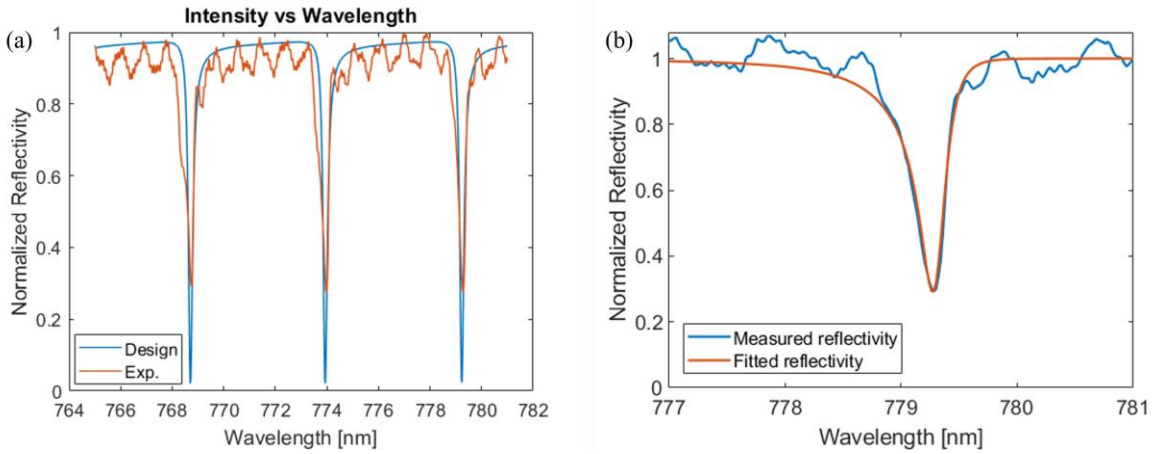

Figure 4.1 ITF measurement of the FP sensor in the vicinity of 770 nm

4.2 Detection sensitivity of the sensor

The detection sensitivity is represented by the noise-equivalent pressure (NEP), which is defined as the minimum detectable acoustic pressure that gives a unity system SNR [53]. Thus, it can be calculated by

$$NEP = \frac{N}{V/P}$$

where N is the peak-to-peak voltage of noise, V is the peak-to-peak voltage of the measured signal induced by the incident ultrasound wave, and P is the pressure of the incident ultrasound wave.

To measure the NEP of the FP sensor, the same 10 MHz unfocused ultrasound transducer (V312-SU, Olympus) is used as the acoustic source. Since the output ultrasound signal of the transducer driven by a pulser receiver (5073PR, Olympus) is too strong and makes the output from the Fabry-Perot sensor saturate the amplified photodetector, a function generator (33600A, Keysight) is used to drive the ultrasound transducer instead of the pulser-receiver. The function generator drives the transducer with a 3-cycle sine wave burst with a frequency of 10MHz and an amplitude of 10V. The resulting pressure wave is calibrated by a needle hydrophone (HNC−1500,

ONDA). The rectangular sensor is line scanned against the transducer and the waveforms acquired by the photodetector are recorded to calculate the NEP. The peak-to-peak voltage of the total acquired signal and the peak-to-peak voltage of the first hundreds of data points before the main signal are used to calculate the SNR then the NEP. The best NEP is found to be 0.76 kPa, while the average NEP along the scanning line of the sensor is 1.12 kPa.

The results are compared with other FP sensors in the literature, as summarized in Table *2*. It can be seen that the bulky sensor has a better NEP, but the size is too large. Meanwhile, the fiber bundle sensor has a similar NEP. The single fiber sensor is extremely sensitive, because it uses a concave resonant cavity to achieve better interference. However, the single element sensor configuration cannot be used in tomography. Also, all of the other FP sensors rely on a tunable laser.

Table 2 Comparison with other sensors in PAI systems

Type of Sensor	**NEP**	**Dimensions**	**Features**
Wafer-based Mini FP	0.76 kPa (best) 1.12 kPa (average)	9 mm×2 mm×0.54 mm	Fixed wavelength laser Mini sensor array
Bulky Substrate FP [54]	0.21 kPa (38 μm) 0.31 kPa (22 μm)	50 mm×30 mm×11.5 mm	Tunable laser Bulky
Fiber Bundle FP [41]	0.5–1.26 kPa	3.2 mm diameter	Tunable laser Rigid and small Mini sensor array
Single Fiber FP [61]	9.3 Pa	125 μm diameter	Tunable laser Flexible and small Highly sensitive Concave cavity
Commercial UT (Blatek)	3.75 kPa	0.48mm×0.47mm×0.2mm	Opaque and small
Commercial UT (Blatek) with 60dB Amplifier	0.21 kPa		

The NEP of a commercially available ultrasound transducer (AT27470, Blatek) which has been widely demonstrated in PAE systems in the literature is also measured. It gives the worst

NEP if an amplifier is not used, while the NEP is good if a 60dB amplifier is used. However, it is an opaque single element sensor. In summary, the proposed wafer-based miniaturized FP sensor has a moderate sensitivity which can still be improved in the future. The advantages are that it can be made into miniaturized sensor array, and it can work with single wavelength interrogation laser.

4.3 Frequency response

To verify the acoustic design, it's important to measure the frequency response of the sensor. As shown in Section 3.3, the frequency response of the miniaturized sensor is simply that of a sensor with infinitely thick substrate multiplied by a filter introduced by the finite thickness of the backing substrate. This effect appears as a series of echo signals in the time domain. Thus, a simply way to process the signal is to leave out the echo signals and just analyze the spectrum of the main signal at the beginning.

The frequency response is measured by Fourier transforming the acquired main signal by the sensor from a known incident ultrasound wave and dividing the spectrum of the known ultrasound signal. The same 10 MHz unfocused ultrasound transducer is used, whose own spectrum is measured beforehand by the pulse-receive method. Figure *4.2* (a) shows the spectrum of the signal of the ultrasound transducer acquired by the pulse-receive method, and its square root is calculated as the real spectrum of the ultrasound wave. Figure *4.2* (b) shows the spectrum of the main signal acquired by the FP sensor. Figure *4.2* (c) shows the measured frequency response of the sensor, with a -3dB bandwidth of 16.6 MHz. The theoretical frequency response simulated using a model given in [53] is also shown in Figure *4.2* (c). It can be seen that the model predicts a -3dB of 20.3 MHz, which is the design target. The measured bandwidth is only about 82% of the design target, and it may result from several factor. It may attribute to a lack of high frequency components of the source ultrasound transducer, of which the central frequency is only 10 MHz.

The low-frequency responses, however, fits the simulation well. It may also result from the discrepancy between the physical properties used in the simulation and the real properties of the sensor. Another cause would be the deviation of the Parylene C thickness from the target thickness due to a lack of precise control of the deposition thickness of the process.

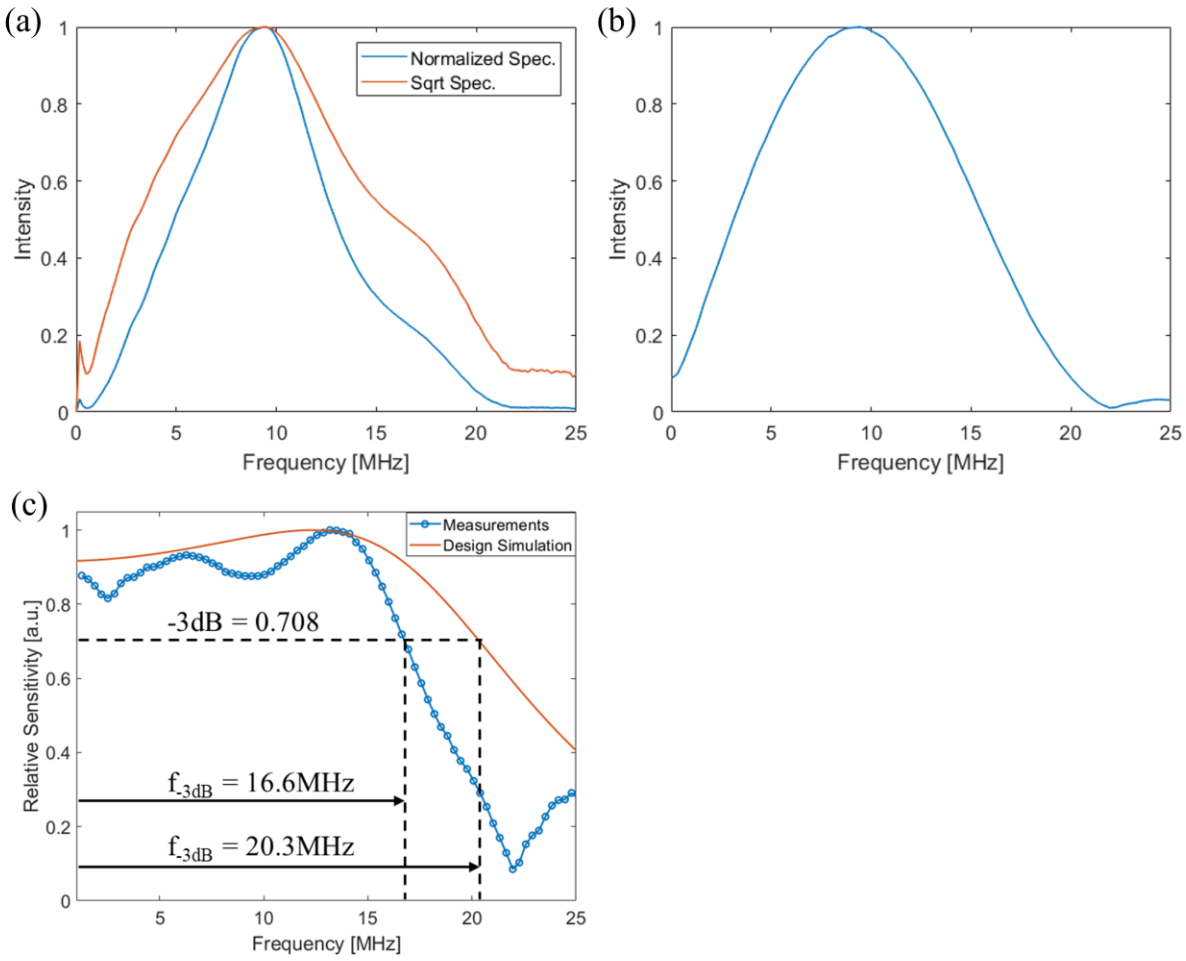

Figure 4.2 Frequency response measurement of the sensor

4.4 Elimination of side waves using a collimated interrogation beam

As shown in Section 3.4, the lateral sizes of the miniaturized FP sensor will have side waves in addition to the main signal and the echoes caused by the finite thickness substrate. As shown in Figure *3.10*, the side waves can be effectively eliminated using a large diameter focused beam or a collimated beam. Figure *4.3* (a) shows a representative sensitivity map of a 10 mm

sensor. Figure *4.3* (b) shows the time domain signal at the location indicated by the red dot at the center of the circle in Figure *4.3* (a). The focused beam size is 121 μm, which will be described in more details in Section 5.2. It can be seen that the signals after the main signal are quite random without a clear pattern. They should be the superposition of the echoes caused by the substrate and the side waves caused by lateral size. The ratio between the magnitudes of the potential side waves and the main signal is close to that shown in Figure *3.10* (b). Now a collimated beam with diameter of 1.5 mm is used for the interrogation laser. The output signal is the averaged intensity change in the area illuminated by the beam. Figure *4.3* (c) shows the time domain signal acquired by the collimated beam of which the center is at the same location as the focused beam in Figure *4.3* (b). It can be seen that the side waves are effectively eliminated, while the echoes with a clear periodical pattern which are caused by the substrate remain. Thus, the side waves are no longer an issue if large diameter beams or collimated beams are used. This is especially useful for single element sensors since no focusing is required.

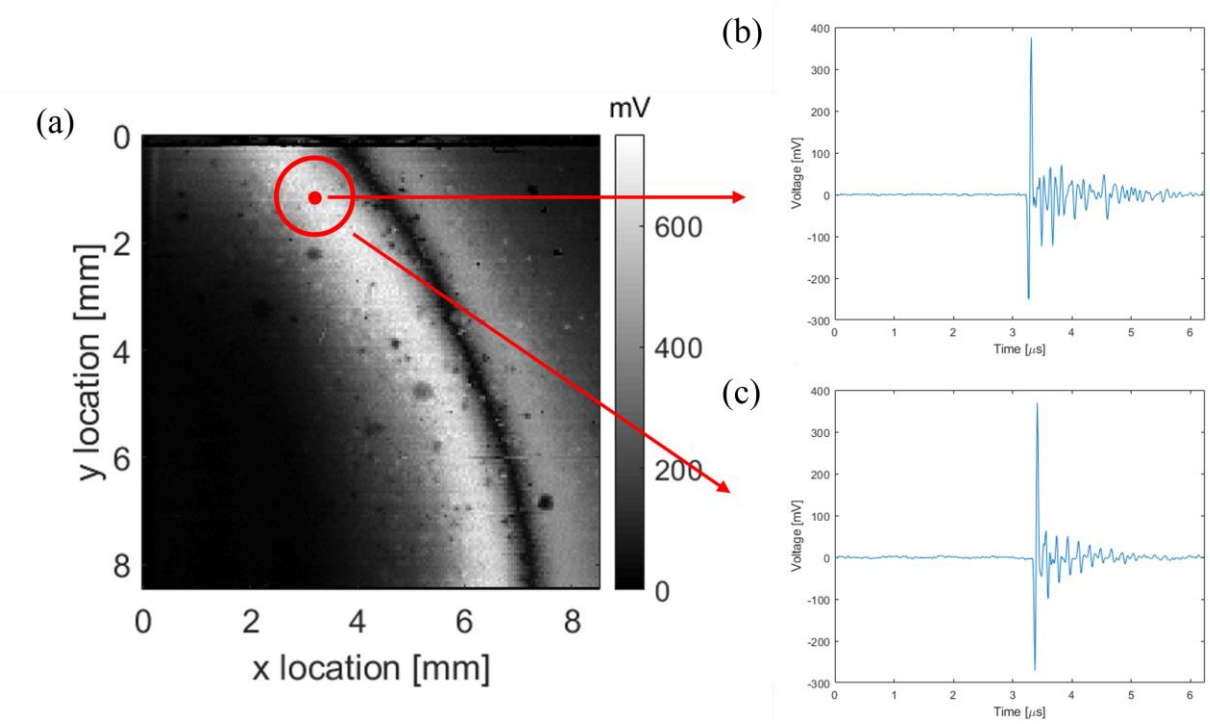

Figure 4.3 Time domain signals acquired with focused and collimated interrogation beams

4.5 Elimination of echo signals using back filtering

After eliminating the side waves, the next step is to eliminate the echo signals caused by the substrate. Section 3.3 has shown that the echoes can be eliminated by back filtering. Thus, the time domain signal in Figure 4.3 (c) is used to validate the back filtering method. Since the real values of the properties of the layers in the miniaturized FP sensor may not be the same as the ones used in simulation, an optimization is conducted using MATLAB first to find the properties of the layers before back filtering. The program loops through the properties of the layers, and for each set of the properties, a back filtering is done on the original data, as shown in Figure *4.4* (a). The back-filtered data is then subtracted from the original data, and the standard deviation of the resultant data is used as the merit function for the optimization. The optimal properties found in this way are: $l = 23.3$ μm, $\rho_2 = 1142$ kg/m^3, $c_2 = 2549$ m/s, $\rho_3 = 3126$ kg/m^3, $c_3 = 5499$ m/s. Then the Fourier transform of the original data is divided by the filter calculated using these optimal properties, and the result is inversely Fourier transformed back to time domain. The back-filtered data is shown in Figure *4.4* (b). The echoes caused by the multi-reflection of the pressure waves inside of the substrate are eliminated. However, periodical artifact signals appear. Although their magnitudes are small, they still cause undesired noises especially at the times where there was no noise.

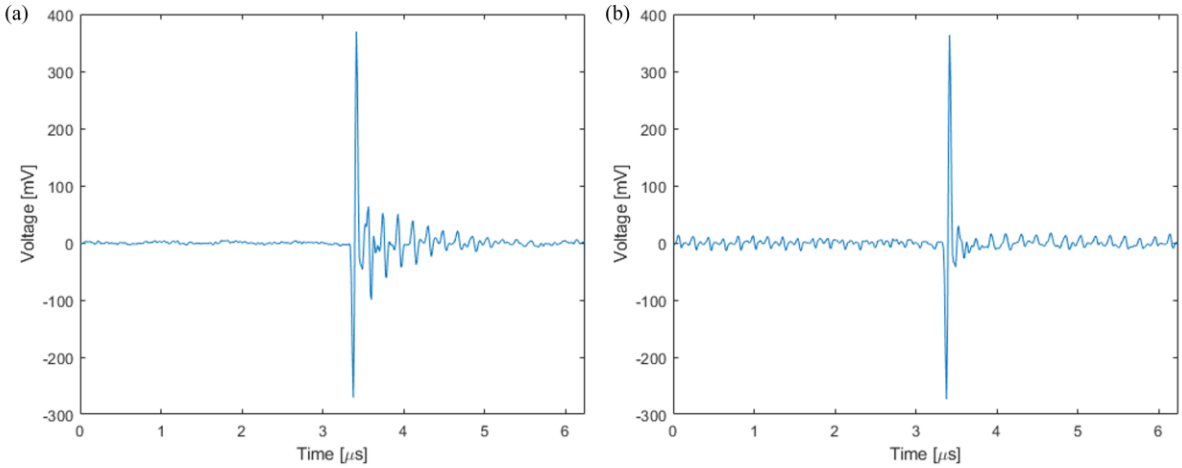

Figure 4.4 Original and the back-filtered signals

These artifact signals should come from the zeros in the spectrum of the original data that were not perfectly canceled by dividing the filter. One possible cause is the finite increment in the frequency axis. It is inversely proportional to the total time window length in the time axis. A finer frequency axis will provide a finer filter, so the zeros can align closer and have better cancellation. To prove this hypothesis, the original data is first appended with zero voltages having the same number of data points, resulting in a new data with twice the length as before. By doing this the frequency axis increment is decreased by half. Then the same optimization is done to find the optimal properties. Finally, the same back filtering operation is done on the new data using the new optimal properties. Figure *4.5* shows the original and the back-filtered appended signals. Compared to Figure *4.4*, it can be seen that the artifact signals are decreased, showing that the finer frequency axis can improve the cancellation. Using more advanced spectrum zero cancellation strategies can further improve the performance of the back filtering. Overall, Section 4.4 and 4.5 show that the side waves and the echoes can both be effectively eliminated, making miniaturized FP sensors promising in building a PAE probe.

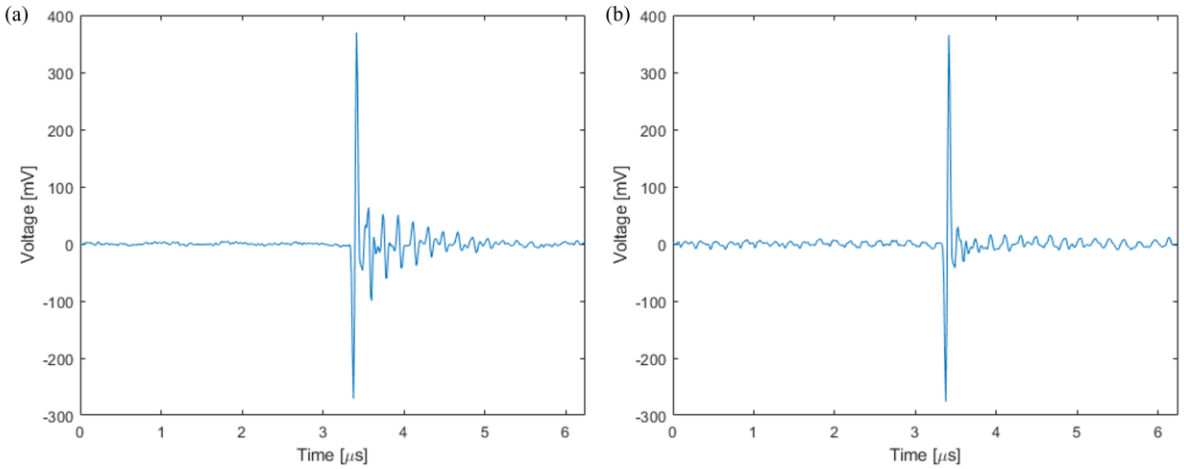

Figure 4.5 Original and the back-filtered appended signals

Chapter 5 Photoacoustic Tomography Based on Miniaturized Fabry-Perot Sensor Array

5.1 Setup of the tabletop imaging system

A tabletop photoacoustic tomography imaging system is built based on the sensor charactering platform as mentioned in Section 3.7. The 9 mm by 2 mm rectangular miniaturized FP sensor is glued into a 3D-printed holder which is mounted onto the side wall of a water tank. Below the sensor is an excitation laser window made by gluing a 22 mm square glass cover slide onto the holder. The ultrasound transducer is replaced by a pulsed laser as the source. The photoacoustic excitation source is an optical parametric oscillator (OPO) tunable laser (Phocus MOBILE, Opotek). It can provide 5 ns pulses over a range of 680 to 950 nm wavelengths with peak energy of 140 mJ and repetition rate of 10 Hz. The output pulses of this laser are focused by a cylindrical lens to achieve line illumination, directed by a mirror M6 under the tank, and go into the tank through the glass window mentioned before, as shown in Figure *5.1*.

The Q-switch output trigger of the pulsed laser is connected to the digital read channel of the data acquisition board and used to trigger the other components of the system. However, the pulse width of this trigger is too short for the data acquisition system to recognize. Thus, a customized circuit consisting of a multivibrator (CD74HC123E, Texas Instruments) is used to synchronize and expand the trigger before sending it to trigger the data acquisition system. Figure *5.2* shows the circuit design to expand the trigger, V_{in} is the Q-switch trigger output form the Opotek laser, V_{out} is the expanded output trigger, and V_{source} is a DC voltage source of 2 V. By using a resistance of 10 kΩ and a capacitance of 0.02 μF, the input pulse with a width of 11.2 μs is expanded to 104.17 μs, which is sufficient to trigger the DAQ system.

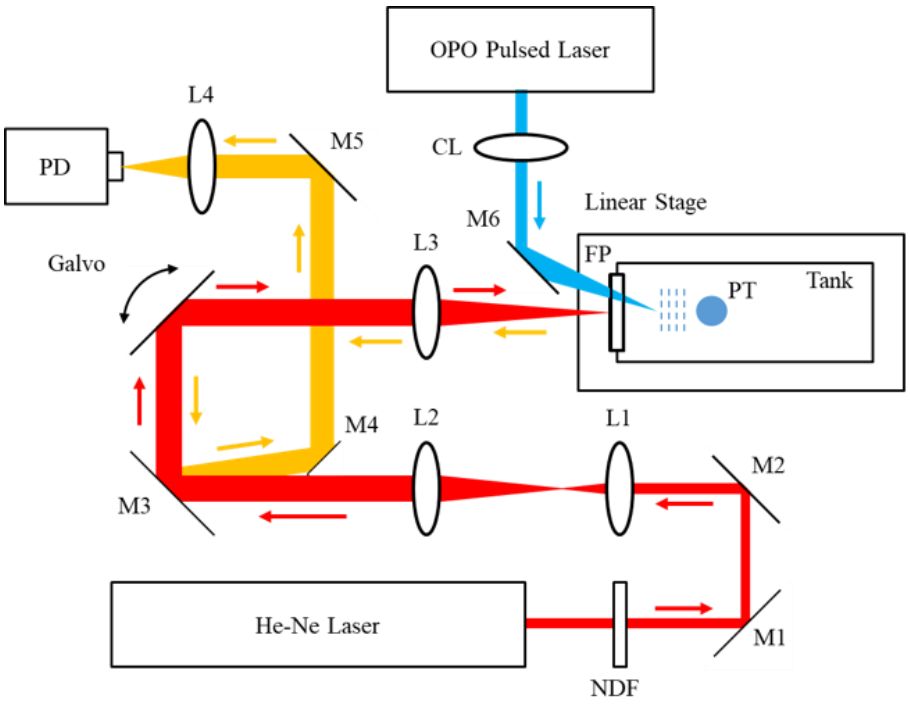

Figure 5.1 Schematic of setup of PAT system

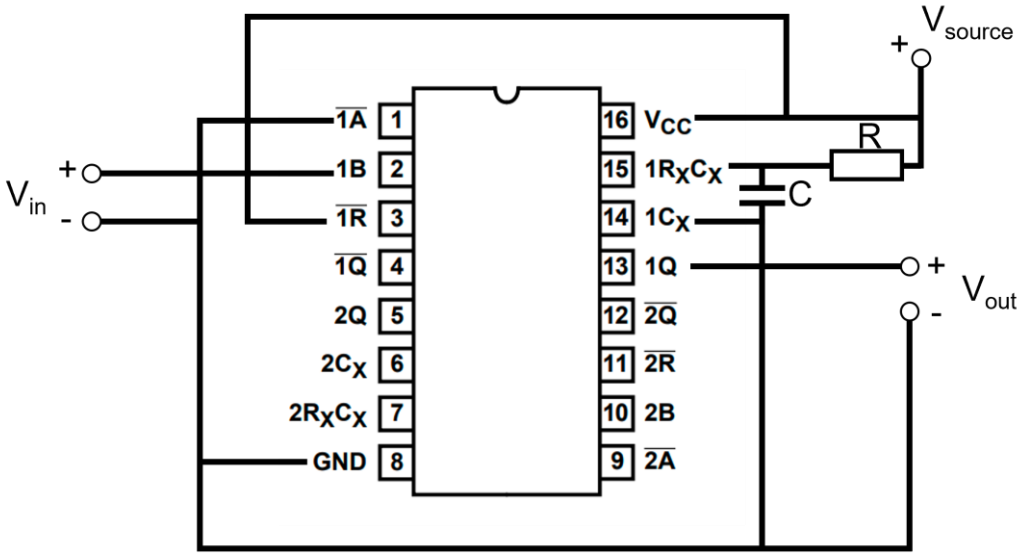

Figure 5.2 Customized multivibrator based circuit to expand the trigger pulse

5.2 Galvo scanning simulation and design parameters

The 75 mm achromatic lens acts as the scan lens such that when galvanometer scans the laser beam, the chief rays of the focused beams coming out of the lens are always perpendicular

to the sensor at the right focal plane of the lens. The focused laser beam onto the sensor can be approximated as collimated beam so that it doesn't spread laterally when undergoing multi-reflection inside of the Fabry-Parot cavity.

Figure *5.3* (a) shows the Zemax simulation of the scanning of the galvo mirror. A ±1.12° scanning angle will result in a ±3 mm line scan, as shown in Figure *5.3* (b). This requires a ±1.12 V input voltage to the galvo mirror. Figure *5.3* (c) shows the focused beams at the center and edges of the sensor. The focus spot at the center has the largest diameter of 121 μm, while the beams on the edges are slightly smaller due to distortion.

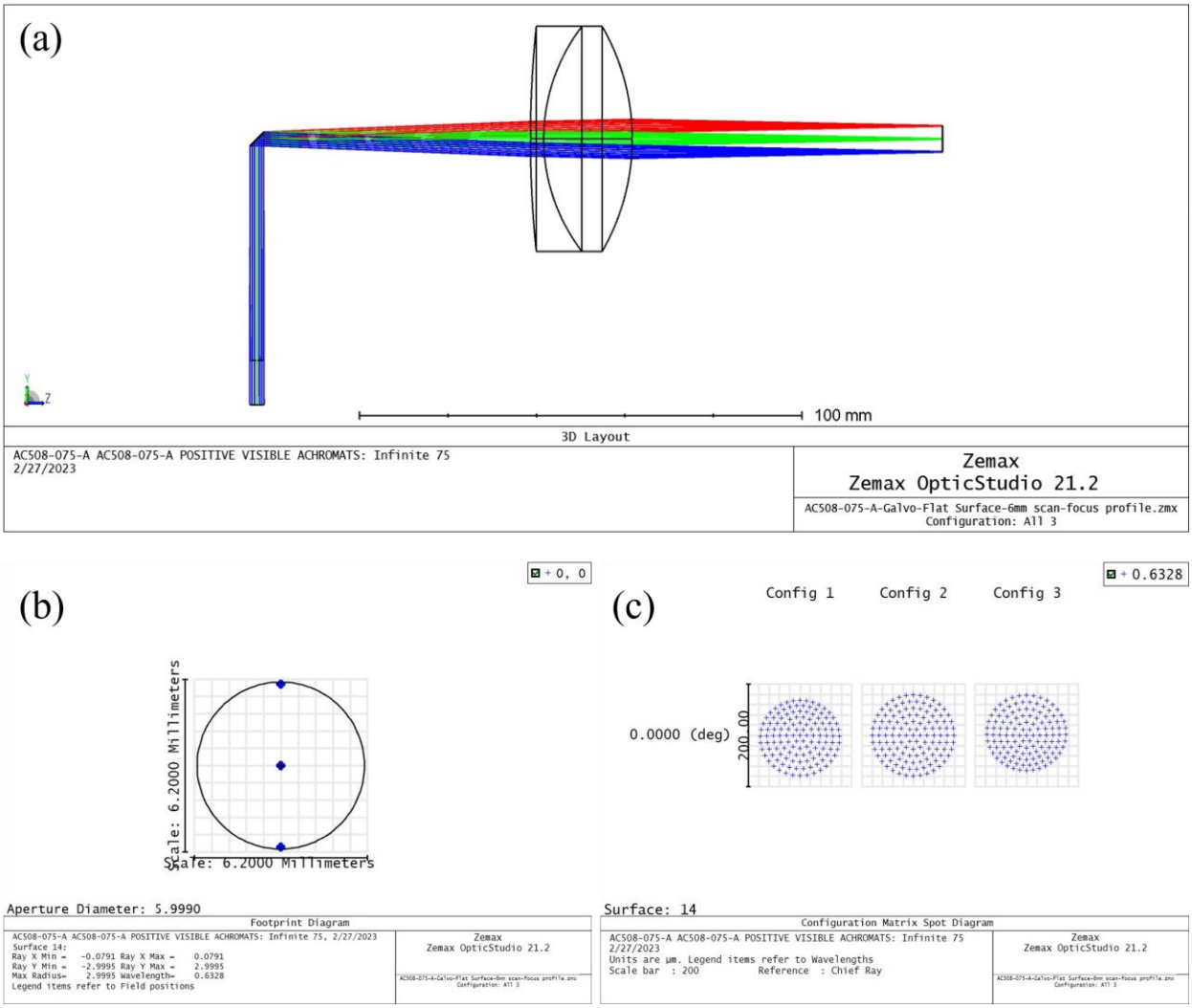

Figure 5.3 Zemax simulation of scanning of galvo mirror

The galvanometer mirror is driven by the output of the NI analog output module. A sawtooth voltage signal is sent to the galvanometer mirror to achieve sawtooth angular scanning. This angular scanning is transformed to a line scanning on the sensor surface by the achromatic lens. The scanning angle is limited by the length of the line scanning on the sensor, which is ultimately limited by the length of relative same sensitivity area on the miniaturized sensor. For a line scanning of 6 mm, the applied amplitude voltage is set to be 1.12 V for the sawtooth signal sent to the galvanometer mirror.

The frequency of the sawtooth signal is determined by the target number of elements on the virtual sensor array and the repetition rate of the pulsed laser. The number of elements is set to be 40 along the 6 mm scanning length, resulting in a 150 μm step size of the virtual sensor array. Given the 10 Hz repetition rate of the pulsed laser, the time for the galvanometer mirror to finish scanning one line is 4 s, or the scanning frequency is 0.25 Hz. This leads to a frame rate of 0.25 Hz, which can be further improved by selecting a pulsed laser with a higher repetition rate.

The output of the Q-switch trigger, sawtooth signal to drive the galvo mirror and the data acquisition are synchronized. The positions of the virtual sensor elements on the 1-D sensor array are estimated according to the time when the laser outputs a pulse, and there is no closed-loop feedback system to measure the actual positions. However, the repetition rate of the pulsed laser is stable enough and no obvious artifacts are observed in later imaging experiments.

5.3 Image reconstruction algorithm

The advantage of sensor array is the ability to form 2-D images using only 1-D scanning with the help of reconstruction algorithm. Here a universal back-projection algorithm is used for reconstruction [7]. In summary, the reconstruction equation to form the back-projected image is:

$$p_0^{(b)}(\vec{r}) = \int_{\Omega_0} b(\vec{r}_0, \bar{t} = |\vec{r} - \vec{r}_0|)\, d\Omega_0/\Omega_0$$

where $\vec{r}$ is the position vector of a point P to be reconstructed, $\vec{r}_0$ is the position vector of a sensor element, Ω_0 is the solid angle of the surface that encloses the target reconstruction area, which is 2π for a planar sensor array, $b(\vec{r}_0, \bar{t}) = 2p(\vec{r}_0, \bar{t}) - 2\bar{t}\partial p(\vec{r}_0, \bar{t})/\partial \bar{t}$ is defined as the back-projection of the pressure at position $\vec{r}_0$, $d\Omega_0 = dS_0/|\vec{r} - \vec{r}_0|^2 \cdot \left[\overrightarrow{n_0^s} \cdot (\vec{r} - \vec{r}_0)/|\vec{r} - \vec{r}_0|\right]$ is the solid angle of a sensor element with area dS_0 with respect to point P at $\vec{r}$, and $\overrightarrow{n_0^s}$ is the normal unit vector of the sensor element dS_0. Figure *5.4* illustrates the relative relationship of these quantities.

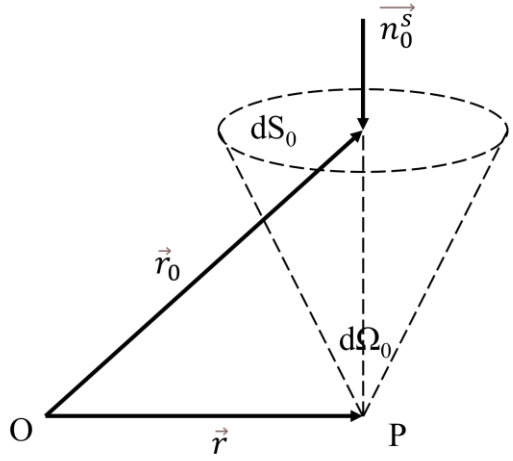

Figure 5.4 Diagram of quantities for image reconstruction

Since photoacoustic signals usually have a wide spectrum, $k|\vec{r} - \vec{r}_0| \gg 1$, then $\bar{t}\partial p(\vec{r}_0, \bar{t})/\partial \bar{t} \gg p(\vec{r}_0, \bar{t})$. Thus, the back-projection term is approximated by $b(\vec{r}_0, \bar{t}) \approx -2\bar{t}\partial p(\vec{r}_0, \bar{t})/\partial \bar{t}$. For a sensor array with discrete locations of detection elements, the above reconstruction equation becomes:

$$p_0^{(b)}(\vec{r}) = \sum_{i=1}^{N} \Delta\Omega_i \cdot b(\vec{r}_i, \bar{t} = |\vec{r} - \vec{r}_i|) \Big/ \sum_{i=1}^{N} \Delta\Omega_i$$

where

$$\Delta\Omega_i = \frac{\Delta S_i}{|\vec{r} - \vec{r}_i|^2} \cdot \left[\frac{\overrightarrow{n_i^s} \cdot (\vec{r} - \vec{r}_i)}{|\vec{r} - \vec{r}_i|} \right]$$

is the individual solid angle of each sensor element with respect to the reconstruction point P. For the 1-D array presented in this dissertation, the reconstruction plane is defined as the (x,y) plane in cartesian coordinate system, so the position vector of a pixel is $\vec{r}$ = (x,y). The 1-D array is placed along the x-axis of the plane, with the sensing elements facing the positive y direction. Thus, the location of each sensing elements is: $\vec{r}_i$ = (x_i,0), and the normal unit vector is simply $\overrightarrow{n_i^s}$ = (0,1). During imaging, a piece of time domain signal is acquired by the FPGA module every time there is an incident laser pulse, and it is then transferred to the host computer and buffered into a FIFO queue. The reconstruction is performed in a parallel while loop where the signal from each sensor element is extracted from the queue and used to update the image matrix. An output image is retuned when all the signals from the array are used.

5.4 Spatial resolutions of the PAT system

To evaluate the resolutions of the sensor, a metal wire with diameter of about 32 μm is used as the imaging target. The wire is placed perpendicularly with respect to the scanning direction of the sensor in order to get a cross-sectional (x-z) image of the wire. A horizontal (x) line scan of 6 mm on the sensor is chosen to form the 1D sensor array. An imaging depth of 9.375 mm is chosen which corresponds to 500 time-domain data points acquired by the 80 MS/s FPGA module. Note that starting depth is not zero because the imaging target has to be placed at a distance from the sensor where the excitation laser beam intersects the imaging plane. Thus, the nominal 9.375 mm depth is actually the difference between the end depth and the staring depth. This configuration is also used in experiments in later sections of this paper. The wire is moved in a raster scanning pattern with a step of 0.1 mm in lateral direction and 0.635 mm (0.025 inch) in

axial direction, and one image is acquired at each location to calculate the corresponding resolutions. The default wavelength of 750 nm of the pulsed laser is used for maximum energy output. Figure *5.5* (a) shows an example of the cross-sectional image of the wire, and (b) shows a zoomed in view of the region near the target wire in (a). Two lines in axial and lateral direction are drawn respectively through the center of the wire in the image, and the normalized profiles of the image intensity are plotted with respect to the relative location, as shown in Figure *5.5* (c) and (d). The profiles are fitted using a Gaussian function and the lateral and axial resolutions are given by the FWHM of the fitting curves. At this example location, the sensor has a lateral resolution of 272 μm and an axial resolution of 32 μm. The lateral and axial resolutions at different locations are calculated using the same method as the wire is raster scanned in the imaging region. The map of lateral resolutions is plotted in Figure *5.5* (e). The dark blue area indicates that the signal is too low to extract resolution data because the wire is too off-centered. It shows that the sensor has a lateral resolution ranging from 208 μm at a depth of 9.375 mm to 519 μm at a depth of 16.36 mm. This decrease arises because the acoustic numerical aperture decreases as the imaging depth increases. Meanwhile, the axial resolution remains relatively invariant across the imaging region, because in theory the axial resolution is predominantly related to the bandwidth of the sensor.

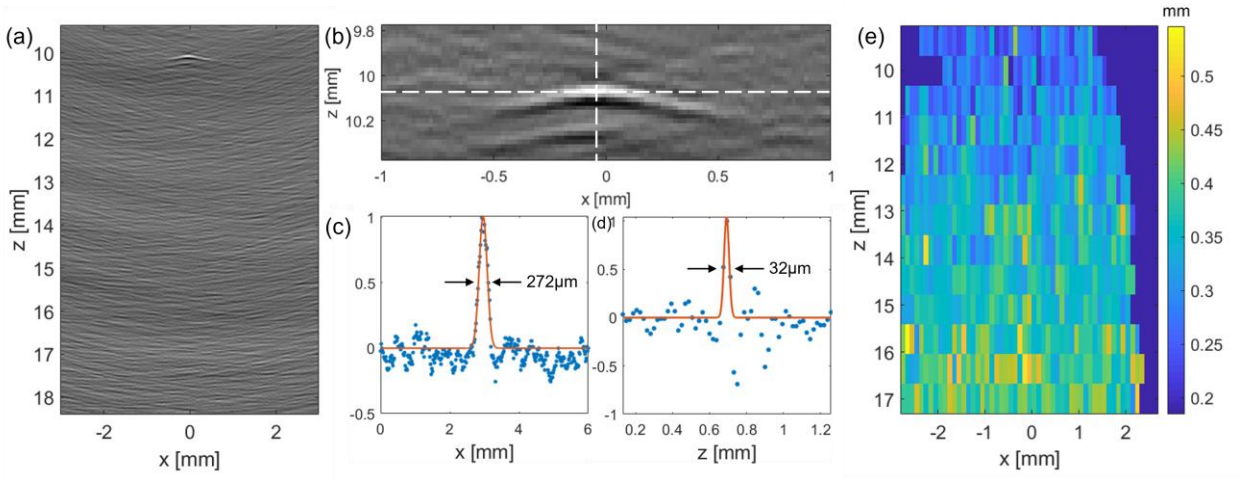

Figure 5.5 Resolution measurements of the PAT system

5.5 3-D imaging of absorbing phantoms

To demonstrate the ability to image objects with different geometries, various imaging phantoms are used to test the performance of the system. One phantom is a soldering wire with a diameter of about 300 μm which is made into a knot. A scanning range of 6 mm and imaging depth of 9.375 mm are chosen as the dimensions of the image. To perform 3-D imaging, the imaging target is pulled along the perpendicular direction (y) of the imaging plane (x-z plane) using a motorized linear stage, and 3D images are formed by stacking. A pulling range of 8 mm and step of 0.05 mm are chosen as the third dimension of the 3-D data set. Figure *5.6* (a) shows a photo of the knotted wire, and (b), (c) and (d) show the maximum intensity projections (MIPs) in x-y, y-z and x-z planes which are reconstructed from the 3-D image data. A comparison between the reconstructed x-y image and the photo shows that the imaging system based on FP sensor can provide an excellent representation of the phantom.

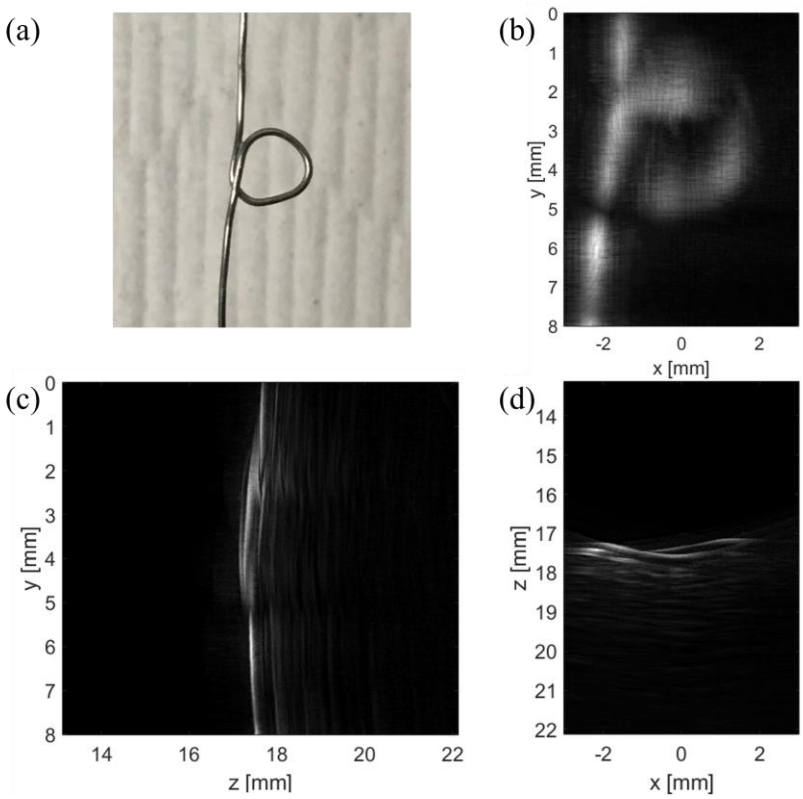

Figure 5.6 3-D images of a phantom made from a knotted wire

5.6 Nanoparticle characterization

Nanoparticles are widely used as exogenous imaging contrast agents to enhance signals at desired locations. Commercial gold nanoshells (GSXR150, NanoComposix) with nominal diameter of 150 nm, 20 OD, and Carboxyl on surface were used for ex vivo imaging of polyp of a CPC-APC mouse colon. The gold nanoshells were characterized before the experiment. They were mounted on glow-discharged formvar/carbon-coated 200-mesh copper grids (FCF200-CU, Electron Microscopy Sciences) before being examined by a transmission electron microscope (TEM, JEM-1400 Plus, JEOL) with an accelerated voltage of 60kV, as shown in Figure *5.7* (a). The sizes of the gold nanoshells (n = 550) were measured from the TEM images using an image processing program (ImageJ, National Institutes of Health), and the size distribution result was plotted in Figure *5.7* (b). The absorption spectrum was measured in the wavelength range of 400-

1000 nm with an increment of 1 nm using a modular multimode microplate reader (Synergy H1, BioTek). The average size of the nanoshells is 165.41 nm with a stand deviation of 11.56 nm, and the peak absorption occurs at 804 nm, which are not far from the spec sheet.

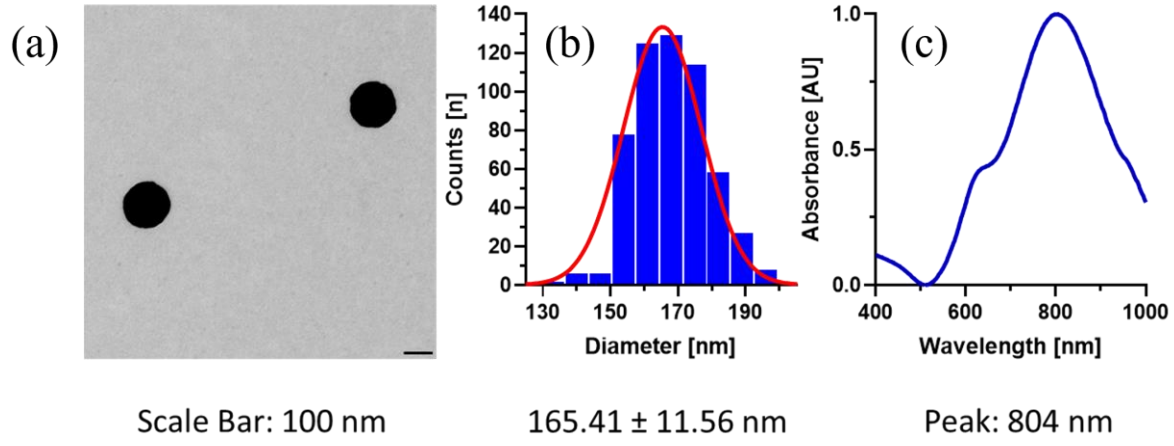

Figure 5.7 Characterization of gold nanoshell

5.7 Ex vivo 3D imaging of mouse colon tissue

CPC-APC mice are genetically engineered mice which can spontaneously form adenomas in the distal colon [79]. They provide a convenient model to study colon cancer in early stages. The mouse was anesthetized before IV injection of 200 µL gold nanoshell solution. The colon tissue is harvested 2.5 hours after the injection. The colon tissue is glued to a microscope slide with UV-glue (NOA 61, Norland Products Inc.) for better support and more convenient handling, as shown in Figure *5.8* (a). The excitation wavelength is set to 804 nm corresponding to the peak absorption of the gold nanoparticle and the pulse energy at the imaging region is estimated to be 15 mJ/cm2, which is below the maximum permissible exposure (MPE) for skin [80].

There are two relatively large polyps at the end of the colon tissue, which are indicated by red dashed rectangles in Figure *5.8* (a). Due to the limited lateral scanning range, these two polyps are imaged separately. The same line scan of 6 mm and depth of 9.375 mm are used, and the glass

slide is pulled by a motorized stage with a range of 12 mm due to the elongated shape of the polyps. Figure *5.8* (b) through (d) are the MIPs of the left polyp in x-y, y-z and x-z planes reconstructed from 3D photoacoustic data, while Figure *5.8* (e) through (g) are the corresponding images of the right polyp. With the help of gold nanoparticles, the polyps are distinguished from the surrounding normal tissues.

Note that the images in x-z plane and y-z plane are highly symmetric along the depth (z) direction. This is caused by the reflected echo acoustic waves from the surface of the glass slide. Thus, the image patterns at a larger depth in these images are the mirror-image of the signals from a smaller depth. Despite the echo artifacts, the sensor is still able to image the polyps up to a depth of about 4 mm, as shown in Figure *5.8* (b) and (c).

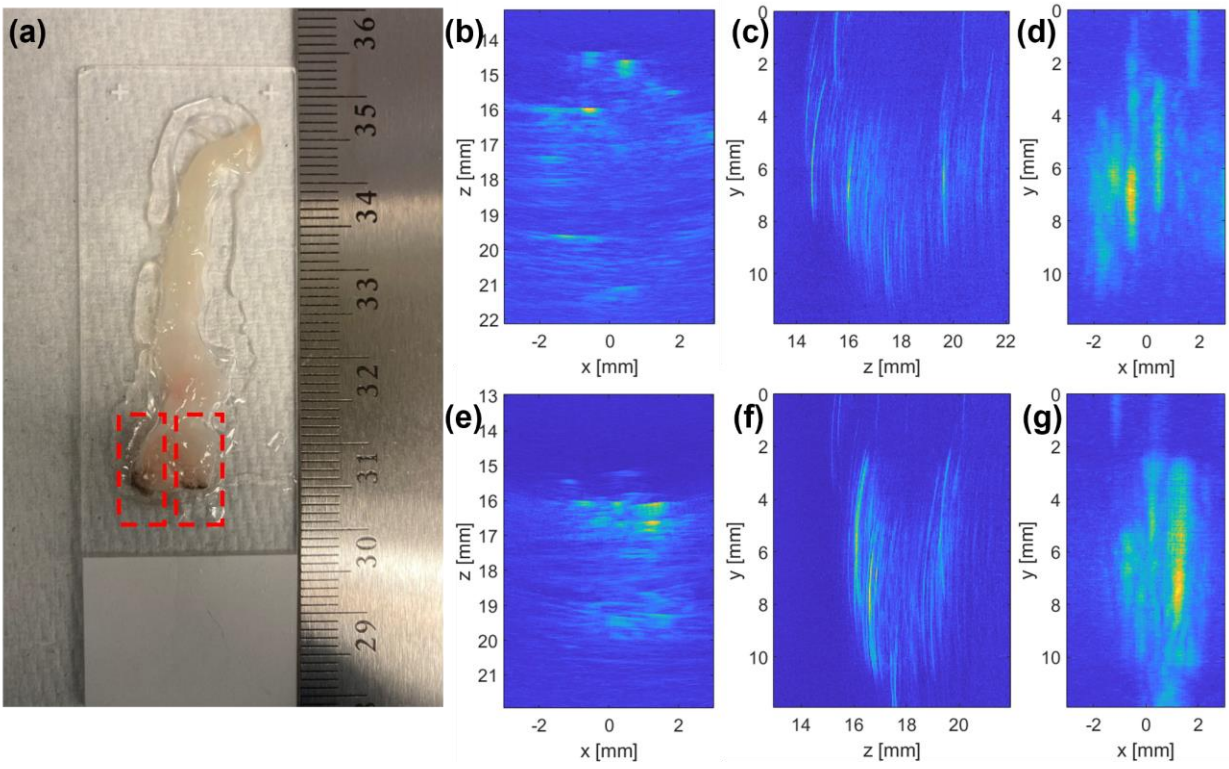

Figure 5.8 Ex vivo imaging of colon polyps of a CPC-APC mouse

Chapter 6 Photoacoustic Endoscopy Based on Miniaturized Fabry-Perot Single Element Sensor

A miniaturized FP polymer film ultrasound sensor array has been demonstrated for PAE applications. A tabletop system is built to conduct ex vivo imaging of colon polyps of a CPC-APC mouse. The next step is to implement this technology into a miniaturized imaging probe to conduct in vivo imaging. However, as has been shown in the last chapter, the array needs to be line scanned by a focused laser to perform tomography imaging. The need for a line scanner with a scanning range of several millimeters causes difficulties in building a PAE probe. New strategies are needed to solve this problem This chapter demonstrates a PAE design based on a 2 mm by 2 mm miniaturized single element FP sensor as an attempt to overcome this challenge.

6.1 Design of PAE probe based on single element FP sensor

A miniaturized imaging probe is necessary for in-vivo mouse imaging. The dimension of the single-element Fabry-Perot sensor is constrained by the packaging design of the imaging probe. Here, a preliminary PAE probe design is proposed, as shown in Figure *6.1*. The outer diameter of the probe is set to be 3.95 mm, which is limited by the diameter of the mouse colon. The probe has a 3-D printed sheath with an imaging window on the side to form a side-viewing configuration. Based on the geometry of the probe and the side-viewing configuration, the lateral size of the single element Fabry-Perot sensor is set to be 2mm by 2mm. The total thickness, including the glass substrate and the coatings, is estimated to be 0.54 mm, as shown in Figure *6.1* (a). Panel (b) shows the inner structure of the probe. There are two sub-probes for delivering the excitation laser beam and the interrogation laser beam. Each sub-probe consists of a light delivery optical fiber, a

fiber ferrule to fix the fiber, a GRIN lens to focus or collimate the light coming out of the fiber, and a stainless-steel tube to hold the components. The diameter of the stainless-steel tube is 1.27 mm, while the diameters of the glass ferrule and the GRIN lens are both 1 mm. The details of these optical and mechanical components will be discussed in the Section 6.2. The laser beams coming from both two sub-probes are reflected by a 2.5 mm prism (MPU-2.5, Tower Optical Corporation) mounted at the tip of the sheath.

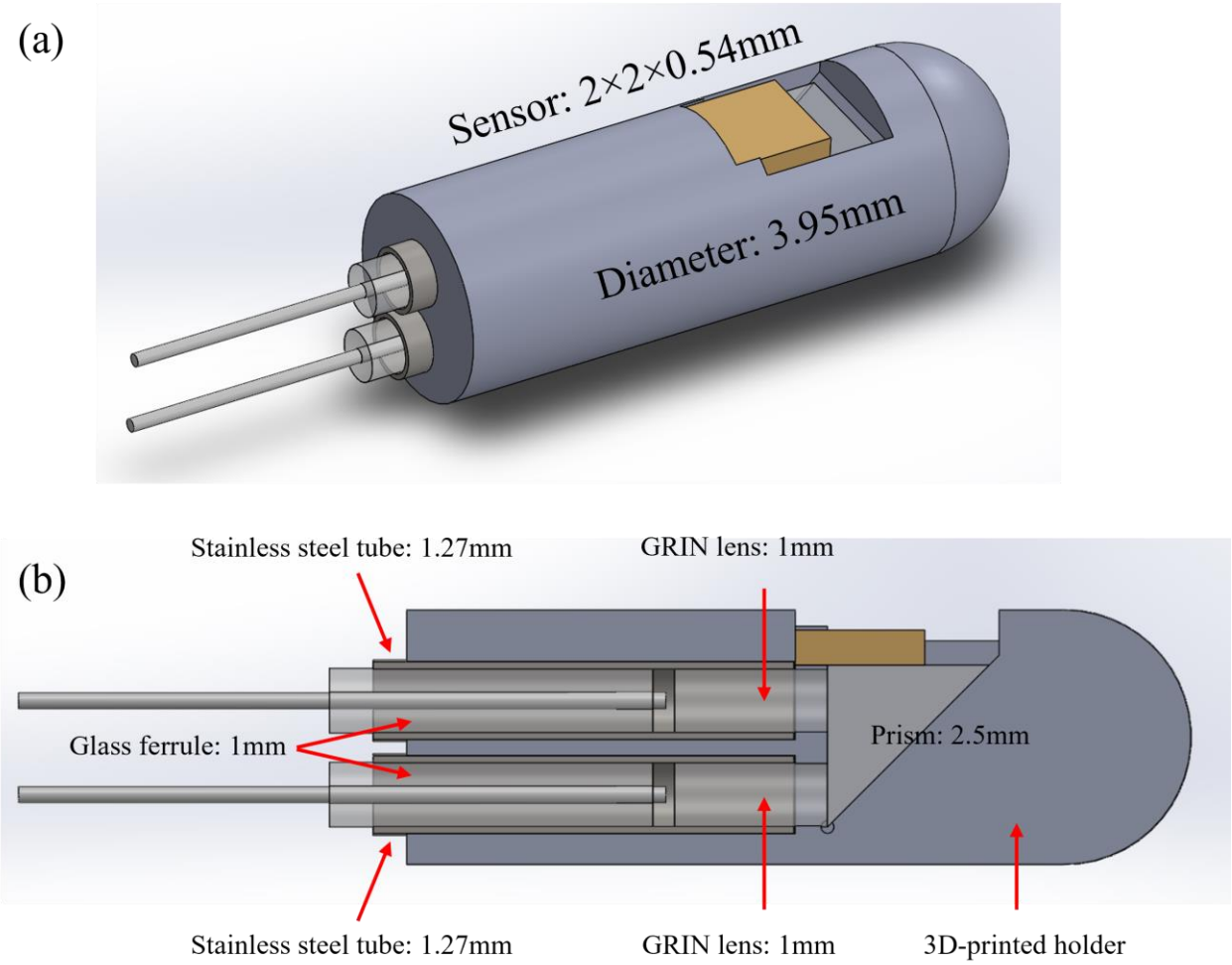

Figure 6.1 Design of the PAE imaging probe based on 2 mm FP sensor

Figure *6.2* shows the optical design of the imaging probe. The interrogation laser is collimated by the lower sub-probe and is incident onto the back of the Fabry-Perot sensor. The collimated beam is reflected by the sensor and goes back into the same fiber after being picked up

by the GRIN lens. The excitation laser is focused by the upper sub-probe and transmits through the end surface of the prism after being internally reflected. Due to the opaque nature of the gold-coated Fabry-Perot sensor, the sensor is placed off-centered on top of the prism, with 0.5 mm protruding from the edge of the prism. This creates a 1 mm window on the other side of the prism that allows the excitation laser to pass through. The excitation laser beam is at an angle with respect to the normal of the end surface of the prism such that the photoacoustic signal can be picked up by the sensor. Panel (b) shows the Zemax simulation of the paths of the detection and excitation laser beams. Note that the GRIN lens has a pitch, meaning that the fiber is at a distance from the GRIN lens when the light is collimated. To focus the light the fiber needs to be placed even further. Panel (b) shows that the excitation and detection fibers are 0.135 mm and 0.2792 mm away from the GRIN lens, respectively. The dimeter of the collimated detection laser is 0.386 mm. To achieve a tilted beam, the fiber tip is de-centered from the GRIN lens for 0.135 mm. The focus of the excitation laser is designed to have a 3 mm working distance, with a lateral distance of 0.707 mm from the center of the sensor. This distance is optimized based on the maximum receiving efficiency of the sensor.

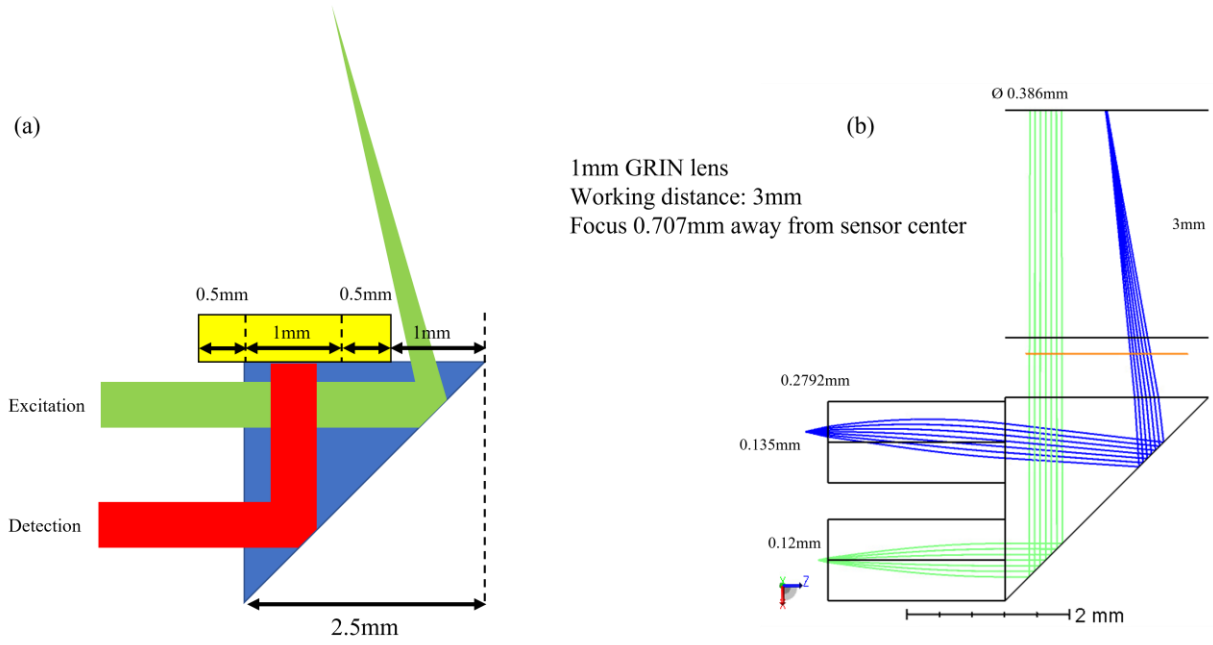

Figure 6.2 Optical paths of interrogation and excitation lasers inside of the PAE probe

6.2 Fabrication of 2 mm miniaturized Fabry-Perot sensor

To verify the feasibility of dicing the glass wafer-based Fabry-Perot sensor into smaller pieces below 2 mm, a new batch of sensors are fabricated using the same recipe as mentioned in Section 3.6. This time after the depositions, the whole wafer is first diced into two halves. Then the upper half is further diced into 2 mm by 1 mm rectangles, and the lower half is diced into 2 mm by 2 mm squares. These halves are partially diced to form trenches, with a remaining glass wafer of thickness of 200 um. Then the half wafer is broken into 10 mm by 10 mm square pieces by hand along the trench so that they can be tested using the same setup as Section 3.7. Panel (d) and (e) show two representative photos of the broken pieces with 2 mm by 1 mm and 2 mm by 2 mm sensors on them. Note that in panel (b) many of the coatings peel off after the 2 mm by 1 mm dicing, while most of the coatings remain after the 2 mm by 2 mm dicing. This implies that the coatings are more vulnerable to the dicing process when the dicing step is too small.

Figure *6.4* shows the surface sensitivities of selected 10 mm square pieces. The figures are placed according to their relative positions on the original wafer. From our previous knowledge about the wafer-based sensors, there should be concentric fringe patterns on the wafer, and dicing would not affect the shape and continuity of the pattern. However, when the dicing step comes down to 2 mm and smaller, the coatings become vulnerable to the dicing and the edge of the film is warped, which can be seen from the white periphery of each miniaturized sensor. When the dimension of the sensor is large compared to the trench, such as 2 mm, this warping effect is not severe and the center region of the sensor can still have a relatively uniform and high sensitivity. When the dimension of the sensor is even smaller, the warping effect will become dominant, significantly reducing the usable region in the center of the sensor, or even leaving the sensor completely unusable. This is the reason why no continuously concentric fringes are observed in the upper half of the wafer. Thus, the lateral size of the miniaturized sensor is limited to 2 mm. The 2 mm sensor with uniform high sensitivity region is further broken from the 10 mm square by hand, cleaned by acetone and IPA, coated with 4 um Parylene C as protective layer, and glued to a 3-D printed holder to be waterproof.

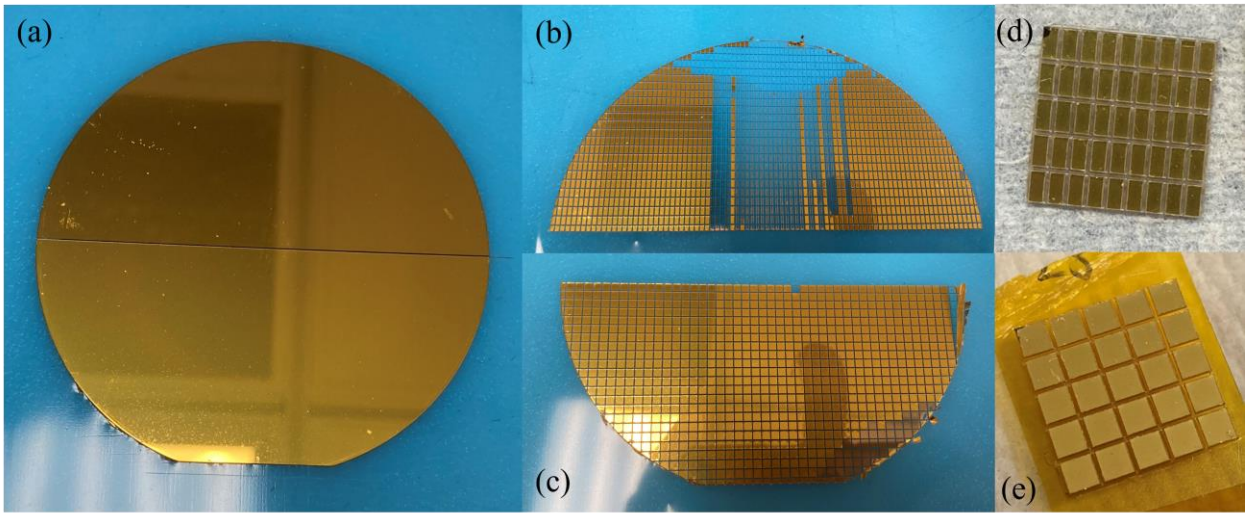

Figure 6.3 Fabrication results of 2 mm by 2 mm and 1 mm by 2 mm sensors

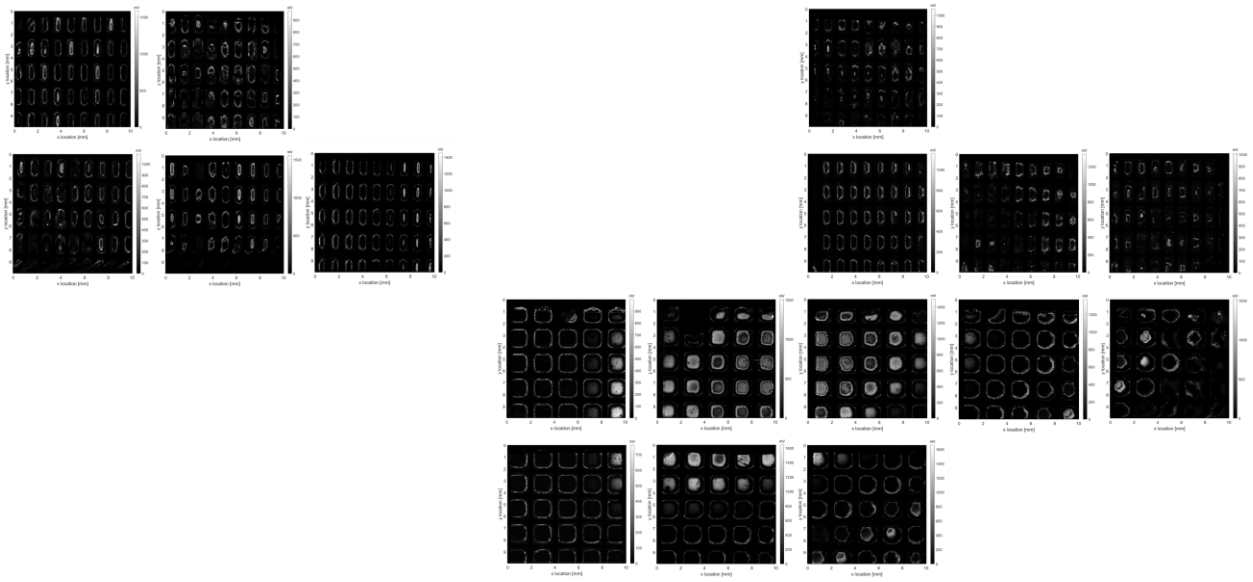

Figure 6.4 Surface sensitivities of selected sensors

6.3 Zemax simulation and measurements of beam profile

For the first generation of PAE probe, it will use hemoglobin as the imaging contrast agent, so the wavelength is 532 nm. Thus a INNOSLAB Nd:VO4 Laser (BX60-2-G, EdgeWave) is selected as the excitation light source, and a GRIN lens with customized anti-reflection coating (GT-LFRL-100-025-50-C1, Grintech) is used to avoid damage. To deliver as much pulse energy as possible without damage, a 105 um core MMF (FG105LVA, Thorlabs) is chosen to deliver the excitation laser. Since the core is large compared to a single-mode fiber, the previous Zemax simulation needs to be modified to consider the propagation of multi-mode optical waves.

To accurately model the propagation of light in a MMF, non-sequential simulation in Zemax is used. The MMF is modeled as two concentric cylinders with different indices of refraction. The optical properties of the core and cladding and the input NA are from the spec sheet of the selected MMF. Figure *6.5* shows the Zemax simulation of the propagation of the beam after the GRIN lens. It can be seen that because of the higher modes of optical wave inside of the MMF, there is no well-defined focus after the beam exits the GRIN lens. Thus, optimization on the

distance between the MMF and the GRIN lens is performed to get the minimum beam diameter when the image plane is 5.5 mm away from the GRIN lens, corresponding to a 3 mm imaging depth in the probe design mentioned in Section 6.1. The simulation reveals an optimal distance of 0.1579 mm between the MMF and the GRIN lens to give a 664.29 μm (estimated by twice of the GEO radius) diameter beam spot at the imaging plane.

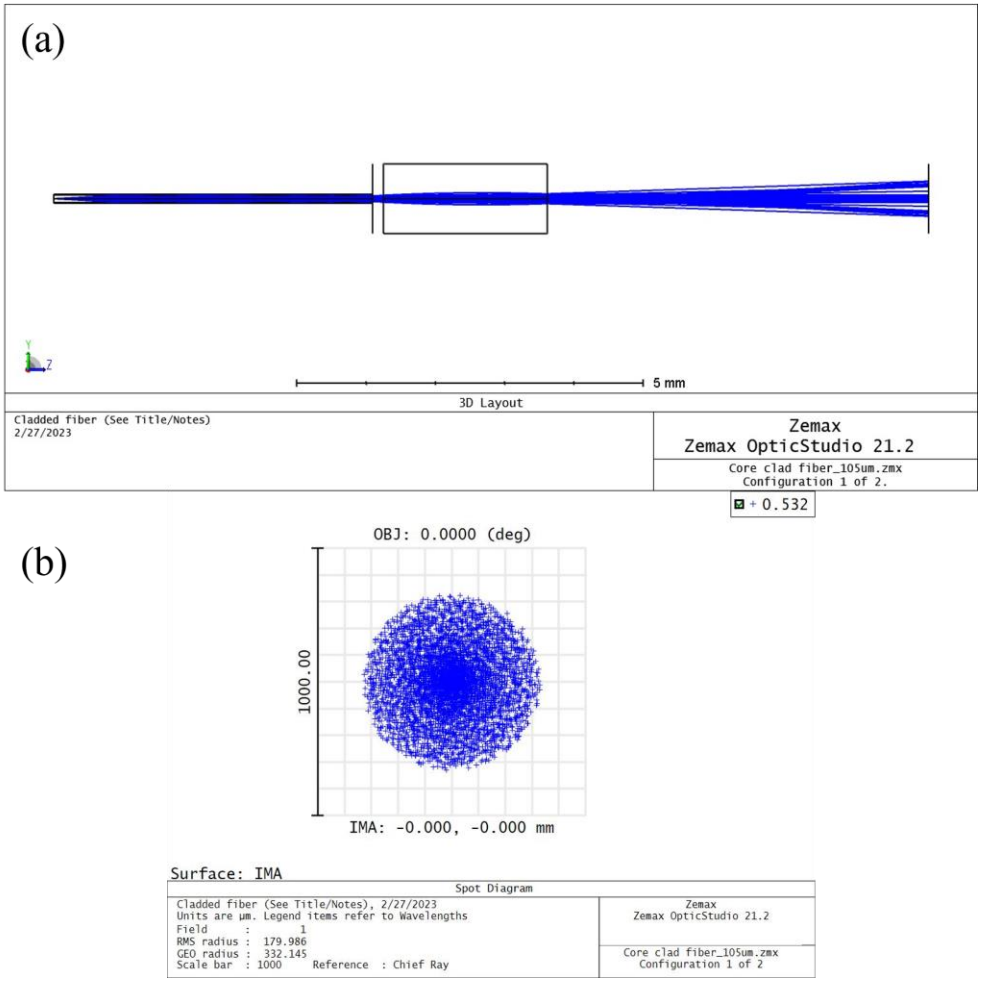

Figure 6.5 Zemax simulation of 532 nm laser beam propagating through a GRIN lens

6.4 Coupling of the 532 nm excitation laser and beam spot measurements in free space

Before the assembly of the sub-probe, the excitation laser is coupled into the MMF. Figure *6.6* shows the setup to couple the 532nm excitation laser. The output beam is guided by a pair of mirrors M1 (PF10-03-P01, Thorlabs) and M2 (E02, Thorlabs) to an objective lens (M-5X,

Newport). The end of the MMF is held by a fiber chuck (FPH-J, Newport). Both the objective lens and the fiber chuck are mounted on a 3-axis stage fiber launch system (MBT613D, Thorlabs).

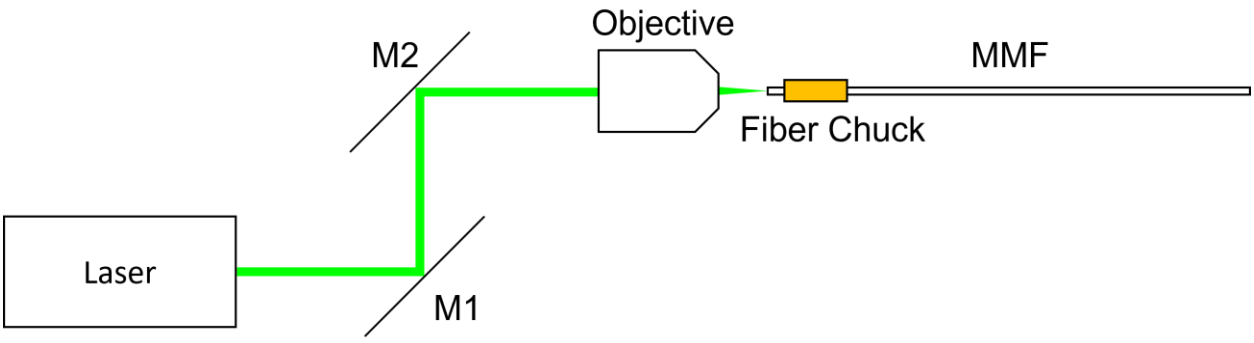

Figure 6.6 Coupling of 532nm laser

After the coupling, the end of the MMF is placed in front of the GRIN lens and controlled by a manual stage. A beam profiler (BP209-VIS, Thorlabs) is placed after the GRIN lens to measure the beam diameter. It is first put at 5.5 mm away from the GRIN lens to represent the target imaging depth as described in Section 6.1. The MMF is moved by the manual stage until the measured beam diameter on the beam profiler is minimum. Then the MMF is fixed, and the beam profiler is used to measure the beam diameters at different distances from the GRIN lens. Note that there is an imaging window that covers the internal sensor of the beam profiler, and the closest distance to the sensor of the beam profiler is estimated to be 1.61 mm by measuring the output of a single-mode fiber. The measured beam diameters are plotted with the simulation results from the model described in Section 6.3. The experiment data matches the simulation very well, demonstrating the ability of the Zemax model for MMF-GRIN lens beam propagation.

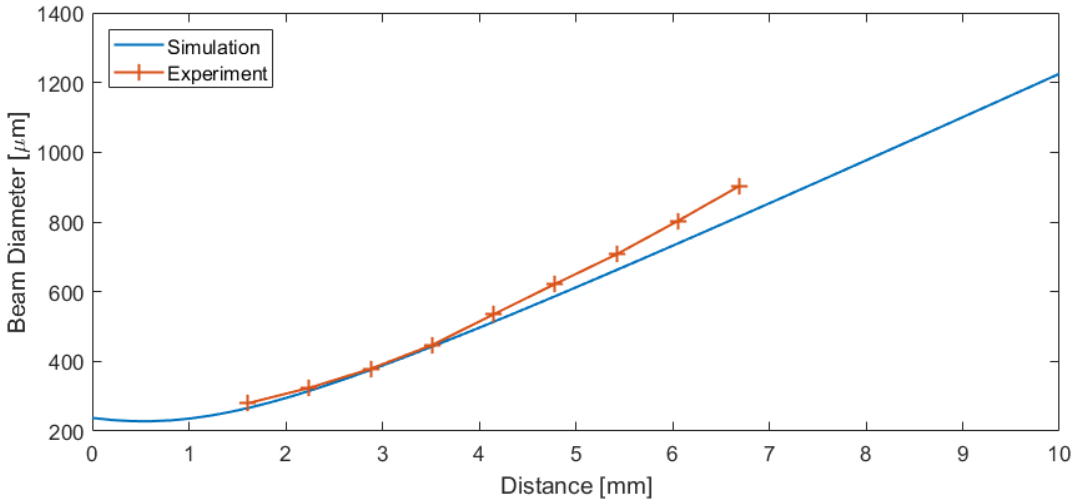

Figure 6.7 Simulation and experiment results of beam profile

6.5 Fabrication of excitation sub-probe using 105 μm core MMF

After the laser is coupled into the MMF, the next step is the fabrication of the excitation sub-probe. Since the cladding diameter is only 125 μm, there will be light leaking through the thin cladding if the coating is removed and fiber is glued to a common 125 μm ID fiber ferrule. Thus, a special glass ferrule (9235, VitroCom) is selected with an OD of 1.00 mm, an ID of 0.27 mm and length of 5 mm. The coating of the MMF is first removed by a single fiber stripper (SS03, Fujikura) and cleaned by fiber optic splice and connector cleaner (Sticklers, MicroCare). The peeled MMF is then insert through the ferrule, leaving enough length of exposed cladding for later processes. Next the exposed cladding is cut by a fiber cleaver (CT50, Fujikura). After examining the cut with a fusion splicer (90S, Fujikura), the MMF is pulled back from the uncut side until the remaining exposed cladding is just sticking out of the ferrule. The fiber outside of the ferrule also contains some length of coating to isolate the exposed cladding from the glass ferrule to avoid light leakage. Finally, the MMF is glued at the other end of the ferrule with UV glue (NOA 61, Norland Products Inc.).

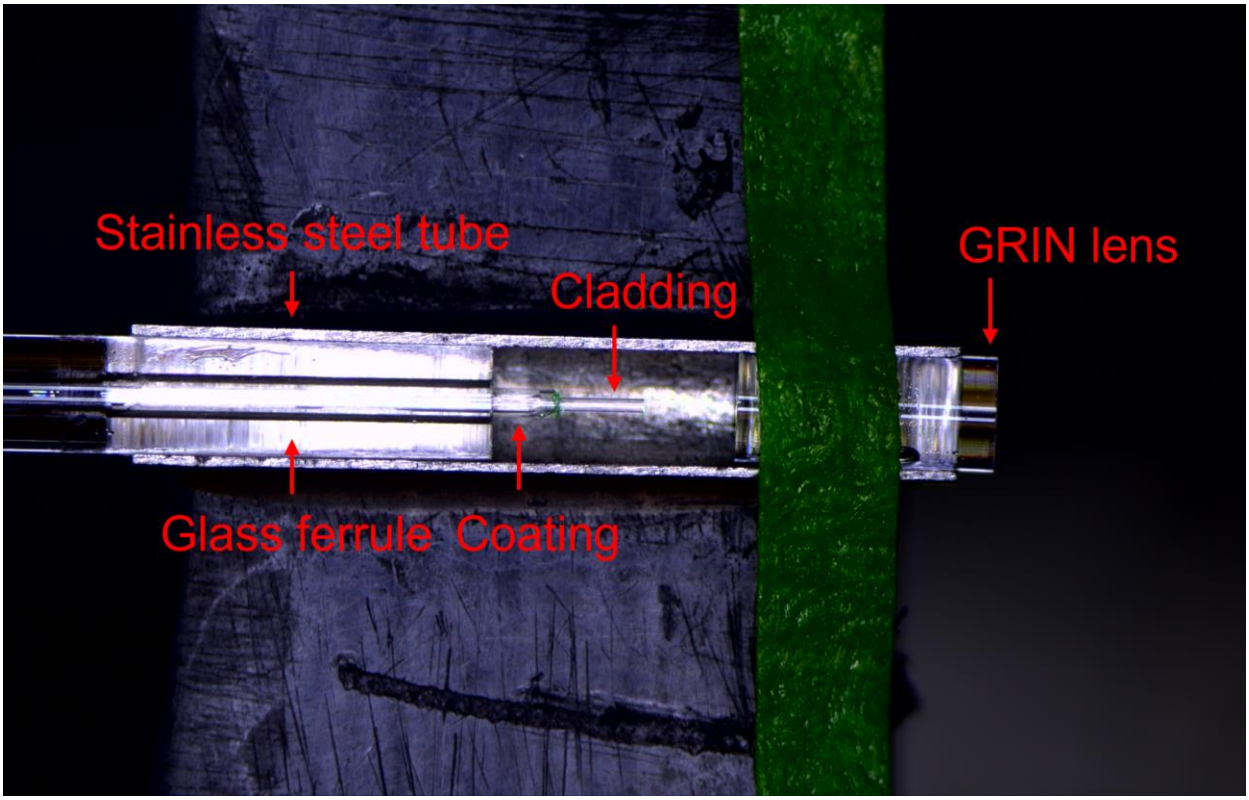

Figure 6.8 Photo of the excitation sub-probe assembly

The chosen stainless-steel tube (5560K46, McMaster) has an OD of 1.27mm (0.05 in) and a wall thickness of 0.1016 mm (0.004 in), thus having an ID of 1.0668 mm (0.042 in). To better monitor the positions of the components during assembly, the upper part of the tube is removed by a custom-made abrasive machining tool. During assembly, the GRIN lens is firstly put into the tube manually and fixed by NOA 61 UV glue on the side. The glass ferrule is mounted on a manual stage and is carefully positioned under the monitoring of two microscopes, one from the top view and one from the side view. The ferrule is placed into the metal tube by the manual stage and the distance between the fiber tip and the GRIN lens is determined by the output diameter of the beam at the target 5.5 mm imaging depth. The beam diameter is measured by a beam profiler (BP209-VIS, Thorlabs) placed 5.5 mm away from the GRIN lens. To prevent the optics from being burnt by the high fluence of the excitation laser, the output diameter is intentionally set to 1 mm instead

of the previously designed 664.29 μm to leave more space between the fiber tip and the GRIN lens such that the beam diameter at the surface of the GRIN lens is larger. The distance is about 0.8 mm, as measured by counting the pixels of the photo taken by the microscope. The energy output from the sub-probe is 149 μJ when the control current is 50 A, while the energy measured right after the laser is 191 μJ, leading to an overall coupling efficiency of 78%.

6.6 Tabletop photoacoustic imaging system based on sub-probe

A new tabletop imaging system is built to incorporate the excitation sub-probe, as shown in Figure *6.9*. Polarizing optics are used to sufficiently use the power output of the He-Ne laser. A polarizer is used to polarize the output of the He-Ne laser. A polarizing beam splitter (PBS) is placed right after the polarizer and a quarter wave plate (QWP) is used to transfer the linearly polarized beam to circularly polarized beam. The laser beam is directed by a fixed mirror which is mounted on a kinematic mirror mount (KM100, Thorlabs) and is incident downward onto the glass substrate of the miniaturized FP sensor. The sensor is mounted on the same 3-D printed holder described in Section 3.7. which is controlled by a manual stage to align the center of the sensor with the laser beam and adjust to the proper height. The reflected beam from the sensor is transferred back to a linearly polarized beam which is perpendicular to the original beam by the same QWP and is directed by the PBS onto the same photodetector (PD) used before.

The imaging target is held by a home-made plastic container, as shown in Figure *6.9*. First, the imaging target is placed on top of a block-shape holder which is placed on the bottom of the container. The height of the block-shape holder is designed such that the height of the imaging target is the same as the wall of the container. US imaging gel (EcoVue) is applied to the target for acoustic coupling. The target is held down by a plastic tank which is placed on top of the bottom container. The tank has a square-shape hole on its bottom and a plastic membrane is sealed on the

hole as an imaging window. The top tank is filled with water, and the water, the membrane and the US gel are in good contact during imaging. The whole assembly is placed on a 2-D motorized stage. The excitation sub-probe is mounted on another manual stage. The excitation laser coming out of the sub-probe illuminates the target through the membrane at an angle. The sub-probe is positioned in the manner as described in Section 6.1. such that the focus is about 5.5 mm away from the FP sensor. During imaging, the whole assembly is raster scanned in 2D, and the depth profile is acquired by taking Hilbert transform of the signal.

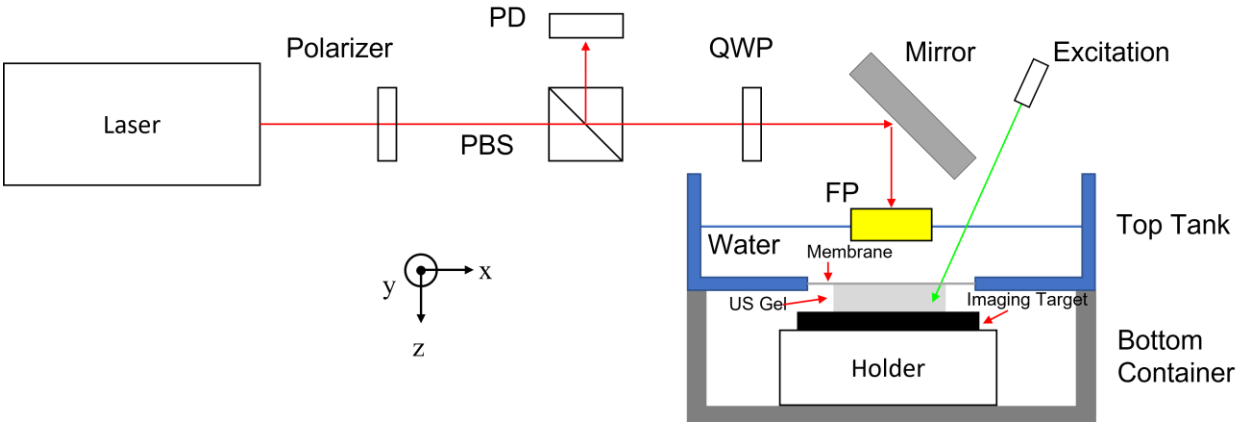

Figure 6.9 Schematic of setup of the tabletop system based on sub-probe for excitation

6.7 Fabry-Perot single element sensor phantom imaging

A home-made phantom is used to verify the performance of the imaging system, as shown in Figure *6.10* (a). The phantom consists of three sets of line-shape phantoms. The first phantom set consists of three 300 µm diameter pencil leads. They are arranged in a triangular configuration with 2.5 mm separation. The second phantom consists of the same type of three pencil leads, but they are evenly placed in a horizontal plane with a separation of 1 mm. The third phantom consists of three 63 µm diameter magnet wires (42 AWG), also placed in a horizontal plane with a separation of 1 mm. They are embedded in PDMS to mimic tissue. The configurations are shown in Figure *6.10*. (b).

The maximum intensity projection (MIP) images of the second phantom are shown in Figure *6.10* (c), (d) and (e). The control current of the 532 nm pulsed laser is 40 A, resulting in an energy output of about 79 μJ. Higher current was not used because the optics, especially the GRIN lens, could be burnt at higher energy outputs after running for a long time. The repetition rate of the laser is set to 10 Hz to be compared with the output of Opotek laser and to avoid burning damage on the optics. The scanning field of view is 4 mm by 4 mm, with a scanning step of 0.05 mm. 500 time-domain data points are recorded at each pixel, resulting in an imaging depth of about 9.375 mm. The raw A-line data is processed with a Hilbert transform to extract the envelope of the depth data, and all the A-lines arranged pixel by pixel form the 3-D matrix for image visualization. The total image acquisition time is about 30 min. It can be seen that the structures of the three pencil leads are clearly shown. Note that the one pencil lead on the right is slightly higher than the other two. This is attributed to the error during fabrication of the phantom.

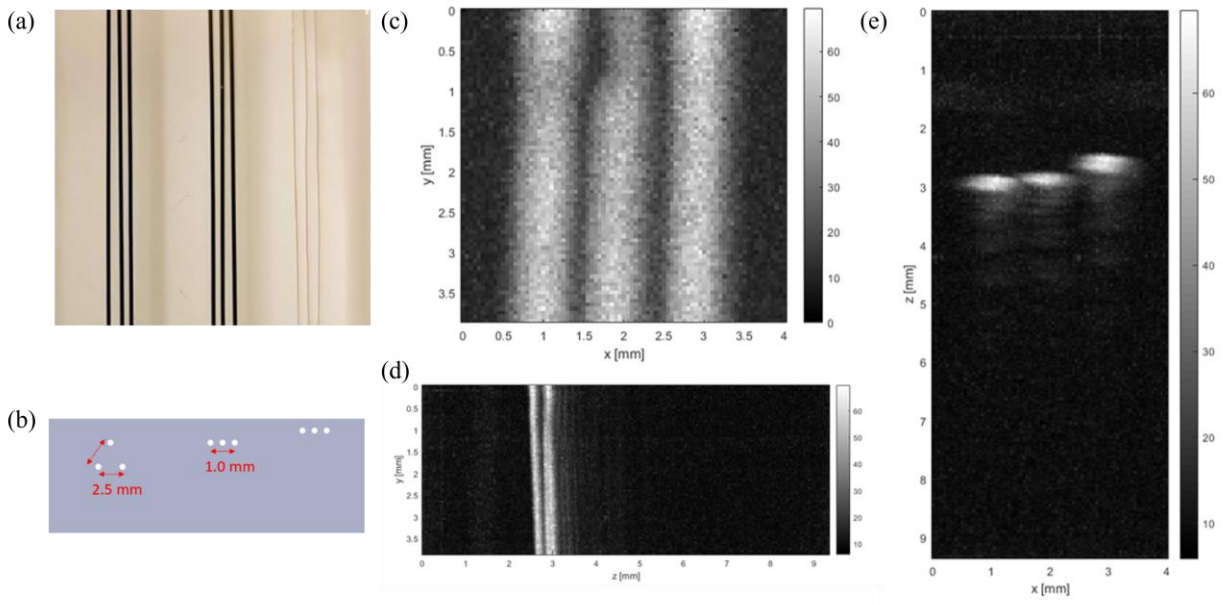

Figure 6.10 Photo and MIP images of pencil leads phantoms

Figure *6.11* shows the MIP images of the first triangular phantom set. It can be seen that the triangular configuration is clearly imaged. However, the signals of the lower two pencil leads

are weaker than the top one. This is because of the divergence of the excitation laser beam at larger depth. Thus, the best imaging quality is achieved when the imaging target is close to the FP sensor and excitation laser probe.

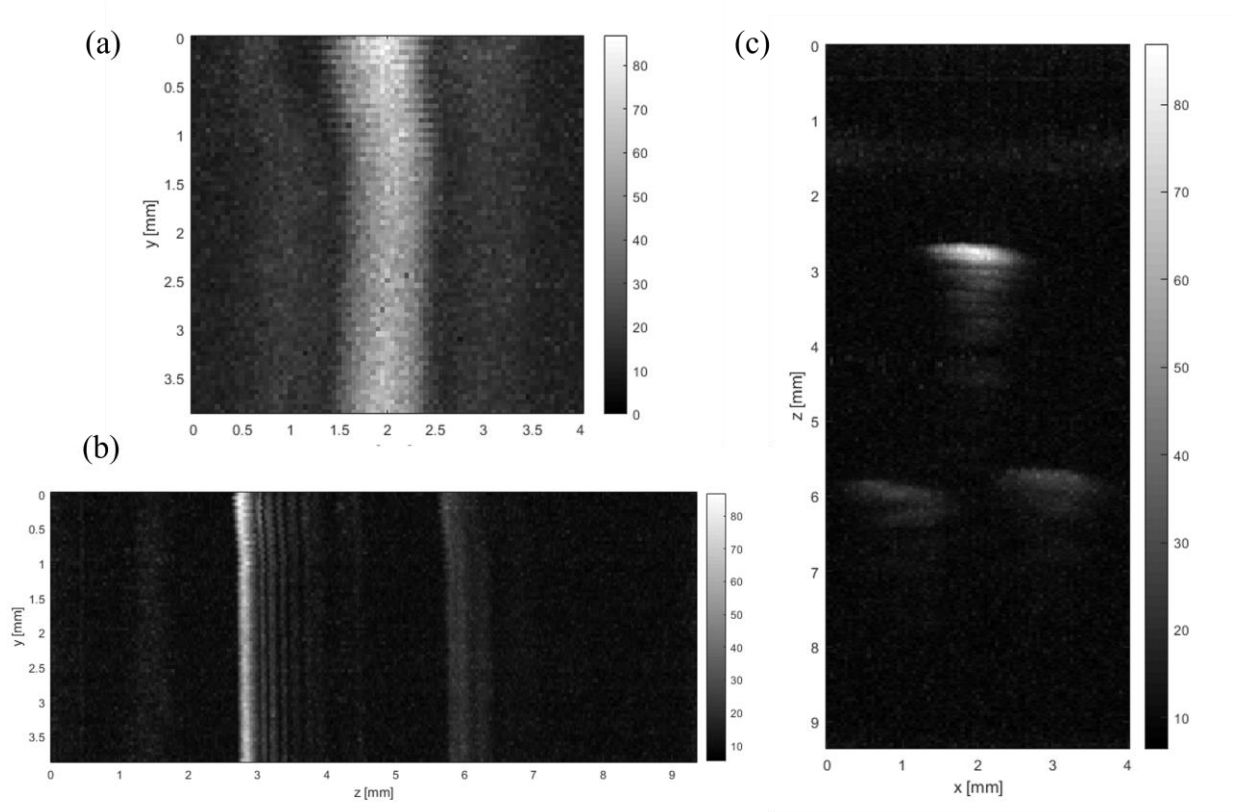

Figure 6.11 MIP images of pencil lead phantoms in a triangular configuration

However, the third phantom of 63 μm diameter magnet wires could not be imaged. This may attribute to the lower absorption than the pencil lead. To increase the signal level, the fluence at the target location needs to be increased. Since the energy delivered though the MMF and the GRIN lens cannot be increased too much in fear of damaging the optics, decreasing the beam diameter is the only way to increase the fluence. The low fluence of current sub-probe mainly results from the diverging beam caused by the higher modes transmitted by the 105 μm diameter MMF. Using a smaller core fiber is an efficient way to reduce the beam spot size, and the development of a sub-probe using a smaller core MMF is described in the next section.

6.8 Simulation, fabrication and testing of excitation sub-probe using 25 μm core MMF

A 25 μm core MMF (FG025LJA, Thorlabs) is chosen to build the new sub-probe. The same Zemax simulation as described in Section 6.3 is conducted and an optimal distance of 0.13 mm between the fiber tip and GRIN lens is found from the simulation. The resulting beam diameter at the 5.5 mm target depth is 152.5 μm. However, this separation between the fiber and the GRIN lens is too small for the optics to survive after long time use. Thus, the distance is intentionally increased to 0.38 mm to decrease the fluence at the surface of the GRIN lens. This results in a beam diameter of about 350 μm measured by a beam profiler. Figure *6.12* shows the simulation results when the separation is set to 0.38 mm. The beam diameter of at a depth of 5.5 mm is about 333 μm, which is close to the measurement. Note that the beam diameter is calculated by the RMS radius multiplied by $\sqrt{2}$, since the 25 μm core now contains fewer modes so GEO radius is no longer accurate to describe the beam diameter. After the assembly, the output energy is about 41 μJ at a maximum current of 35 A. Although the energy is lower compared to 79 μJ at 40 A, the beam diameter decreases from 1 mm to 350 μm, resulting in a fluence increase by a factor of more than 4. The third set of phantom described in Section 6.7 is imaged again to test the performance of the new sub-probe. The MIP images are shown in Figure *6.13*. This time the wires are imaged clearly by the 25 μm MMF-based sub-probe, thanks to the increase in the fluence at the imaging depth. Thus, the later experiments are conducted using this 25 μm sub-probe.

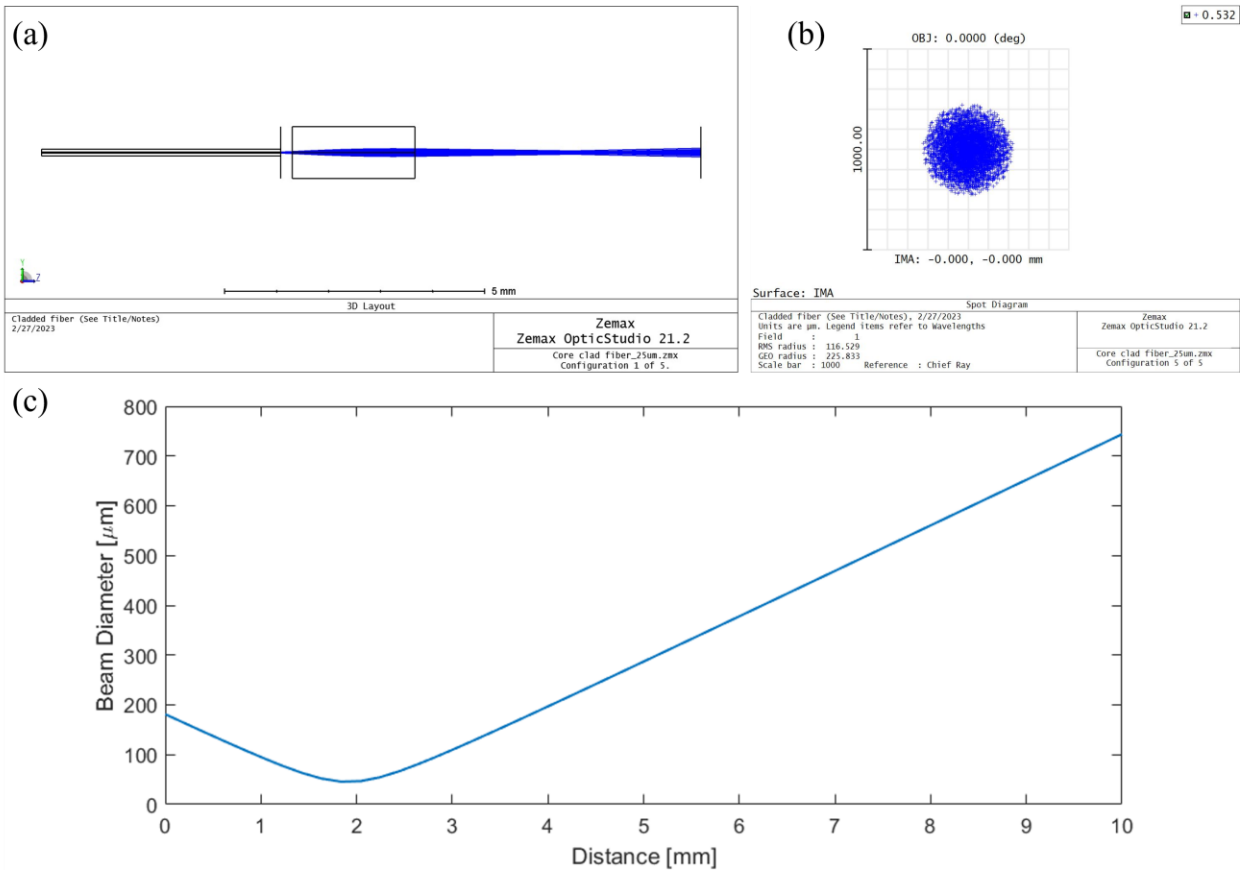

Figure 6.12 Zemax simulation of beam profile of a 25 μm core MMF based sub-probe

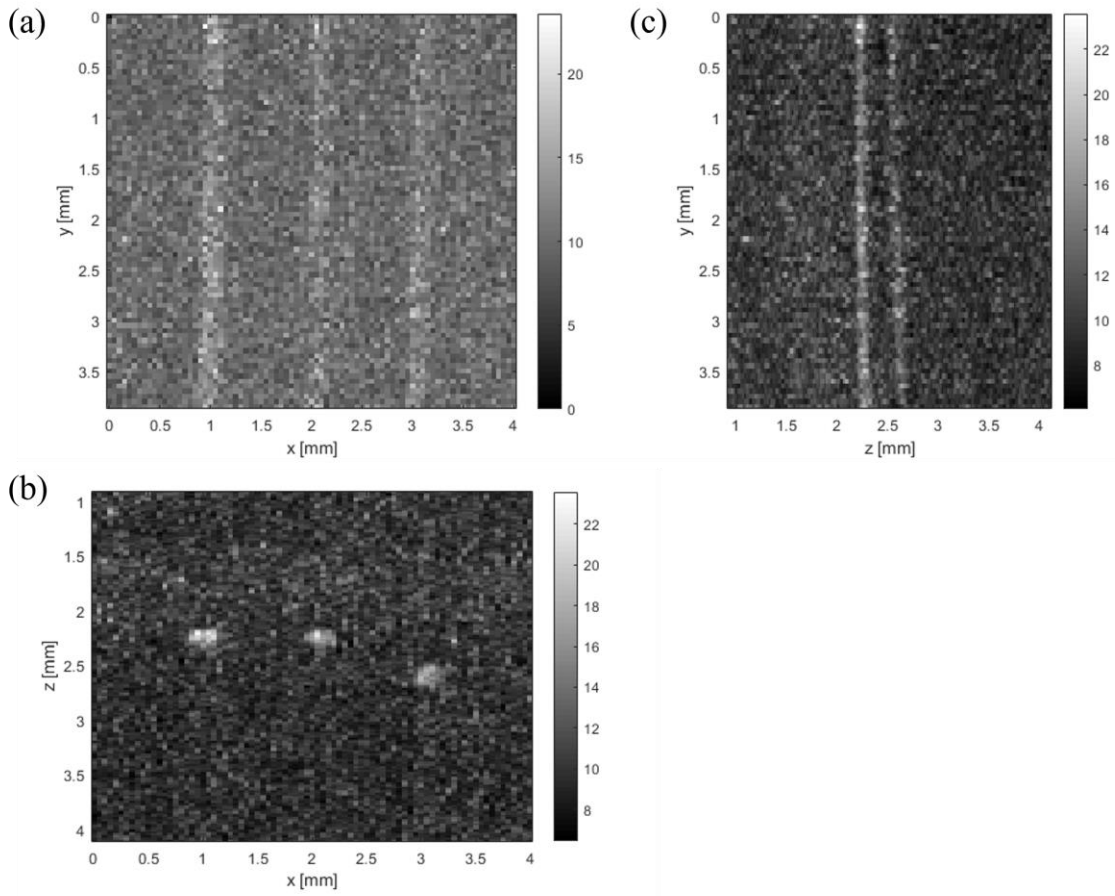

Figure 6.13 MIP images of 42 AWG wire phantom

6.9 In vivo imaging of nude mouse ear

A nude mouse is used to image the blood vessels of the ear. The nude mouse is placed in the bottom container of the assembly shown in Figure *6.9*. The ear is firstly applied with hair remover and then cleaned by distilled water. Next US gel is applied to the ear before the top tank is place onto the ear. The ear is made sure to be in good contact with the membrane of the imaging window of the tank. Figure *6.14* shows the results of the in vivo imaging of ear blood vessels of a nude mouse. Panel (a) shows a photo of the ear of the nude mouse, and the area in the red square is the imaging field of view. A zoomed in version of the photo is shown in panel (b). Panel (c) to (e) are the MIP images of the 3-D data set. The scanning field of view is 4 mm by 4 mm with a

pixel size of 0.05 mm as before. The total imaging time is about 30 min, and the mouse is under anesthetization using isoflurane during the whole imaging session. The xy MIP image in Figure *6.14* (c) clearly shows the structure of the blood vessels of the mouse ear, demonstrating the capability of the sub-probe based PAI system to reveal the structures of biological tissues in vivo.

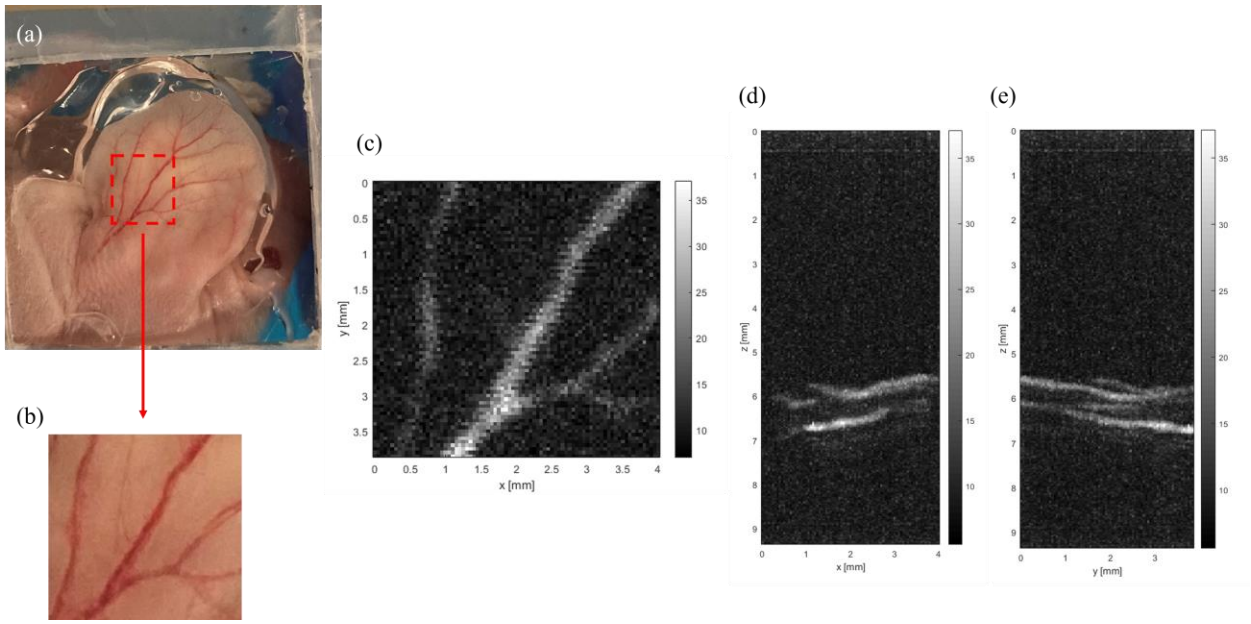

Figure 6.14 Photo and MIP images of the ear of a nude mouse

6.10 Assembly of 804 nm probe

PAI system based on sub-probe assembly and 532 nm excitation laser has been demonstrated to image the mouse ear. However, to improve imaging depth and provide more molecular information of the tissue, a near-infrared wavelength is appreciated, and a corresponding sub-probe design is needed. To transform the setup into a NIR system, the fiber coupling is first updated. The original output fiber bundle of the tunable Opotek laser is replaced with home-made coupling optics, as shown in Figure *6.15*. The laser is coupled into a 1500 μm diameter large core multi-mode fiber MMF1 (M107L02, Thorlabs) by a lens L1 (LA1509-B, Thorlabs) to be delivered to the fiber launch system. The output of MMF1 is collimated by a fiber collimator L2 (F810SMA-780, Thorlabs). Since the beam quality of the Opotek laser is poor in exchange for higher pulse

energy, another pair of lenses L3 (LA1608-B, Thorlabs) and L4 (LA1131-B, Thorlabs) are used to collimate the laser beam to a proper diameter before entering the objective. A pair of broadband dielectric mirrors M1 (BB1-E03, Thorlabs) and M2 (BB1-E03, Thorlabs) are used to fine align the laser beam. A 20X objective (M-20X, Newport) is used to couple the laser beam into the same type of multi-mode fiber MMF2 (FG105LVA, Thorlabs) that has been used to construct the 532 nm probe. Although the NA of MMF2 is 0.1, which is much smaller than the NA of the objective, 0.4, the beam cannot be focused into a tight spot due to the poor quality, thus making the real NA of the beam close to that of the MMF2. The previously used 5X objective (M-5X, Newport) was used to compare the coupling efficiency and there seemed to be no significant energy output from the fiber. The tip of MMF2 is held by the same fiber chuck (FPH-J, Newport) and the same 3-axis stage fiber launch system (MBT613D, Thorlabs) is used to perform fine alignment. Since the NIR wavelength cannot be seen by the human eye, a 650 nm laser pen (visual fault locator) is used to achieve maximum coupling efficiency before switching to the pulsed laser.

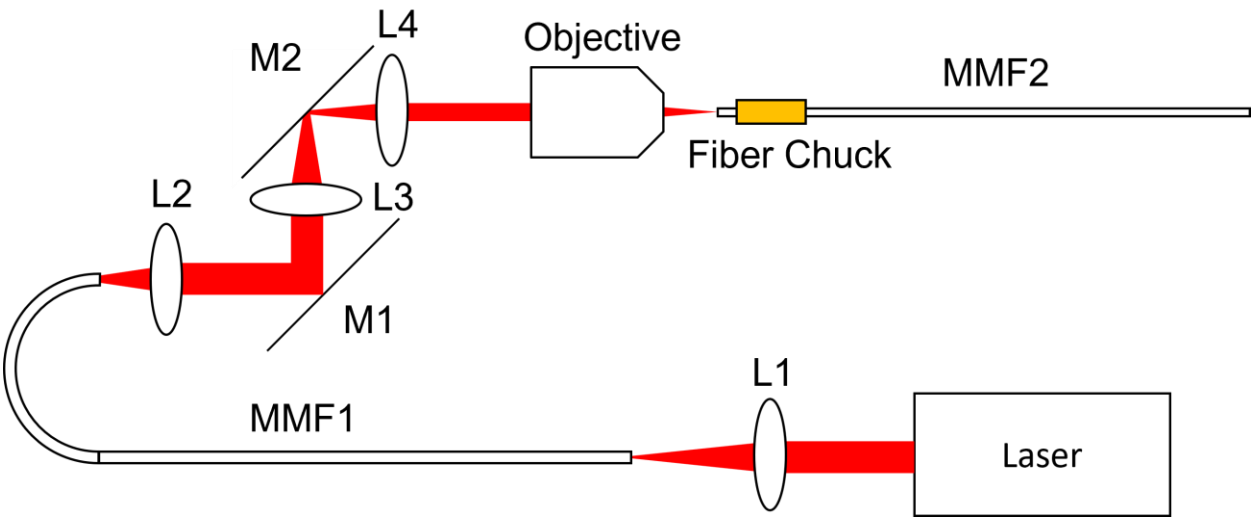

Figure 6.15 Schematic of coupling of Opotek laser

From previous results using a coated GRIN lens, the anti-reflection coating didn't help much to prevent laser burning, but the distance between the fiber tip and the GRIN lens played a

more important role. Thus, a 1 mm uncoated GRIN lens with a 0.12 mm working distance (#64-524, Edmund Optics) is used for 804 nm probe design. The optimal distances between the fiber tip and the GRIN lens are found by Zemax simulation for both 804 nm and 650 nm because the 650 nm will be used for alignment. The optimal distance for both case is 0.3158 mm, creating a beam diameter of 647.8 µm and 623.3 µm at an imaging depth of 5.5 mm. The beam profiles at different depths are plotted in Figure *6.16*.

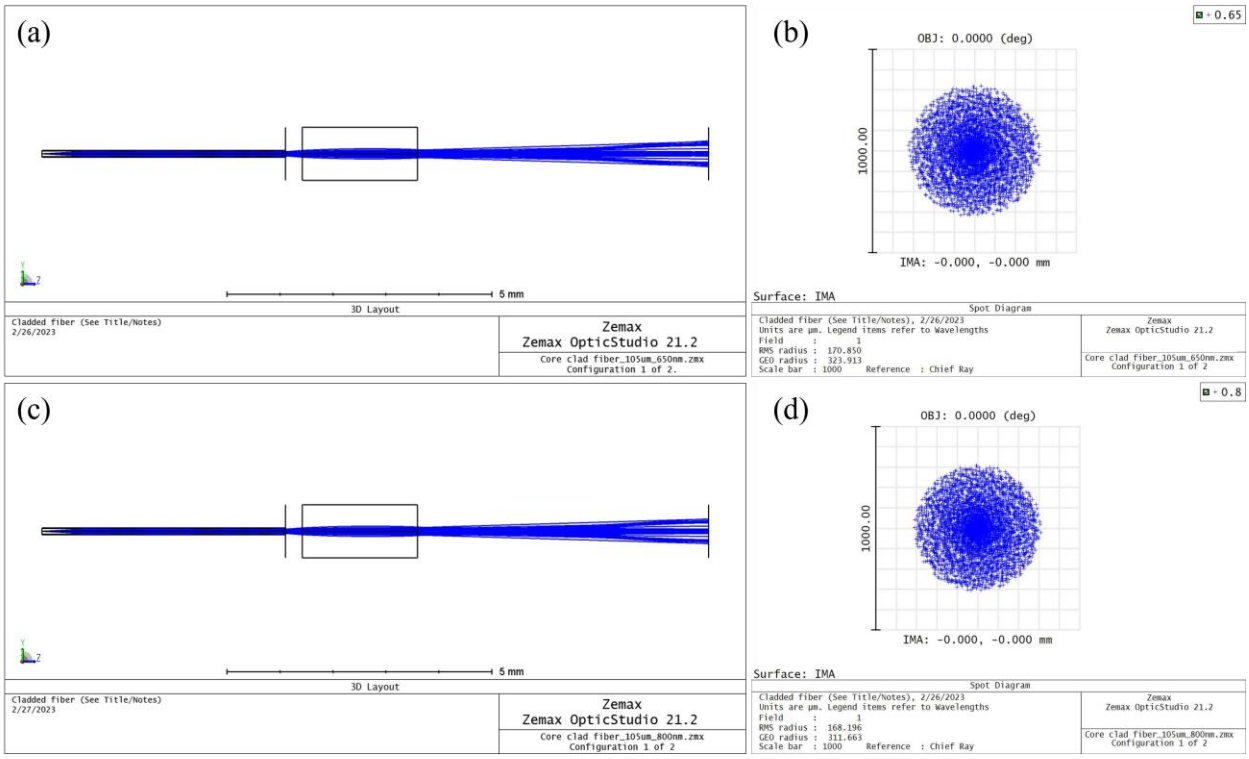

Figure 6.16 Zemax simulations of 650 nm and 800 nm beams propagating through the MMF and GRIN lens

The sub-probe is assembled in a similar way as described in Section 6.5, as shown in Figure *6.17*. Since the NIR pulsed laser has a low repetition rate and its beam profile cannot be measured by the beam profiler accurately, the output beam is not monitored during assembly. Instead, the distance between the fiber tip and the GRIN lens is carefully monitored by counting pixels from the microscope. Once the desired 0.3158 mm distance is achieved, the glass ferrule is glued to the metal tube and the beam profile at different distances are measured using the 650 nm laser pen to

validate the design. The data is plotted along with the Zemax simulation results, as shown in Figure *6.18*. It can be seen that the measured beam diameters match the simulation very well. Thus, the simulation results for 804 nm should represent the real diameters with satisfying accuracy. The beam diameter at the target depth of 5.5 mm is about 646 µm, and it indicates the lateral resolution of the probe. The total energy output from the probe is 263 µJ, which is much higher than the output of a 532 nm probe. Thus, the 804 nm probe is promising to have higher PA signal levels.

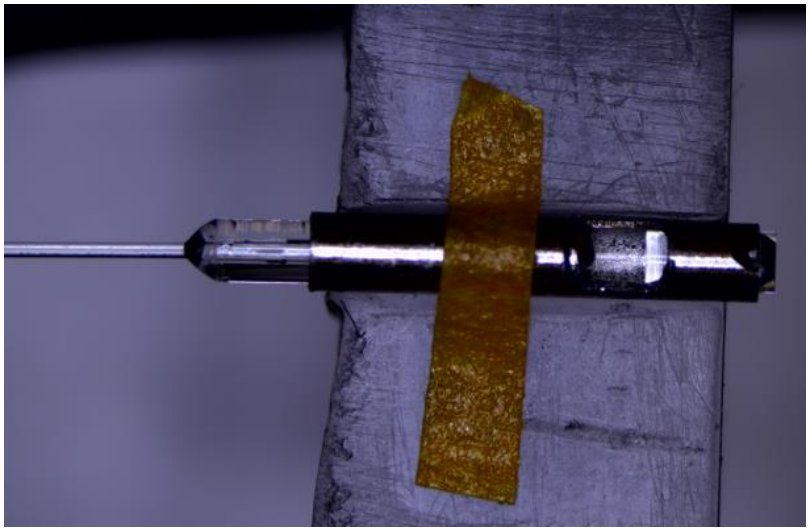

Figure 6.17 Photo of assembled 800 nm sub-probe

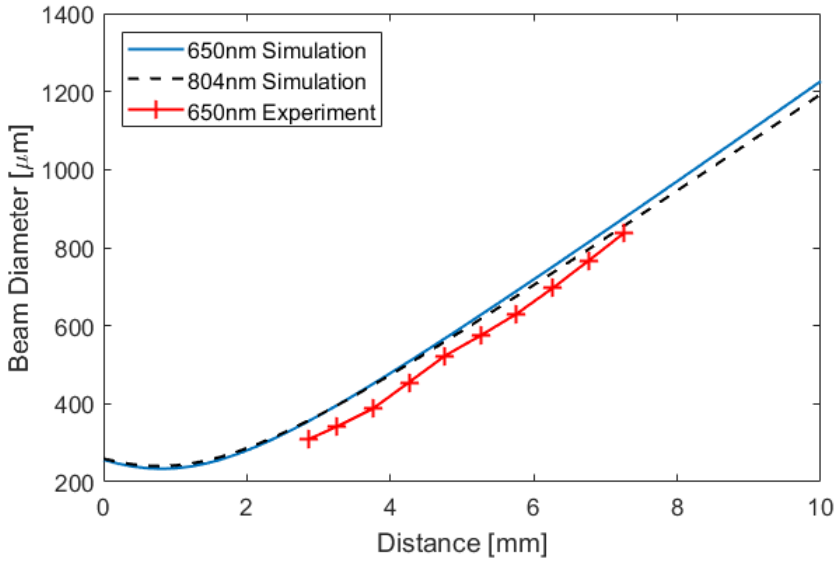

Figure 6.18 Simulation and experiment results of beam diameters at different depths

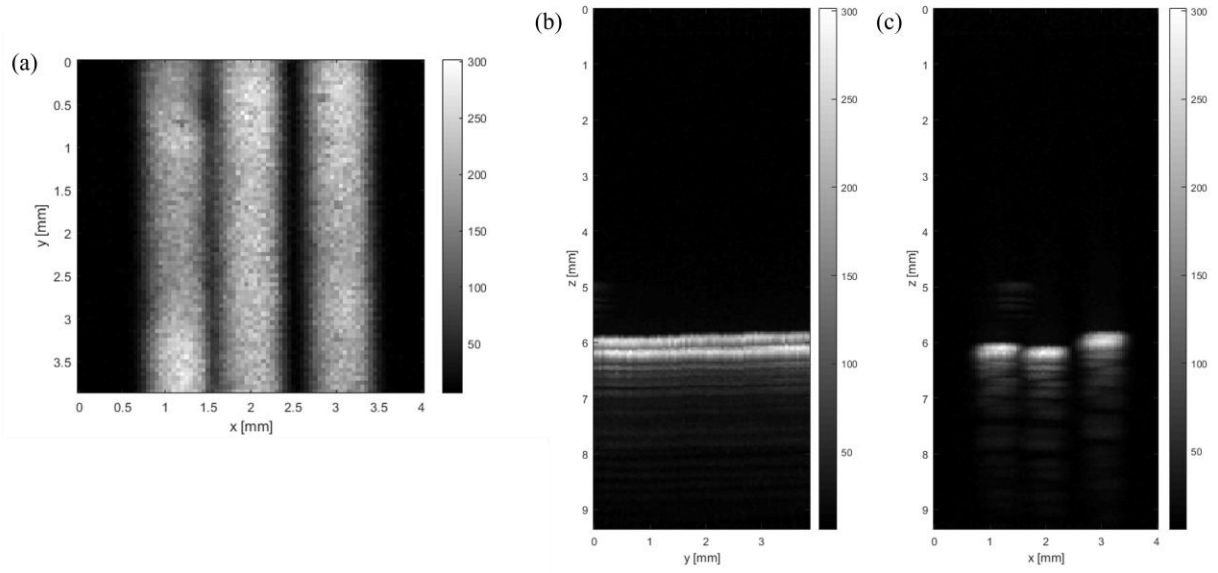

Figure 6.19 MIP images of horizontally placed pencil lead phantoms

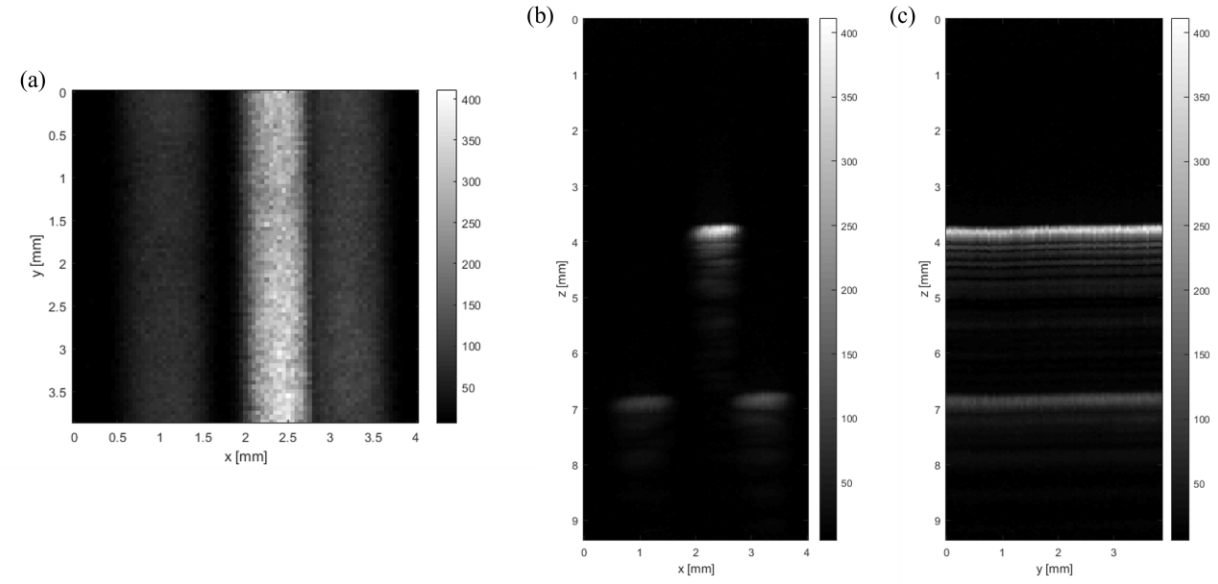

Figure 6.20 MIP images of triangularly placed pencil lead phantoms

Phantom imaging using the same pencil leads are used to test the performance of the 804 nm sub-probe. MIP images are shown in Figure *6.19* and Figure *6.20*. The signal levels are much higher compared to those of the 532 nm sub-probe in Figure *6.10* and Figure *6.11*. Thus, this sub-probe is promising for deep tissue imaging.

6.11 In vivo imaging of prolapsed mouse

In vivo imaging is conducted on prolapsed CPC-APC mouse using the newly assembled 804 nm sub-probe. The previous tabletop imaging system is modified to adjust to the requirements of in vivo mouse imaging, as shown in Figure *6.21*. The interrogation laser is flipped to go upwards and the FP sensor is mounted on the bottom of a tank. The mouse is placed in a customized holder made from a plastic tube. The bottom of the tube is sealed with a transparent membrane as an imaging window. The top of the tube is connected to a nose cone to anesthetize the mouse during imaging. Both the tank and the tube are filled with water for acoustic coupling. The excitation laser goes through an imaging window made from a glass cover slide and illuminates the prolapse of the mouse. The tube is mounted on a motorized linear stage for 2-D raster scanning to form the images.

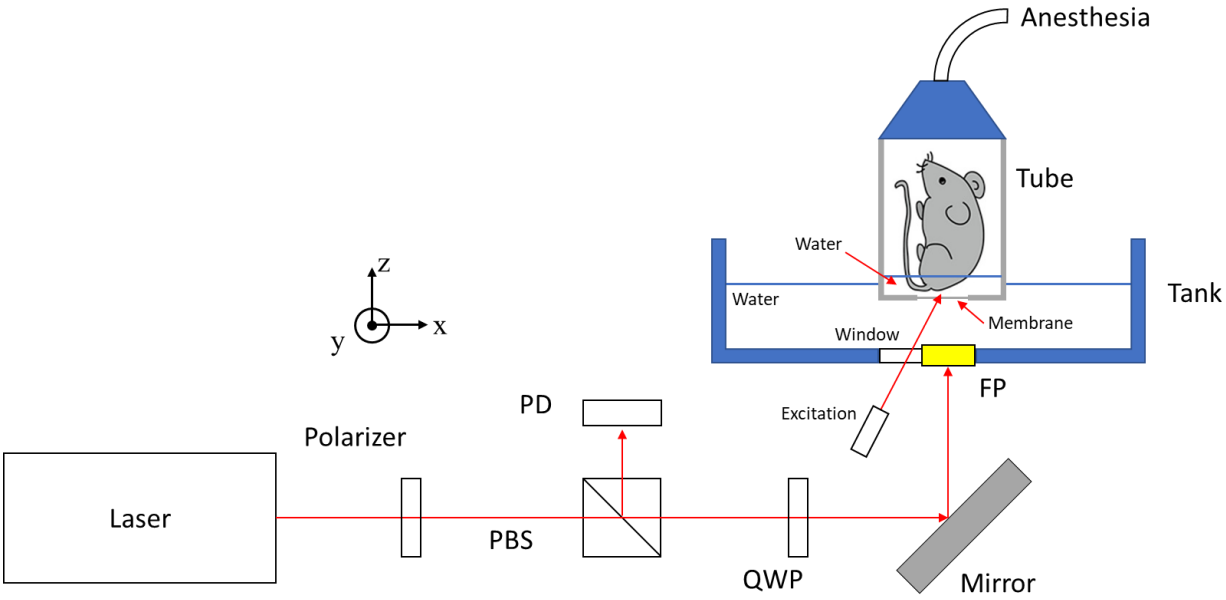

Figure 6.21 Schematic of setup of in vivo imaging of prolapsed mouse

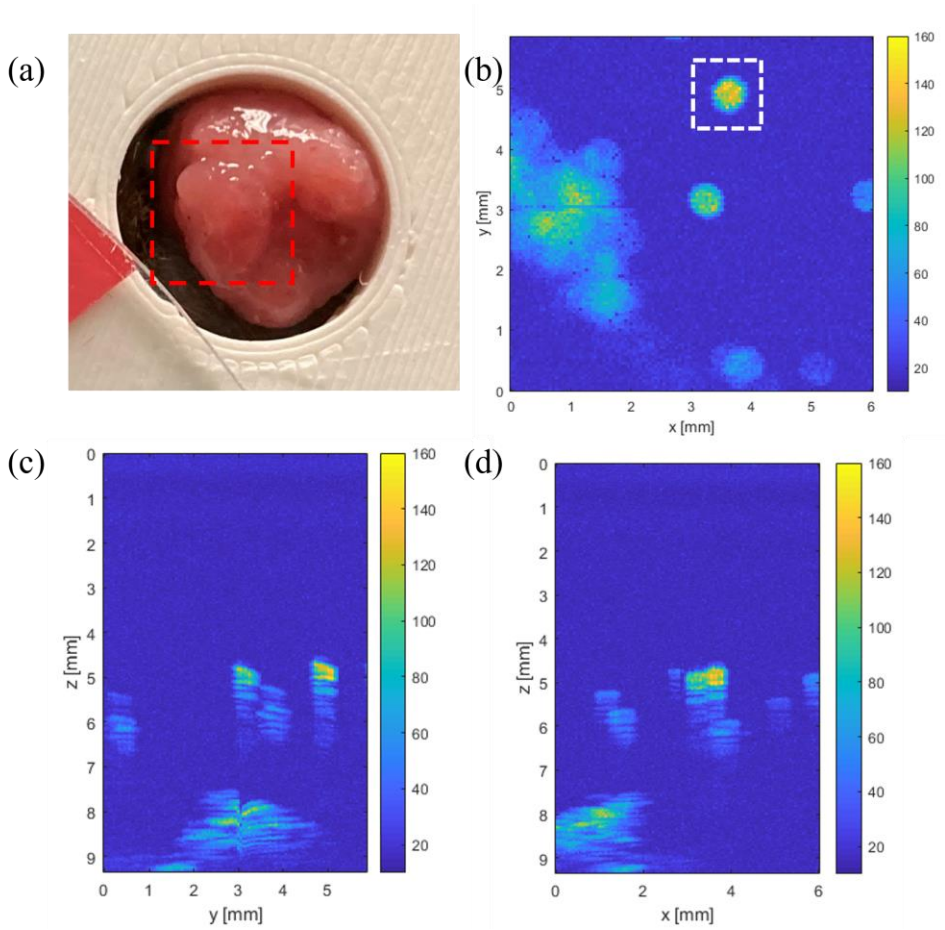

Figure 6.22 MIP images of the prolapse region of an APC-CPC mouse

200 µL of gold nanoshell solution was IV injected into the tail vain of the mouse before imaging. The mouse is imaged about 8 hours after the injection. Figure *6.22* (a) shows a photo of the prolapsed region and (b) to (d) show the MIP images of the prolapsed region. The scanning field of view is 6 mm by 6 mm with a pixel size of 0.05 mm as before. The total imaging time is about 60 min. The first thing to notice is a wide region of unknown object in the xy image in panel (b). They turn out to be the signal from the mouse hair near the anus of the mouse. The evidence is that these signals occur at a large depth, which should not come from the prolapsed tissue which is in contact with the membrane. It makes sense if they come from the hair of the mouse which is further away from the sensor. The signals from the prolapse tissue appear in the form of ellipse, and they appear at nearer imaging depths, as shown in the yz and xz images in panel (c) and (d).

They represent small polyps grown on the prolapse tissue where the gold nanoshell has accumulated due to EPR effect. The brightest polyp is indicated in the white dashed square in panel (b), and MIP images using the 3-D data in the vicinity of the indicated region are shown in Figure *6.23*. The zoomed images reveal the depth of the selected polyp and demonstrate the depth-resolving ability of PA imaging.

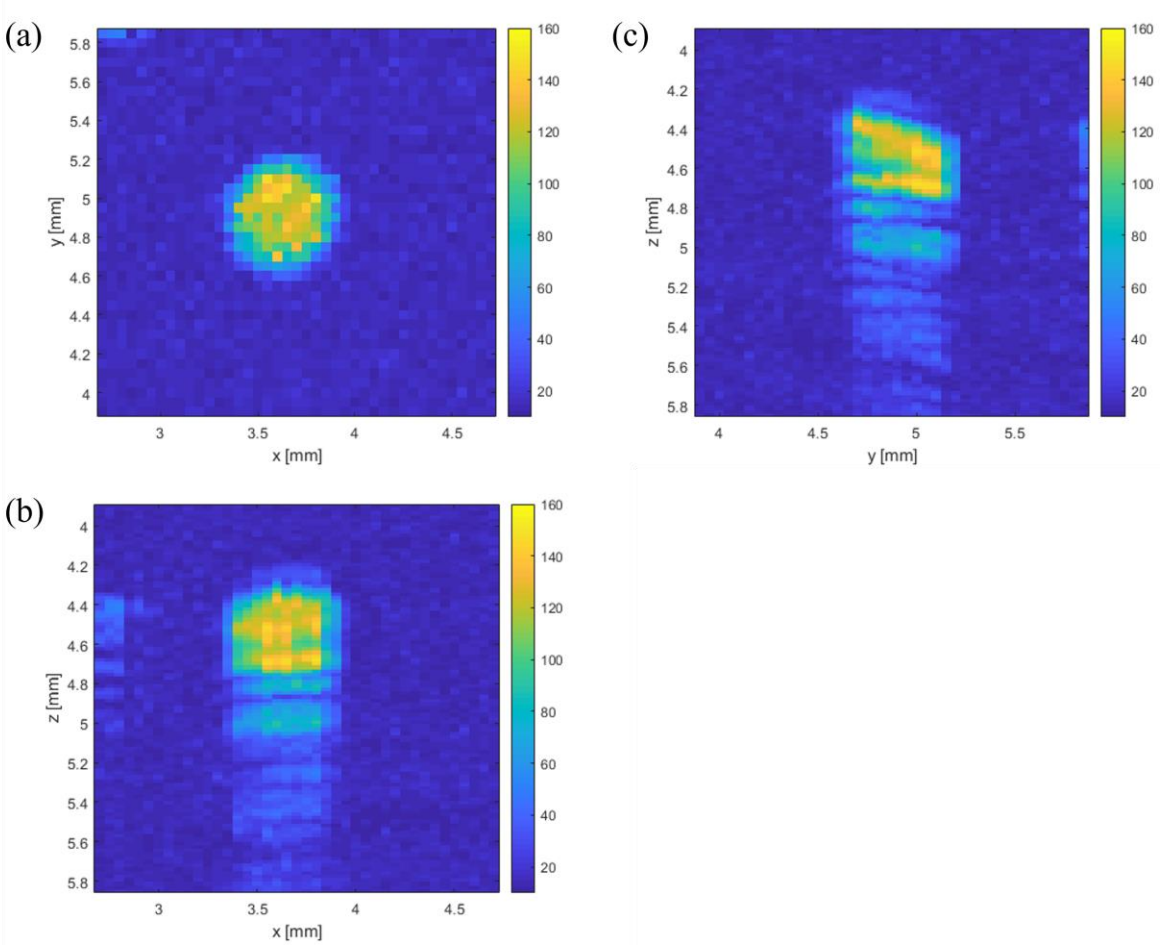

Figure 6.23 Zoomed in MIP images of the region indicated by white dashed square in Figure 6.21

Next, the time course experiment is conducted on the prolapsed mouse after IV injection of the same amount of gold nanoshell solution. Figure *6.24* shows the xy MIP images of a selected polyp imaged at different times. The peak signal occurs at around 8 hours after the injection, and the nanoshell appears to clear after 24 hours. A Python code is developed to calculate the target-

to-background (T/B) ratio of each image. First, Chan-Vese algorithm [81] is used to select the polyp region from the image at 8 hours as the target area. Then dilation method is used to select a region of 10 pixels away from the boundary of the target area as the background area. The averaged value of pixel intensities in the target and background areas are calculated and the ratio between them is the T/B ratio of this image. Finally, the same target and background masks are applied to the images at other times to calculate the corresponding T/B ratios. They are plotted in Figure *6.24* (f). The T/B ratio starts at a value of 1, meaning that there is no significant signal right after the injection. The T/B ratio keeps increasing until it reaches the peak at about 8 hours and then falls back to 1 after about 24 hours from the injection. These results show the ability of the proposed PAE system for vivo tissue imaging for cancer detection and staging.

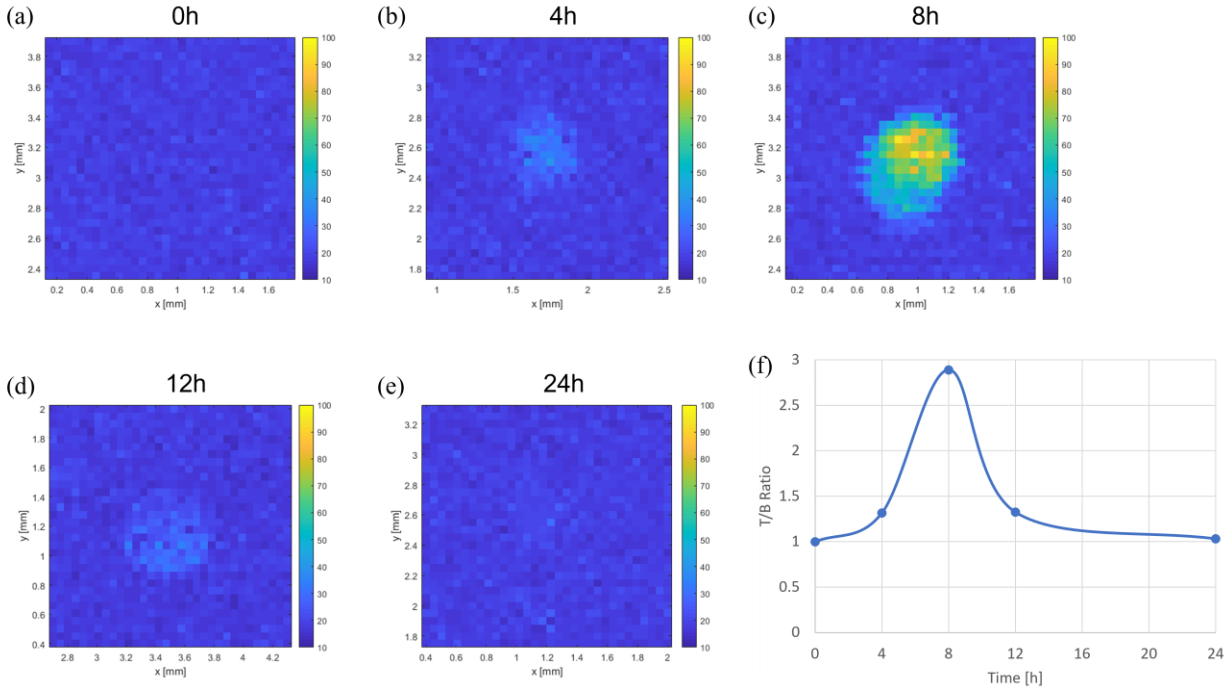

Figure 6.24 MIP images of polyp and T/B ratio at different times

Chapter 7 Discussion and Conclusion

Photoacoustic endoscopy (PAE) is an emerging imaging technology that combines the advantages of molecular imaging of optics and deep penetration of ultrasound. Various designs of PAE have been proposed, however, they all have different limitations and these limitations raise a need for a highly sensitive, transparent, and miniaturized sensor array for PAE systems. Fabry-Perot polymer film ultrasound sensor is an excellent candidate to overcome these challenges. Efforts have been made to implement FP based sensors into PAE systems and front-viewing imaging probes have been demonstrated using fiber bundle-based FP sensor array. However, there is still a need for cheaper and simpler FP sensor that can get rid of a tunable laser.

In this dissertation, we propose using thin wafer-based FP sensor to fabricate miniaturized and cost-effective sensor array for PAE applications. First, the dynamics of a FP sensor with a thin substrate is studied to verify the feasibility of such sensors. It turns out that the frequency response of a thin substrate-based sensor only differs from that of an infinitely thick sensor by a frequency filter. This filter is formed from the multi-reflection of acoustic waves inside of the substrate and can be explicitly derived from the information of the substrate and the coatings. Thus, using a thin substrate for miniaturization will not affect the acoustic performance of the sensor.

The thin wafer-based FP sensor also enables working with a fixed wavelength laser for interrogation. Although the wafer-based sensor also shows a non-uniform sensitivity across the surface of the whole wafer, the thin wafer enables dicing of the whole sensor to get the part with relatively uniform region, then a single wavelength laser can be used to interrogate this region without sacrificing sensitivity. For endoscopic applications, 1-D array is sufficient to form images

without scanning mechanism, thus the tolerance on the non-uniformity becomes even higher as long as there is a line that can be used on the wafer. The same fabrication process as the current FP sensors can be directly applied to the wafer-based miniaturized sensor, and dicing turns out to be usually safe to keep the usable patterns on the wafer. A 9 mm by 2 mm rectangular sensor array is fabricated and a tabletop system is built to conduct tomographic imaging. The system clearly shows the structure of a phantom made from a knotted wire and ex vivo imaging of the polyps from a CPC-APC mouse colon is also conducted.

However, there are still limitations to this miniaturized sensor. As a proof of concept, gold coatings are used as the reflective mirrors on the sides of the Parylene C film. Although high reflectivity and sensitivity are achieved, the transparency advantage of the FP sensor is not realized. Thus, the excitation laser has to be placed on the side of the sensor and illuminates the target imaging region at an angle. This forces the imaging target to be placed at a distance from the sensor where the excitation laser beam intersects the imaging plane. The decay of excitation laser during travelling to the target and the illumination at an angle will both reduce the overall sensitivity of the imaging system.

The surface sensitivity is not uniform due to the thickness variation of the Parylene C film during deposition. Although this thickness gradient creates the usable area for a single wavelength interrogation laser, the size of the usable area is limited and the yield is low. As discussed before, the wafer is slowly spinning during the deposition, and this is the reason why there is a thickness gradient. Thus, by slowing the wafer down or even stopping it form spinning, we should be able to decease the thickness variation and thus increasing the yield of usable sensors.

The best NEP demonstrated in this study is 0.76 kPa, which is worse than most of the recently reported values of other FP sensors [43], [54], [61], but it’s still comparable to some

proposed sensors [41]. The NEP can be improved by either increasing the sensitivity or decreasing the noise. The sensitivity will be mostly increased by using non-absorbing dielectric mirrors. The noise of the imaging system mostly comes from the interrogation laser which is further amplified by the photodetector which has a built-in transimpedance amplifier. Thus, a low noise interrogation laser will be preferred to increase system performance.

The sensor has a measured -3dB bandwidth of 16.6 MHz. While on the same order of magnitude, it is only 82% of the designed bandwidth. The discrepancy may come from the lack of high frequency components of the source 10 MHz ultrasound transducer, since the low-frequency region and the peak response match the simulation well. Further investigation could be done by using a higher frequency transducer.

For PAE probe design, the thin rectangular 1-D array will be ideal for being placed along the axial direction of the probe, making it perfect for a side-viewing configuration. However, there is a lack of line scan technology for miniaturized probe, so the implementation of the FP sensor array is a problem remained to be solved. Based on this situation, a 2 mm by 2 mm square sensor is fabricated to work as a single element sensor to verify the feasibility of being integrated into a PAE probe. A PAE miniaturized probe is designed, and the sub-probe for 532 nm excitation laser is assembled. Phantom imaging and in vivo imaging of the ear of a nude mouse are conducted. To verify the feasibility for deep tissue imaging and cancer staging, another 804 nm sub-probe was assembled. Phantom imaging and in vivo imaging of prolapsed CPC-APC mouse are conducted. These show that the miniaturized FP sensor is promising to be implemented into a PAE imaging probe.

There are several fundamental hardware constraints that limit the system performance. First, the real ITF could have been measured with a tunable laser near 633 nm. Second, the frame

rate is currently limited by the slow repetition rate of only 10 Hz of the pulsed laser. For the single element sensor setup, the slow raster scanning also limits the frame rate. These constraints could be overcome by future development of laser and scanning technologies.

In summary, the miniaturized size, transparency potential, single wavelength operation, and feasibility of forming sensor array make this new type of FP sensor an excellent candidate for photoacoustic endoscopy applications. It will be particularly useful in tumor staging because of its depth resolving capability with molecular contrast.

Chapter 8 Future Work

Some constraints mentioned in the last section could be lifted by future advancement of technologies, while some work can be done in the near future to improve the performance of the current sensor. Dielectric coatings which are transparent at the excitation wavelength while highly reflective at the interrogation wavelength can be applied to this type of FP sensor, and quite a few different types of coatings have already been demonstrated in literature [54], [82], [83]. The feasibility of applying these coatings to the wafer-based FP sensor and dicing them need to be studied. Once miniaturized sensors with dielectric coatings are fabricated, new PAE probes can be designed based on the new sensors. Figure *8.1* shows a conceptual picure of the PAE probe design using a 2 mm FP sensor with dielectric coatings. The dimensions of most of the components are the same as the design in Section 6.1.The difference is that a single sub-probe is used for both detection and excitation laser, because this time the FP sensor can be highly reflective to the detection laser while transparent to the excitation laser. A 2 mm prism is used instead and the FP sensor is placed in the center of the prism, forming a coaxial configuration. The sensitivity should be increased due to the low absoption dielectric coatings and conaxial configuration. There is more spare space in the probe so it can be further scaled down, making it promising for miniaturized imaging probes.

As discussed in Chapter 7, the thickness variation of the Parylene C can possibly be reduced by slowing down the spinning speed of the wafer. This needs to be verified and it will be benifitial to increasing the yield of usable sensors. On the other hand, the current 2 mm by 2 mm square sensor and the sub-probe for excitation can already be integrated into a miniaturized probe. The

miniaturized probe could enable in vivo imaging of mouse colon or other tissues, thus greatly widening the application of the FP sensors in PAI.

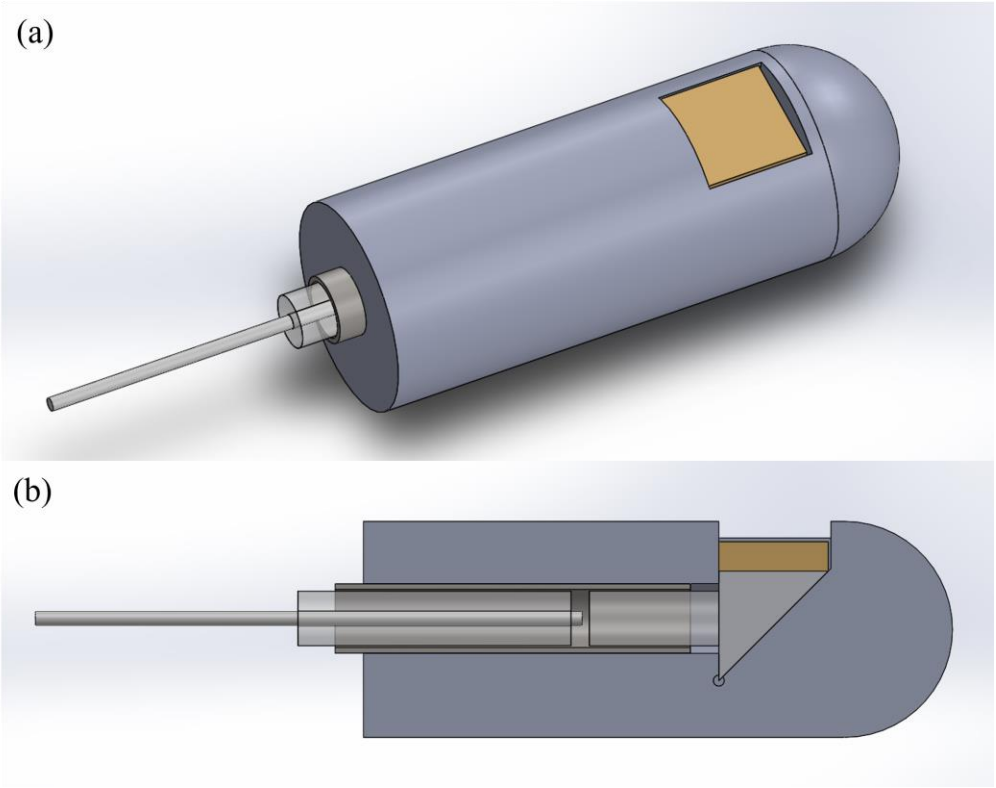

Figure 8.1 New PAE probe design using dielectric coatings

Bibliography

[1] American Cancer Society, "Cancer Facts & Figures 2023," *Atlanta: American Cancer Society*, 2023.

[2] American Cancer Society, "Colorectal Cancer Facts & Figures 2020-2022," *Atlanta: American Cancer Society*, 2020.

[3] T. D. Mast, "Empirical relationships between acoustic parameters in human soft tissues," *Acoustics Research Letters Online*, vol. 1, no. 2, pp. 37–42, Oct. 2000, doi: 10.1121/1.1336896.

[4] L. V. Wang and H. Wu, *Biomedical Optics: Principles and Imaging*. John Wiley & Sons, 2012.

[5] A. G. Bell, "Upon the production and reproduction of sound by light," *Journal of the Society of Telegraph Engineers*, vol. 9, no. 34, pp. 404–426, 1880, doi: 10.1049/jste-1.1880.0046.

[6] G. J. Diebold, "Photoacoustic Monopole Radiation: Waves from Objects with Symmetry in One, Two, and Three Dimensions," in *Photoacoustic Imaging and Spectroscopy*, CRC Press, 2009.

[7] M. Xu and L. V. Wang, "Universal back-projection algorithm for photoacoustic computed tomography," *Phys. Rev. E*, vol. 71, no. 1, p. 016706, Jan. 2005, doi: 10.1103/PhysRevE.71.016706.

[8] Y. Xu, D. Feng, and L. V. Wang, "Exact frequency-domain reconstruction for thermoacoustic tomography. I. Planar geometry," *IEEE Transactions on Medical Imaging*, vol. 21, no. 7, pp. 823–828, Jul. 2002, doi: 10.1109/TMI.2002.801172.

[9] L. V. Wang and S. Hu, "Photoacoustic Tomography: In Vivo Imaging from Organelles to Organs," *Science*, vol. 335, no. 6075, pp. 1458–1462, Mar. 2012, doi: 10.1126/science.1216210.

[10] D. Li, L. Humayun, E. Vienneau, T. Vu, and J. Yao, "Seeing through the Skin: Photoacoustic Tomography of Skin Vasculature and Beyond," *JID Innovations*, vol. 1, no. 3, p. 100039, Sep. 2021, doi: 10.1016/j.xjidi.2021.100039.

[11] J. Yao and L. V. Wang, “Photoacoustic microscopy,” *Laser & Photonics Reviews*, vol. 7, no. 5, pp. 758–778, 2013, doi: 10.1002/lpor.201200060.

[12] A. Sun *et al.*, “Multicolor Photoacoustic Volumetric Imaging of Subcellular Structures,” *ACS Nano*, vol. 16, no. 2, pp. 3231–3238, Feb. 2022, doi: 10.1021/acsnano.1c11103.

[13] X. Li, L. Kang, Y. Zhang, and T. T. W. Wong, “High-speed label-free ultraviolet photoacoustic microscopy for histology-like imaging of unprocessed biological tissues,” *Opt. Lett., OL*, vol. 45, no. 19, pp. 5401–5404, Oct. 2020, doi: 10.1364/OL.401643.

[14] X. Luo, X. Li, C. Wang, W. Pang, B. Wang, and Z. Huang, “Acoustic-resolution-based photoacoustic microscopy with non-coaxial arrangements and a multiple vertical scan for high lateral resolution in-depth,” *Appl. Opt., AO*, vol. 58, no. 33, pp. 9305–9309, Nov. 2019, doi: 10.1364/AO.58.009305.

[15] C. Fang and J. Zou, “Acoustic-resolution photoacoustic microscopy based on an optically transparent focused transducer with a high numerical aperture,” *Opt. Lett., OL*, vol. 46, no. 13, pp. 3280–3283, Jul. 2021, doi: 10.1364/OL.423287.

[16] Z. Xie *et al.*, “In vivo intravascular photoacoustic imaging at a high speed of 100 frames per second,” *Biomed. Opt. Express, BOE*, vol. 11, no. 11, pp. 6721–6731, Nov. 2020, doi: 10.1364/BOE.405792.

[17] R. Lin *et al.*, “Miniature intravascular photoacoustic endoscopy with coaxial excitation and detection,” *Journal of Biophotonics*, vol. n/a, no. n/a, p. e202200269, doi: 10.1002/jbio.202200269.

[18] N. Liu, S. Yang, and D. Xing, “Photoacoustic and hyperspectral dual-modality endoscope,” *Opt. Lett., OL*, vol. 43, no. 1, pp. 138–141, Jan. 2018, doi: 10.1364/OL.43.000138.

[19] Z. Wang, F. Yang, H. Ma, Z. Cheng, and S. Yang, “Photoacoustic and ultrasound (PAUS) dermoscope with high sensitivity and penetration depth by using a bimorph transducer,” *Journal of Biophotonics*, vol. 13, no. 9, p. e202000145, 2020, doi: 10.1002/jbio.202000145.

[20] T. Guo, K. Xiong, Z. Zhang, L. Li, and S. Yang, “In vivo anatomical imaging of colorectum by tens-of-micron-resolved photoacoustic/ultrasonic endoscope,” *Appl. Phys. Lett.*, vol. 118, no. 15, p. 153702, Apr. 2021, doi: 10.1063/5.0049855.

[21] T. Zhao, M. Zhang, S. Ourselin, and W. Xia, “Wavefront Shaping-Assisted Forward-Viewing Photoacoustic Endomicroscopy Based on a Transparent Ultrasound Sensor,” *Applied Sciences*, vol. 12, no. 24, Art. no. 24, Jan. 2022, doi: 10.3390/app122412619.

[22] Y. Li *et al.*, “High-Speed Integrated Endoscopic Photoacoustic and Ultrasound Imaging System,” *IEEE Journal of Selected Topics in Quantum Electronics*, vol. 25, no. 1, pp. 1–5, Jan. 2019, doi: 10.1109/JSTQE.2018.2869614.

[23] H. Lei *et al.*, “Characterizing intestinal strictures of Crohn’s disease in vivo by endoscopic photoacoustic imaging,” *Biomed. Opt. Express, BOE*, vol. 10, no. 5, pp. 2542–2555, May 2019, doi: 10.1364/BOE.10.002542.

[24] Y. Cao *et al.*, “Fast assessment of lipid content in arteries in vivo by intravascular photoacoustic tomography,” *Sci Rep*, vol. 8, no. 1, Art. no. 1, Feb. 2018, doi: 10.1038/s41598-018-20881-5.

[25] G. Li, Z. Ye, S. Liang, and S.-L. Chen, “Miniature probe for dual-modality photoacoustic microscopy and white-light microscopy for image guidance: A prototype toward an endoscope,” *Journal of Biophotonics*, vol. 13, no. 4, p. e201960200, 2020, doi: 10.1002/jbio.201960200.

[26] L. Lin *et al.*, “IVUS\IVPA hybrid intravascular molecular imaging of angiogenesis in atherosclerotic plaques via RGDfk peptide-targeted nanoprobes,” *Photoacoustics*, vol. 22, p. 100262, Jun. 2021, doi: 10.1016/j.pacs.2021.100262.

[27] J. Leng *et al.*, “Multi-spectral intravascular photoacoustic/ultrasound/optical coherence tomography tri-modality system with a fully-integrated 0.9-mm full field-of-view catheter for plaque vulnerability imaging,” *Biomed. Opt. Express, BOE*, vol. 12, no. 4, pp. 1934–1946, Apr. 2021, doi: 10.1364/BOE.420724.

[28] W. Yang *et al.*, “Photoacoustic-fluorescence microendoscopy in vivo,” *Opt. Lett., OL*, vol. 46, no. 10, pp. 2340–2343, May 2021, doi: 10.1364/OL.425753.

[29] M. Kim *et al.*, “Intra-instrument channel workable, optical-resolution photoacoustic and ultrasonic mini-probe system for gastrointestinal endoscopy,” *Photoacoustics*, vol. 26, p. 100346, Jun. 2022, doi: 10.1016/j.pacs.2022.100346.

[30] K. Kim *et al.*, “Tapered catheter-based transurethral photoacoustic and ultrasonic endoscopy of the urinary system,” *Opt. Express, OE*, vol. 30, no. 15, pp. 26169–26181, Jul. 2022, doi: 10.1364/OE.461855.

[31] K. Xiong, S. Yang, X. Li, and D. Xing, “Autofocusing optical-resolution photoacoustic endoscopy,” *Opt. Lett., OL*, vol. 43, no. 8, pp. 1846–1849, Apr. 2018, doi: 10.1364/OL.43.001846.

[32] X. Leng *et al.*, “Feasibility of co-registered ultrasound and acoustic-resolution photoacoustic imaging of human colorectal cancer,” *Biomed. Opt. Express, BOE*, vol. 9, no. 11, pp. 5159–5172, Nov. 2018, doi: 10.1364/BOE.9.005159.

[33] Z. Guo, Y. Li, and S.-L. Chen, “Miniature probe for in vivo optical- and acoustic-resolution photoacoustic microscopy,” *Opt. Lett., OL*, vol. 43, no. 5, pp. 1119–1122, Mar. 2018, doi: 10.1364/OL.43.001119.

[34] Y. Qu *et al.*, "Transvaginal fast-scanning optical-resolution photoacoustic endoscopy," *JBO*, vol. 23, no. 12, p. 121617, Dec. 2018, doi: 10.1117/1.JBO.23.12.121617.

[35] P. Wang, Z. Chen, F. Yang, S. Yang, and D. Xing, "Intravascular tri-modality system: Combined ultrasound, photoacoustic, and elasticity imaging," *Appl. Phys. Lett.*, vol. 113, no. 25, p. 253701, Dec. 2018, doi: 10.1063/1.5051387.

[36] P. Lei, X. Wen, L. Wang, P. Zhang, and S. Yang, "Ultrafine intravascular photoacoustic endoscope with a 0.7 mm diameter probe," *Opt. Lett., OL*, vol. 44, no. 22, pp. 5406–5409, Nov. 2019, doi: 10.1364/OL.44.005406.

[37] K. Zhan, L. Wang, Z. Chen, and D. Xing, "Intravascular Photoacoustic and Autofluorescence Imaging for Detecting Intraplaque Hemorrhage: A Feasibility Study," *IEEE Journal of Selected Topics in Quantum Electronics*, vol. 27, no. 4, pp. 1–5, Jul. 2021, doi: 10.1109/JSTQE.2020.3020237.

[38] C. Lu, K. Xiong, Y. Ma, W. Zhang, Z. Cheng, and S. Yang, "Electrothermal-MEMS-induced nonlinear distortion correction in photoacoustic laparoscopy," *Opt. Express, OE*, vol. 28, no. 10, pp. 15300–15313, May 2020, doi: 10.1364/OE.392493.

[39] M. Basij, A. Karpiouk, I. Winer, S. Emelianov, and M. Mehrmohammadi, "Dual-Illumination Ultrasound/ Photoacoustic System for Cervical Cancer imaging," *IEEE Photonics J*, vol. 13, no. 1, p. 6900310, Feb. 2021, doi: 10.1109/jphot.2020.3043685.

[40] Y. Zhu *et al.*, "Prototype endoscopic photoacoustic-ultrasound balloon catheter for characterizing intestinal obstruction," *Biomed. Opt. Express, BOE*, vol. 13, no. 6, pp. 3355–3365, Jun. 2022, doi: 10.1364/BOE.456672.

[41] R. Ansari, E. Z. Zhang, A. E. Desjardins, and P. C. Beard, "All-optical forward-viewing photoacoustic probe for high-resolution 3D endoscopy," *Light Sci Appl*, vol. 7, no. 1, Art. no. 1, Oct. 2018, doi: 10.1038/s41377-018-0070-5.

[42] S. J. Mathews *et al.*, "All-optical dual photoacoustic and optical coherence tomography intravascular probe," *Photoacoustics*, vol. 11, pp. 65–70, Sep. 2018, doi: 10.1016/j.pacs.2018.07.002.

[43] G. Li, Z. Guo, and S.-L. Chen, "Miniature Probe for Forward-View Wide-Field Optical-Resolution Photoacoustic Endoscopy," *IEEE Sensors Journal*, vol. 19, no. 3, pp. 909–916, Feb. 2019, doi: 10.1109/JSEN.2018.2878801.

[44] R. Ansari, E. Z. Zhang, A. E. Desjardins, and P. C. Beard, "Miniature all-optical flexible forward-viewing photoacoustic endoscopy probe for surgical guidance," *Opt. Lett., OL*, vol. 45, no. 22, pp. 6238–6241, Nov. 2020, doi: 10.1364/OL.400295.

[45] S. Mezil *et al.*, "Single-shot hybrid photoacoustic-fluorescent microendoscopy through a multimode fiber with wavefront shaping," *Biomed. Opt. Express, BOE*, vol. 11, no. 10, pp. 5717–5727, Oct. 2020, doi: 10.1364/BOE.400686.

[46] T. Zhao *et al.*, "Ultrathin, high-speed, all-optical photoacoustic endomicroscopy probe for guiding minimally invasive surgery," *Biomed. Opt. Express, BOE*, vol. 13, no. 8, pp. 4414–4428, Aug. 2022, doi: 10.1364/BOE.463057.

[47] B. Dong, S. Chen, Z. Zhang, C. Sun, and H. F. Zhang, "Photoacoustic probe using a microring resonator ultrasonic sensor for endoscopic applications," *Opt. Lett., OL*, vol. 39, no. 15, pp. 4372–4375, Aug. 2014, doi: 10.1364/OL.39.004372.

[48] J. Zhou *et al.*, "Miniature non-contact photoacoustic probe based on fiber-optic photoacoustic remote sensing microscopy," *Opt. Lett., OL*, vol. 46, no. 22, pp. 5767–5770, Nov. 2021, doi: 10.1364/OL.444889.

[49] Y. Liang *et al.*, "Optical-resolution functional gastrointestinal photoacoustic endoscopy based on optical heterodyne detection of ultrasound," *Nat Commun*, vol. 13, no. 1, Art. no. 1, Dec. 2022, doi: 10.1038/s41467-022-35259-5.

[50] B. Fu *et al.*, "Optical ultrasound sensors for photoacoustic imaging: a narrative review," *Quant Imaging Med Surg*, vol. 12, no. 2, pp. 1608–1631, Feb. 2022, doi: 10.21037/qims-21-605.

[51] S. Hu, "Emerging concepts in functional and molecular photoacoustic imaging," *Current Opinion in Chemical Biology*, vol. 33, pp. 25–31, Aug. 2016, doi: 10.1016/j.cbpa.2016.04.003.

[52] R. R. Anderson *et al.*, "Selective photothermolysis of lipid-rich tissues: A free electron laser study," *Lasers in Surgery and Medicine*, vol. 38, no. 10, pp. 913–919, 2006, doi: 10.1002/lsm.20393.

[53] P. C. Beard, F. Perennes, and T. N. Mills, "Transduction mechanisms of the Fabry-Perot polymer film sensing concept for wideband ultrasound detection," *IEEE Transactions on Ultrasonics, Ferroelectrics, and Frequency Control*, vol. 46, no. 6, pp. 1575–1582, Nov. 1999, doi: 10.1109/58.808883.

[54] E. Zhang, J. Laufer, and P. Beard, "Backward-mode multiwavelength photoacoustic scanner using a planar Fabry-Perot polymer film ultrasound sensor for high-resolution three-dimensional imaging of biological tissues," *Appl. Opt., AO*, vol. 47, no. 4, pp. 561–577, Feb. 2008, doi: 10.1364/AO.47.000561.

[55] A. P. Jathoul *et al.*, "Deep in vivo photoacoustic imaging of mammalian tissues using a tyrosinase-based genetic reporter," *Nature Photon*, vol. 9, no. 4, Art. no. 4, Apr. 2015, doi: 10.1038/nphoton.2015.22.

[56] N. Huynh, O. Ogunlade, E. Zhang, B. Cox, and P. Beard, "Photoacoustic imaging using an 8-beam Fabry-Perot scanner," in *Photons Plus Ultrasound: Imaging and Sensing 2016*, Mar. 2016, vol. 9708, pp. 505–509. doi: 10.1117/12.2214334.

[57] N. Huynh *et al.*, "Single-pixel camera photoacoustic tomography," *JBO*, vol. 24, no. 12, p. 121907, Sep. 2019, doi: 10.1117/1.JBO.24.12.121907.

[58] T. Allen, E. Zhang, and P. Beard, "Time-gated Parallelised Interrogation of a Fabry-Perot Ultrasound Sensor Using a Camera for Fast Photoacoustic Tomography," in *Biophotonics Congress: Biomedical Optics 2022 (Translational, Microscopy, OCT, OTS, BRAIN) (2022), paper OM2D.6*, Apr. 2022, p. OM2D.6. doi: 10.1364/OTS.2022.OM2D.6.

[59] P. Morris, A. Hurrell, A. Shaw, E. Zhang, and P. Beard, "A Fabry–Pérot fiber-optic ultrasonic hydrophone for the simultaneous measurement of temperature and acoustic pressure," *The Journal of the Acoustical Society of America*, vol. 125, no. 6, pp. 3611–3622, Jun. 2009, doi: 10.1121/1.3117437.

[60] E. Z. Zhang and P. C. Beard, "Characteristics of optimized fibre-optic ultrasound receivers for minimally invasive photoacoustic detection," in *Photons Plus Ultrasound: Imaging and Sensing 2015*, Mar. 2015, vol. 9323, pp. 151–159. doi: 10.1117/12.2081904.

[61] J. A. Guggenheim *et al.*, "Ultrasensitive plano-concave optical microresonators for ultrasound sensing," *Nature Photon*, vol. 11, no. 11, Art. no. 11, Nov. 2017, doi: 10.1038/s41566-017-0027-x.

[62] P. C. Beard, "Interrogation of free-space Fabry–Perot sensing interferometers by angle tuning," *Meas. Sci. Technol.*, vol. 14, no. 11, p. 1998, Sep. 2003, doi: 10.1088/0957-0233/14/11/019.

[63] P. C. Beard and T. N. Mills, "Optical detection system for biomedical photoacoustic imaging," in *Biomedical Optoacoustics*, May 2000, vol. 3916, pp. 100–109. doi: 10.1117/12.386310.

[64] P. C. Beard, "Two-dimensional ultrasound receive array using an angle-tuned Fabry-Perot polymer film sensor for transducer field characterization and transmission ultrasound imaging," *IEEE Transactions on Ultrasonics, Ferroelectrics, and Frequency Control*, vol. 52, no. 6, pp. 1002–1012, Jun. 2005, doi: 10.1109/TUFFC.2005.1504022.

[65] P. C. Beard and T. N. Mills, "Optical fiber sensor for the detection of laser-generated ultrasound in arterial tissues," in *Medical Sensors II and Fiber Optic Sensors*, Feb. 1995, vol. 2331, pp. 112–122. doi: 10.1117/12.201235.

[66] Y. Hou, J. Kim, S. Huang, S. Ashkenazi, L. J. Guo, and M. O'Donnell, "Characterization of a broadband all-optical ultrasound transducer-from optical and acoustical properties to imaging," *IEEE Transactions on Ultrasonics, Ferroelectrics, and Frequency Control*, vol. 55, no. 8, pp. 1867–1877, Aug. 2008, doi: 10.1109/TUFFC.2008.870.

[67] S. Ashkenazi, Y. Hou, T. Buma, and M. O'Donnell, "Optoacoustic imaging using thin polymer étalon," *Appl. Phys. Lett.*, vol. 86, no. 13, p. 134102, Mar. 2005, doi: 10.1063/1.1896085.

[68] C. Sheaff and S. Ashkenazi, "A Polyimide-Etalon Thin Film Structure for All-Optical High-Frequency Ultrasound Transduction," *IEEE Transactions on Ultrasonics, Ferroelectrics, and Frequency Control*, vol. 59, no. 10, pp. 2254–2261, Oct. 2012, doi: 10.1109/TUFFC.2012.2450.

[69] C. Sheaff and S. Ashkenazi, "Characterization of an improved polyimide-etalon all-optical transducer for high-resolution ultrasound imaging," *IEEE Transactions on Ultrasonics, Ferroelectrics, and Frequency Control*, vol. 61, no. 7, pp. 1223–1232, Jul. 2014, doi: 10.1109/TUFFC.2014.3021.

[70] Specialty Coating Systems, "SCS Parylene Properties," *Technical Library*. https://scscoatings.com/technical-library/ (accessed Mar. 19, 2023).

[71] M. F. A. Rahman, M. R. Arshad, A. A. Manaf, and M. I. H. Yaacob, "An investigation on the behaviour of PDMS as a membrane material for underwater acoustic sensing," *IJMS Vol.41(6) [December 2012]*, Dec. 2012, Accessed: Mar. 19, 2023. [Online]. Available: http://nopr.niscpr.res.in/handle/123456789/15151

[72] C. Sheaff, "All-optical ultrasound transducers for high resolution imaging," University of Minnesota, 2014. Accessed: Mar. 19, 2023. [Online]. Available: http://conservancy.umn.edu/handle/11299/171722

[73] K. Izdihar, H. R. Abdul Razak, N. Supion, M. K. A. Karim, N. H. Osman, and M. Norkhairunnisa, "Structural, Mechanical, and Dielectric Properties of Polydimethylsiloxane and Silicone Elastomer for the Fabrication of Clinical-Grade Kidney Phantom," *Applied Sciences*, vol. 11, no. 3, Art. no. 3, Jan. 2021, doi: 10.3390/app11031172.

[74] Kayaku Advanced Materials, "SU-8 2000 Permanent Negative Epoxy Photoresist," *SU-8 2000*, Aug. 2020. https://kayakuam.com/wp-content/uploads/2020/08/KAM-SU-8-2000-2000.5-2015-Datasheet-8.13.20-final.pdf (accessed Mar. 19, 2023).

[75] HD Microsystems, "PRODUCT BULLETIN PI 2525, PI 2555 & PI 2574," *PRODUCT BULLETINS*, Nov. 2012. https://www.hdmicrosystems.com/content/dam/dupont/amer/us/en/hd-microsystems/public/documents/PI-2525_2555_2574_ProductBulletin.pdf (accessed Mar. 19, 2023).

[76] O. S. Heavens and S. F. Singer, "Optical Properties of Thin Solid Films," *Physics Today*, vol. 9, p. 24, Jan. 1956, doi: 10.1063/1.3059910.

[77] J. Krautkrämer, “Über optische Konstanten, elektrischen Widerstand und Struktur dünner Metallschichten,” *Annalen der Physik*, vol. 424, no. 6, pp. 537–576, 1938, doi: 10.1002/andp.19384240606.

[78] K. M. McPeak *et al.*, “Plasmonic Films Can Easily Be Better: Rules and Recipes,” *ACS Photonics*, vol. 2, no. 3, pp. 326–333, Mar. 2015, doi: 10.1021/ph5004237.

[79] T. Hinoi *et al.*, “Mouse Model of Colonic Adenoma-Carcinoma Progression Based on Somatic Apc Inactivation,” *Cancer Research*, vol. 67, no. 20, pp. 9721–9730, Oct. 2007, doi: 10.1158/0008-5472.CAN-07-2735.

[80] International Electrotechnical Commission, *Safety of laser products - Part 1: Equipment classification, requirements and user’s guide*. Geneva: International Electrotechnical Commission, 2007. Accessed: Mar. 13, 2023. [Online]. Available: http://www.saiglobal.com/online/autologin.asp

[81] T. F. Chan and L. A. Vese, “Active contours without edges,” *IEEE Transactions on Image Processing*, vol. 10, no. 2, pp. 266–277, Feb. 2001, doi: 10.1109/83.902291.

[82] E. Baumann *et al.*, “A backward-mode optical-resolution photoacoustic microscope for 3D imaging using a planar Fabry-Pérot sensor,” *Photoacoustics*, vol. 24, p. 100293, Dec. 2021, doi: 10.1016/j.pacs.2021.100293.

[83] J. Buchmann *et al.*, “Characterization and modeling of Fabry–Perot ultrasound sensors with hard dielectric mirrors for photoacoustic imaging,” *Applied Optics*, vol. 56, p. 5039, Jun. 2017, doi: 10.1364/AO.56.005039.